UNIVERSITY OF CALIFORNIA SAN DIEGO

DIGITAL LIGHT PROCESSING (DLP)-BASED 3D PRINTING FOR MICROPHYSIOLOGICAL SYSTEMS APPLICATIONS

A dissertation submitted in partial satisfaction of the

requirements for the degree Doctor of Philosophy

in

Nanoengineering

by

Hanjun Henry Hwang

Committee in charge:

Professor Shaochen Chen, Chair
Professor Liangfang Zhang, Co-chair
Professor Shengqiang Cai
Professor Yu-hwa Lo
Professor Donald Sirbuly

2022

The Dissertation of Hanjun Henry Hwang is approved, and it is acceptable in quality and form for publication on microfilm and electronically.

University of California San Diego

2022

DEDICATION

I dedicate this dissertation to my family, both blood and chosen:

My mother Chanwon Park and my father Leeseok Hwang, for their loving support.

My brother, Andrew Hankyel Hwang, for his unwavering confidence.

My partner Paula Khim, for her infinite patience and for being my better half.

My friends & colleagues for the good times, great conversations, and happy memories.

I will cherish you all.

EPIGRAPH

It is the struggle itself that is the most important.

We must strive to be more than we are.

It does not matter that we will never reach our ultimate goal, for the effort yields its own rewards.

- Lieutenant Commander Data, *Star Trek: The Next Generation*

TABLE OF CONTENTS

LIST OF ABBREVIATIONS

2D	Two dimensional
2PP	Two-photon polymerization
3D	Three dimensional
3DP	Three dimensional (3D) printing
CLIP	Continuous liquid interface production
DLP	Digital light processing
DMD	Digital micromirror device
EDTA	Ethylenediamine tetra-acetic acid
EGM	Endothelial Growth Media
FITC-Dextran	Fluorescein isothiocyanate-Dextran
GelMA	Gelatin methacryloyl
HA	Hyaluronic acid
HA-GM	Hyaluronic acid gelatin methacrylate
hTSC	Human trophoblast stem cell
HUVEC	Human umbilical vein endothelial cell
LAP	Lithium phenyl-2,4,6-trimethylbenzoylphosphinate
mm	Millimeter
Na-F	Sodium fluorescein
nm	Nanometer
PDMS	Polydimethylsiloxane
PDSF	Placenta-derived stromal fibroblast
PEGDA	Poly(ethylene glycol) diacrylate
STB	Syncytiotrophoblast
TEMPO	2,2,6,6-tetramethylpiperidine 1-oxyl
UV	Ultraviolet
VHM	Variable height micromixer
μCOP	Micro continuous optical printing
μm	Micrometer

LIST OF FIGURES

LIST OF MOVIES

LIST OF TABLES

ACKNOWLEDGEMENTS

I would like to both thank and acknowledge Dr. Shaochen Chen as my advisor and mentor throughout my doctoral program, as he gave me the space and support necessary for me to further develop my engineering skills and scientific creativity. I am grateful for his patience and wisdom during my darkest and difficult moments. I am especially honored for having been able to both learn and contribute to this group.

To my dissertation committee members, Dr. Liangfang Zhang, Dr. Shengqiang Cai, Dr. Yu-hwa Lo, and Dr. Donald Sirbuly, I give many thanks to you all for your time and advice.

I would like to thank all my undergraduate mentees, fellow graduate student colleagues, postdoctoral fellows, and collaborators of all stripes, both past and present, for their valuable time, expertise, shared experiences, and friendship. I give special thanks to my collaborators in the Louise Laurent group, particularly Dr. Chandana Tekkatte and Dr. Scott Lindsay-Hewett. I give special thanks to my undergraduate mentee Leilani Kwe, for her diligence, friendship, and moral support.

To my friends and family (both biological and chosen), I thank you for your love and support. I literally would not have made it through this program without you all.

Chapter 1, in full, includes a reprint of the published article, "3D-Printing of Functional Biomedical Microdevices via Light- and Extrusion-Based Approaches." Hwang, Henry H.; Zhu, Wei; Victorine, Grace; Lawrence; Natalie; Chen, Shaochen. Small Methods Henry H. Hwang, Wei Zhu, Grace Victorine, Natalie Lawrence, and Shaochen Chen. Small Methods, 2018. The dissertation author was the primary investigator and author of this work.

Chapter 2, in full, includes a reprint of the published article, “Direct 3D-Printing of Cell-Laden Constructs in Microfluidic Architectures.” Liu, Justin; Hwang, Henry H.; Wang, Pengrui; Whang, Grace; Chen, Shaochen. Lab on a Chip, 2016. The dissertation author was a co-primary investigator and co-author of this work.

Chapter 3, in full, includes a reprint of the published article, “High Throughput Direct 3D Bioprinting in Multiwell Plates.” Hwang, Henry H.*; You, Shangting*; Ma, Xuanyi; Kwe, Leilani; Victorine, Grace; Lawrence, Natalie; Wan, Xueyi; Shen, Haixu; Zhu, Wei; Chen, Shaochen. Biofabrication, 2021. The dissertation author was a co-primary investigator and co-first author of this work.

Chapter 4, in full, includes material currently being prepared for submission for publication under the working title, “Human Placenta-on-a-Chip: a biomimetic microfluidic 3D transport model.” Hwang, Henry H.; Tekkatte, Chandana; Lindsay-Hewett, Scott; Yu, Claire; Ma, Xuanyi; Farah, Omar; Parast, Mana M.; Laurent, Louise C.; Chen, Shaochen. *In preparation.* The dissertation author is a co-primary investigator and co-author of this ongoing work.

VITA

2011 Bachelor of Science in Engineering: Biomedical Engineering
Duke University, North Carolina, USA

2012 Master of Science in Engineering: Biomedical Engineering
Cornell University, New York, USA

2022 Doctor of Philosophy: Nanoengineering
University of California San Diego, California, USA

TEACHING EXPERIENCE

Cornell University
Introduction to Biomedical Engineering

University of California San Diego
Nanomanufacturing
Multi-scale Transport

PUBLICATIONS

1. Liu, J., **Hwang, H. H.,** Wang, P., Whang, G. & Chen, S. Direct 3D-printing of cell-laden constructs in microfluidic architectures. *Lab Chip* **16**, 1430–1438 (2016).

2. **Hwang, H. H.,** Zhu, W., Victorine, G., Lawrence, N. & Chen, S. 3d Printing: 3D-Printing of Functional Biomedical Microdevices via Light- and Extrusion-Based Approaches (Small Methods 2/2018). *Small Methods* **2**, 1870021 (2018).

3. **Hwang, H. H**., You, S., Ma, X., Kwe, L., Victorine, G., Lawrence, N., Wan, X., Shen, H., Zhu, W. & Chen, S. High throughput direct 3D bioprinting in multiwell plates. *Biofabrication* **13**, 025007 (2021).

4. **Hwang, H. H.**, Tekkatte, C., Lindsay-Hewett, S., Yu, C., Ma, X., Farah, O., Parast, M. M., Laurent, L. C., & Chen, S. "Human Placenta-on-a-Chip: a biomimetic microfluidic 3D transport model." *In Preparation.* (2022).

5. Yuan, H., Khoury, C. G., Hwang, H. H., Wilson, C. M., Grant, G. A. & Vo-Dinh, T. Gold nanostars: Surfactant-free synthesis, 3D modelling, and two-photon photoluminescence imaging. *Nanotechnology* **23**, 075102 (2012).

6. Karabacak, N. M., Spuhler, P. S., Fachin, F., Lim, E. J., Pai, V., Ozkumur, E., Martel, J. M., Kojic, N., Smith, K., Chen, P., Yang, J., Hwang, H., Morgan, B., Trautwein, J., Barber, T. A., Stott, S. L., Maheswaran, S., Kapur, R., Haber, D. A. & Toner, M.

Microfluidic, marker-free isolation of circulating tumor cells from blood samples. *Nat Protoc* **9**, 694–710 (2014).

7. Fachin, F., Spuhler, P., Martel-Foley, J. M., Edd, J. F., Barber, T. A., Walsh, J., Karabacak, M., Pai, V., Yu, M., Smith, K., Hwang, H., Yang, J., Shah, S., Yarmush, R., Sequist, L. V., Stott, S. L., Maheswaran, S., Haber, D. A., Kapur, R. & Toner, M. Monolithic Chip for High-throughput Blood Cell Depletion to Sort Rare Circulating Tumor Cells. *Sci Rep* **7**, 10936 (2017).

8. Warner, J., Gillies, A., Hwang, H. H., Zhang, H., Lieber, R., & Chen, S., "3D-printed biomaterials with regional auxetic properties", *Journal of the Mechanical Behavior of Biomedical Materials*, Vol. 76, pp. 145-152, (2017).

9. Warner, J. J., Wang, P., Mellor, W. M., Hwang, H. H., Park, J. H., Pyo, S.-H. & Chen, S. 3D printable non-isocyanate polyurethanes with tunable material properties. *Polym. Chem*. **10**, 4665–4674 (2019).

10. You, S., Wang, P., Schimelman, J., Hwang, H. H. & Chen, S. High-fidelity 3D printing using flashing photopolymerization. *Additive Manufacturing* **30**, 100834 (2019).

11. You, S., Guan, J., Alido, J., Hwang, H. H., Yu, R., Kwe, L., Su, H. & Chen, S. Mitigating Scattering Effects in Light-Based Three-Dimensional Printing Using Machine Learning. *Journal of Manufacturing Science and Engineering* **142**, (2020).

12. You, S., Guan,. J., Alido, J., Hwang, H. H., Yu, R., Kwe, L., Su, H., & Chen, S., "Mitigating Scattering Effects in Light-based 3D Printing Using Machine Learning", *Journal of Manufacturing Science and Engineering*, (2020).

13. Zhong, Z., Balayan, A., Tian, J., Xiang, Y., Hwang, H. H., Wu, X., Deng, X., Schimelman, J., Sun, Y., Ma, C., Santos, A. D., You, S., Tang, M., Yao, E., Shi, X., Steinmetz, N. F., Deng, S. X. & Chen, S. Bioprinting of dual ECM scaffolds encapsulating limbal stem/progenitor cells in active and quiescent statuses. *Biofabrication* **13**, 044101 (2021).

14. Wangpraseurt, D., Sun, Y., You, S., Chua, S.-T., Noel, S., Willard, H. F., Berry, D. B., Plummer, S., Xiang, Y., Hwang, H. H., Kaandorp, J., Diaz, J. M., La Jeunesse, T. C., Pernice, M., Vignolini, S., Tresguerres, M., & Chen, S., Bioprinted living coral microenvironments mimicking coral-algal symbiosis", *Advanced Functional Materials*, (2022).

15. You, S., Xiang, Y., Hwang, H. H., Berry, D. B>, Kiratitanaporn, W., Guan, J., Yao, E., Tang, M., Zhong, Z., Ma, X., Wangpraseurt, D., & Chen, S. "High Cell Density and High Resolution 3D bioprinting for Fabricating Vascularized Tissues." *In submission.* 2022.

ABSTRACT OF DISSERTATION

DIGITAL LIGHT PROCESSING (DLP)-BASED 3D PRINTING FOR MICROPHYSIOLOGICAL SYSTEMS APPLICATIONS

by

Hanjun Henry Hwang
Doctor of Philosophy in Nanoengineering
University of California San Diego, 2022
Professor Shaochen Chen, Chair
Professor Liangfang Zhang, Co-chair

Tissue engineering encompasses a wide variety of goals, including but not limited to the repair, improvement, or replacement of whole tissues or organs, as well as *in vitro* investigations of native physiology and functionality. The incorporation of three-dimensional (3D) printing as a biomanufacturing technique in recent years has greatly contributed to the field of tissue engineering, granting enhanced capability in fabricating bioartificial constructs that can be used across a myriad of applications, including inducing endogenous regeneration, recapitulating existing pathophysiology, or investigating drug-tissue interactions. Among the varieties of 3D printing paradigms, light-based 3D bioprinting techniques, such as Digital Light Processing (DLP)-based modalities, have significantly advanced fabrication speed, resolution, and

biomanufacturing capability by enabling fabrication options that would be challenging to implement using more traditional extrusion-based techniques. In this work, we investigate the use of DLP-based 3D printing as both a supportive and direct manufacturing platform in the context of tissue engineering and microphysiological systems.

First, a review of extrusion and light-based 3D printing approaches in the manufacturing of functional biomedical microdevices is addressed. The differences between various 3D printing paradigms, their advantages and disadvantages, and several showcases of their capabilities are discussed. Next, the utilization of DLP 3D printing as a dual-purpose microfluidic and *in situ* tissue scaffold fabrication technique for the purpose of dynamic cell culture microenvironment control is discussed. A passive micromixer was developed and evaluated for its mixing efficiency, and DLP 3D printing was used to fabricate tissue scaffolds inside the enclosed microfluidic device. Next, *in situ* DLP 3D printing into well-plates in the context of high throughput pharmaceutical compound screening is investigated. 3D bioprinted liver-based tissue scaffolds were fabricated at high throughput rates. The speed and dimensional accuracy of printing, cell viability, functional chemotherapeutic assays, and multi-cellular 3D bioprinting were investigated. Finally, a combination of DLP 3D printing and microfluidics is utilized in the development of a novel Placenta-on-a-Chip microphysiological system. A 'hybrid' open/closed 3D microfluidic device was fabricated, utilizing multiple primary human cell sources to generate a tri-coculture *in vitro* model. Tri-coculture viability, barrier integrity, and transfer rates of solutes-of-interest were investigated. In summary, these explorations of Digital Light Processing (DLP)-based 3D printing as a biomanufacturing platform for the creation of microphysiological systems provide significant scientific and translational advancement in the fields of 3D cell culture, microphysiological systems, and pharmaceutical drug discovery.

CHAPTER 1: INTRODUCTION – 3D PRINTING OF FUNCTIONAL BIOMEDICAL MICRODEVICES VIA LIGHT- AND EXTRUSION-BASED APPROACHES

1.1. Abstract

3D-printing is a powerful additive manufacturing tool, one that enables fabrication of biomedical devices and systems that would otherwise be challenging to create with more traditional methods such as machining or molding. Many different classes of 3D-printing technologies exist, most notably the extrusion-based and light-based 3D-printers that are popular in consumer markets, with advantages and limitations for each modality. The focus here is primarily on showcasing these 3D-printing platforms" ability to create different types of functional biomedical microdevices – their advantages and limitations are covered with respect to other classes of 3D-printing, as well as the past, recent, and future efforts to advance the functional micro-device domain. In particular, the fabrication of micro-machines/robotics, drug delivery devices, biosensors, and microfluidics is addressed. The current challenges associated with 3D-printing functional microdevices are also addressed, as well as future directions to improve both the printing techniques and the performance of the printed products.

1.2. Introduction

3D-printing technologies have made significant strides in both technological sophistication and ubiquity, with users across consumer, academic, industrial, and medical domains incorporating 3D-printing into their workflows. By "3D-printing," we refer to a wide variety of additive manufacturing processes that successively "add" material in a controlled manner, thus generally enabling the fabrication of user-defined 3D objects. This is in contrast with subtractive manufacturing and machining techniques, where the final construct is created by successively "removing" material from a solid bulk substance. 3D-printing has gained popularity due to its

rapid prototyping flexibility, as well as the ability to produce features that would otherwise be challenging to produce with strictly subtractive manufacturing, i.e. non-standard geometries, multi-material layers, and isolated hollow spaces. In the context of creating functional microdevices, where multiple length scales and grades of complexity may be required in a quickly evolving field of biomedical needs, such 3D-printing capabilities can be invaluable.

By "functional microdevices," we refer to systems and technologies that, by way of fabrication and/or function, generally perform tasks on the microscale. These devices can vary greatly in both form and function, but in the biomedical domain they tend to serve diagnostic and/or therapeutic purposes. Examples span the range from microscale robotics and biosensors to tissue-engineered models and microfluidic lab-on-a-chip systems, with some devices capable of fulfilling more than one role. As 3D-printing technology improves, so too does the ability to fabricate functional microdevices of higher sophistication and functionality, which is of significant importance to the biomedical research, industry, and healthcare fields, as there are growing demands on improving not just the speed and cost of fabrication, but also scalability and utility.

Here, we acknowledge that there have already been extensive efforts to characterize the technical performance of most popular 3D-printing modalities, such as fused deposition modeling (FDM)-based, multi jet modeling (MJM)-based, and laser stereolithography (SLA). In lieu of comparing the detailed minutiae of different technical performance parameters of different 3D-printing methods, we instead direct particular focus on showcasing different types of functional biomedical microdevices that have been created via 3D-printing, primarily light and extrusion-based modalities. Building from previous reviews in the field of 3D-printing for biomedical applications[1–4], we briefly discuss the basic principles of various 3D-printing

paradigms, the relative advantages and limitations, and salient examples of recent and prominent functional biomedical microdevices created by 3D-printing.

1.3. Current 3D-printing Technologies

On a fundamental level, 3D-printing involves successive addition of material to itself in a precise, controlled manner, ultimately resulting in a 3D object. However, in recent years, 3D-printing techniques have innovated and matured along different paths, resulting in a plethora of technologies that are capable of creating functional microdevices. Here, we describe the basic operating principles of several different 3D-printing modalities that we have loosely categorized into two overarching types: extrusion-based 3D-printing (E-3DP), where there is controlled release/deposition of a material via a forming tool, and light-based 3D-printing (L-3DP), where directed light is used to selectively-shape material into desired 3D constructs. While we acknowledge that not all 3D-printing modalities will fit neatly into these two classifications, they serve as a useful mental model in assessing relative advantages and limitations. A pictorial overview of the 3D-printing techniques most relevant here is given in **Figure 1**.

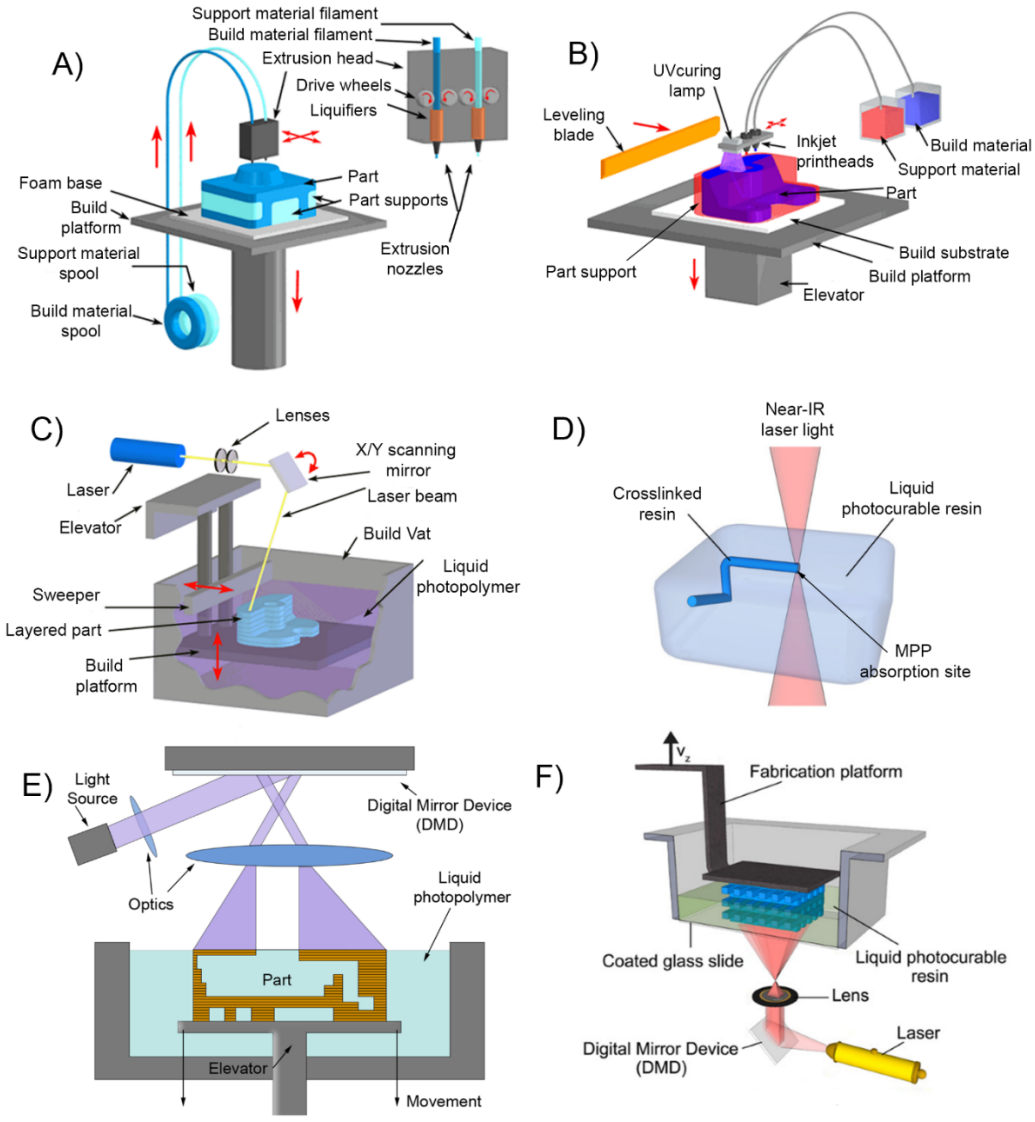

Figure 1.1: Schematic overview of various E-3DP and L-3DP modalities.

A) E-3DP: Schematic of a fused deposition modeling (FDM) 3D-printer, where thermoplastic filaments spool through a heated nozzle extruder. A–C) Adapted with permission[5]. Copyright 2016, The Royal Society of Chemistry. B) E-3DP: Schematic of a multi-jet modeling 3D-printer, where materials are jetted via printheads. The variant pictured photopolymerizes the dispensed droplets in place. C) L-3DP: Schematic of traditional stereolithography 3D-printer, where a laser light is raster-scanned across the surface of a photopolymerizable resin as a build stage within moves. D) L-3DP: Multi-photon polymerization 3D-printing, where nonlinear photon absorption from a laser into a photopolymerizable resin creates structures as the laser is traced in 3D space[6]. E) L-3DP: The "free surface" configuration digital light processing 3D-printing, where a 2D cross-section of light strikes the air-liquid surface of photopolymerizable resin as a build stage sinks into the vat. F) L-3DP: The "bat" configuration of digital light processing 3D-printing, where a 2D cross-section of light strikes the bottom of a transparent vat of photopolymerizable resin, as a build stage pulls out of the vat[6]. D, F) Adapted with permission[6]. Copyright 2012, Elsevier.

1.3.1. Extrusion-Based 3D-Printing

Extrusion-based 3D-printing (E-3DP) covers a number of different types of 3D-printers – of them, perhaps the most common examples used in fabricating functional biomedical microdevices are fused deposition modeling (FDM), nozzle-based 3D-printing, and multi-jet modeling (MJM). While there are differences in the compositions of materials used and the exact manner in which they are deposited, all fundamentally depend on the controlled release of the building material via a forming tool.

1.3.2. Fused Deposition Modeling (FDM)

FDM-based 3D-printers have gained much popularity in the last decade, in part due to the expiry of the original patent on FDM technology in 2009, but also due to their relatively simple construction and inexpensive material costs. These types of printers additively build 3D structures by extruding thermoplastic materials via a heated, motorized nozzle that can be digitally-controlled such that it translates freely in 3D-space. As the material extrudes from the nozzle, it partially cools on contact with air, thus depositing and fusing material in a line-by-line, layer-by-layer fashion until the final 3D object is formed. FDM 3D-printers are most commonly known to use thermoplastic materials primarily due to low melting temperatures, and in the context of fabricating functional biomedical devices there are many suitable plastics and polymers that are not only inexpensive, but can have desirable material properties such as biocompatibility and mechanical durability. Examples of common materials used in FDM include acrylonitrile butadiene styrene (ABS), polypropylene (PP), polycarbonate (PC)[7]; biocompatible polymers include examples such as polycaprolactone (PCL), polylactic acid (PLA), and polyglycolic acid (PGA)[8], most of which are sold in cheap, easy-to-use form factors such as pellets, wires, and laminates.

1.3.3. Nozzle-Based 3D-Printing

Nozzle-based 3D-printing is a more generalized version of FDM in that the material choices are not limited to strictly thermoplastic materials. Rather, this modality allows the use of any liquid and/or flowable precursors that can be driven through a nozzle; these precursors can be immobilized and/or removed as necessary to build the final structure (again in a drop-by-drop, line-by-line, layer-by-layer fashion). Thus, in comparison to FDM, users are afforded more material choices in fabricating functional microdevices, and examples can range from colloidal nanoparticles and cell-laden solutions to hydrogels and viscoelastic materials. This approach is particularly suited for bioprinting applications, where soft, biocompatible materials that would otherwise be incompatible with FDM techniques are used in fabricating structures meant for biological interaction.

1.3.4. Multi-Jet Modeling

Multi-jet modeling (MJM), otherwise known more generically as inkjet 3D-printing, operates in a manner similar to the inkjet printers commonly seen in consumer and business environments – liquid droplets are dispensed in a layer-by-layer fashion via numerous nozzles contained in movable printheads. The difference with MJM as compared to commercial inkjet printers is that these droplets are commonly composed of a liquid prepolymer, which are then crosslinked quickly after deposition (either through thermal cooling or photopolymerization) such that each layer is bonded to the previously deposited layer, thus building the final 3D object. The multiple-nozzle approach to the printhead means that a MJM printer can deploy multiple materials simultaneously in a single pass. Some MJM printers can also deliver gel- or wax-like sacrificial materials, which after post-processing removal, allows for the construction of 3D-

objects with void spaces, in addition to multiple materials (and thus multiple material properties) in any given layer.

1.3.5. Light-Based 3D-printing

L-3DP fundamentally uses light as the primary effector for fabrication – historically, this category was filled mostly by stereolithography (SLA), where ultraviolet laser light was raster-scanned across the surface of photopolymerizable resins. In the last two decades, ever since Chuck Hull first coined the term "stereolithography" in 1986[9] however, L-3DP has come to encompass a wide variety of materials, light sources, and motion control. Material choices can include the gas, liquid, and solid phases of matter; light sources can range from the deep ultraviolet (UV) all the way to the upper end of the visible spectra; and the light itself can be controlled to strike not just surfaces but also within the depths of a photopolymerizable material[10]. In this context of fabricating functional biomedical microdevices, most L-3DP technologies still rely on the photopolymerization of liquid prepolymer into solid, cured entities.

By "photopolymerization," we refer to the set of light-induced polymerization reactions in which the energetic absorption of light by a photosensitive material causes chain-growth crosslinking and polymerization of functional monomers into polymers[11]. Whether the material is directly photopolymerized or mediated by photo-crosslinking agents can depend on user needs, but most L-3DP systems commonly utilize free-radical polymerization (FRP). The FRP process is briefly described as follows: i) light strikes a photoinitiator molecule that then generates free radical species; ii) these free radical species interact with functional monomers; iii) these active monomers then react with other monomers in a propagative manner to produce polymeric chains until reaction termination. After the photopolymerization and motion-related steps in the 3D-printing process are completed, any unreacted materials can be developed or flushed away to

yield the final 3D object. Since photopolymerizable materials only change their properties (namely a phase transition from liquid to solid) upon exposure to light, advances in light-3DP technologies have enabled quick fabrication of high-resolution functional microdevices.

1.3.6. Direct Laser Writing

Direct laser writing (DLW) is a type of L-3DP where focused laser light is used to illuminate a single focal point either on the surface or within a volume of photopolymerizable materials; digitally controlled motorized stages and/or mirror galvanometers can then trace this illuminated focal point in 3D space to fabricate a 3D structure. Common examples of DLW technology include stereolithography (SLA) and multi-photon polymerization (MPP). SLA is a single-photon polymerization process in which the laser light source is raster-scanned across the surface of a liquid prepolymer, after which the focal plane is changed such that a new layer can be irradiated and adjoined in a layer-by-layer fashion to build the final 3D object. For this reason, SLA printers operate in what is called a "free-surface configuration," termed for how the light strikes the photopolymerizable resin at the air-liquid interface. The SLA's resolution limit depends mostly on the photopolymerizable material's absorption spectra, the laser's focal point size and the precision of the motorized stage.

In contrast, MPP operates not by projecting light onto a 2D surface, but rather into a 3D voxel within the depths of a photopolymerizable material. MPP materials undergo polymerization after the nonlinear absorption of two or more photons (in contrast to ones used in SLA, where a single photon is sufficient): to aid in this, MPP systems typically use high-intensity pulsed lasers with a very short pulse duration, i.e. femtosecond pulsing. Only the material at the laser's focal point undergoes polymerization due to the multi-photon absorption, since the intervening regions are effectively transparent to wavelength used and do not receive

enough energy to catalyze polymerization. Tracing the laser's focal point in 3D space then enables free-form fabrication of 3D structures, and MPP's precision enables the creation of sub-micrometer features in the regime of 100 nanometers in size.

1.3.7. Selective Laser Sintering / Melting

Selective laser sintering and selective laser melting (collectively known as powder-bed fusion techniques but labeled here as SLS/M) are loosely-related to direct laser writing in that a high-powered laser light is used to selectively sinter or melt, respectively, powdered materials into 3D structures. This is contrasted against photoinitiated chemical methods as seen in SLA or MPP 3D-printing, as SLS/M techniques utilize the energy of the laser to thermally heat the powdered building substrates until they physically fuse together. In most SLS/M setups, the laser light scans across the build substrate one layer at a time, after which fresh powdered material is mechanically-laid across as the next layer, ready to be fused to its predecessor. The resolution of SLS/M techniques depends on laser power, scanning speed, and the materials used, but often the final products are characterized on the basis of porosity – both pore density and pore size[12]. SLS/M is mentioned here for conceptual similarity to DLW, but as the majority of SLS/M materials are neither biocompatible nor biodegradable[13], beyond applications to certain tissue-engineered scaffolds[12] which are outside the scope of this review, fabrication of functional biomedical microdevices is limited.

1.3.8. Digital Light Processing

Digital light processing (DLP) 3D-printing, termed here as DLP-3DP, is a variant of "standard" SLA where, instead of a raster-scanned laser, a spatial light modulating (SLM) element, such as a liquid crystal display (LCD) or digital micromirror device (DMD), is used as a dynamically-changing "digital photomask" in projecting a two-dimensional (2D) plane of

specifically-patterned light[14]. By directing this light plane onto a vat of photosensitive substrate, DLP-3DP allows the photopolymerization of an entire 2D cross-section in a single exposure, subsequently enabling the fabrication of 3D constructs simply by changing the vertical position of the focal plane and selectively curing adjacent layers together. Similar to DLW-based techniques, the resolution limits for DLP-3DP is dependent mostly on the material's photopolymerization properties, the motorized stage's precision-of-movement, and the size of the projected "pixel". Two main configurations of DLP-3DP exist, termed: i) "free surface," where photopolymerization happens at the air-liquid interface and the build stage moves "downward" into the build vat of material, and ii) "bat" or "upside-down", where the light plane is directed through the bottom surface of a transparent build vat and the build stage rises upward from the floor, thus "pulling" the 3D object from the fluid as it prints.

Integral to DLP-3DP is the SLM element, which circumvents the need for physical photomasks by providing a digitally controlled, two-dimensionally projectable image. There are two main options for the SLM element: LCD or DMD, both of which can spatially modulate incoming light to produce an outgoing pattern. To briefly describe their modes of function: LCDs contain layers of liquid crystals and electrodes sandwiched between polarizing filters - incoming light is modulated by applying electrical current to the electrodes in desired areas, causing the liquid crystals there to align such that light cannot pass through. DMDs are opto/electromechanical arrays of micromirrors on individually addressable tilt switches, where each micromirror has an "on" or "off" state that allows selective reflection of incoming light - toggling individual mirrors in desired areas thus creates the desired images.

The use of LCDs as a DLP-3DP method was initially popularized by Bertsch et al. in 1997[15]. The LCD spatially modulated an expanded laser beam, where the transmitted light was

focused and directed to strike the surface of a motorized stage submerged in photopolymerizable resin. DMDs were originally manufactured by Texas Instruments in 1987. While they enjoyed commercial success in digital entertainment systems, their utilization in DLP-3DP methods happened later, with early examples utilizing visible and UV light demonstrated by Bertsch et al.[16] and Beluze et al.[17] in 1999. They utilized DMD chips with VGA resolution (640 x 480) in conjunction with broadband metal halide lamps, with desired wavelengths obtained by selective optical filtration. As understanding of DMD technology improved in sophistication and resolution, so too did DMD-based 3D-printing: Sun et al. in 2005 demonstrated high-aspect ratio structures, some with features as fine as 0.6 μm[18], and Lu et al. in 2006 showed the earliest known example of direct DMD-projection printing of biocompatible materials into 3D scaffolds for tissue engineering[14]. More recently, Tumbleston et al. demonstrated "continuous liquid interface production (CLIP)", where in the "bat" configuration of DLP-3DP, where a DLP is used to project a 2D light plane up into a vat of photopolymerizable resin – they demonstrated the use of an oxygen permeable membrane at the light's focal plane, such that prints-in-progress did not "stick" to the build vat floor, increasing the speed at which 3D-printing could occur[19].

1.4. 3D-Printing of Functional Biomedical Microdevices

The variety of 3D-printing methodologies has enabled the creation of a wide array of functional biomedical microdevices, encompassing different form factors and capabilities. In this section, we go over the use of different 3D-printing techniques for various biomedical microdevices, including micromachines, personalized medicines, biosensors and microfluidic devices.

1.4.1. Micromachines and Robotics

Microscale machines and robotics are often challenging to produce due to their small size, which scales with the complexity of the final device – mechanical features and forces that may be well understood at the macroscale may function differently at the microscale, necessitating material and/or design changes. As an example, we consider the problem of microscale propulsion: many microorganisms exist in fluid environments where viscous forces dominate inertial forces, otherwise known as the low Reynolds number regime. In such environments, traditional mechanical elements for locomotion, i.e. gears, motors, and shutters, are less effective due to enhanced friction at the microscale. Thus, when designing for locomotion in low Reynolds number regimes, often special design considerations must be taken into account, most notably Purcell's Scallop Theorem, which states that locomotion in fluids of low Reynolds number regimes must generally be of non-reciprocal and time-asymmetric character[20].

3D-printing has enabled innovative ways of actualizing microscale locomotion – Tottori et al., inspired by bacterial flagella, reported the fabrication of magnetically-controllable helical micromachines that can swim in both water and fetal bovine serum[21] **(Figure 2a)**. A two-photon polymerization (2PP)-based 3D DLW was used to fabricate helical structures in photoresist, followed by physical vapor deposition of magnetically-sensitive Ni/Ti bilayers; externally-applied rotating magnetic fields induced rotational motion in the helices, and thus propulsion. The flexibility of their 3D DLW system enabled iteration of their helical micromachines through various design parameters, such as length, diameter, and helical angle, with sub-micrometer resolution. For added utility, cage-like microholders were added to one end of the helices to allow for the manipulation and transportation of microparticle cargo, opening up potential

applications of such micromachines in biological sample manipulation, or targeted drug delivery at the microscale.

Purcell's scallop theorem holds generally for locomotion in Newtonian fluids, but in non-Newtonian fluids with shear-thickening or -thinning properties, i.e. hyaluronic acid, blood, and saliva, the Theorem no longer holds and low Reynolds Number propulsion can be realized with reciprocal motion[22]. Qiu et al. reported micro-swimmers with scallop-like shapes that can perform reciprocal opening/closing body-shape changes, and swim in non-Newtonian fluids. To fabricate these "micro-scallops," a MJM 3D-printer was used to create a negative mold out of a rigid thermoplastic material, which was subsequently cast with poly(dimethylsiloxane) (PDMS) and outfitted with two micro-magnets on the "shells" **(Figure 2b)**. By magnetically introducing a time-asymmetric stroke pattern in the opening/closing of the shells, and by exploiting the strain rate-dependent viscosity of the non-Newtonian fluids, Qiu et al. demonstrated the propulsion of their micro-scallops in both shear-thickening (fumed silica in poly(propylene glycol)) and shear-thinning (hyaluronic acid) solutions[22].

In addition to magnetic materials, biological components such as cells and/or tissues can be incorporated into soft robotics to provide the propulsive forces. Cvetkovic et al. developed a 3D-printed hydrogel "bio-bot" powered by the actuation of skeletal muscle strips **(Figure 2c)**[23]. An SLA 3D-printer was used to fabricate the millimeter-scale bio-bots out of poly(ethylene glycol) diacrylate (PEGDA) hydrogels. Their bio-bots featured two stiff pillars connected by a compliant beam, around which skeletal muscle myoblasts and extracellular matrix (ECM) proteins were polymerized into strips. An externally applied electrical field induced contraction in these muscle strips, in turn causing contraction in the bio-bot's pillars, ultimately mimicking an inchworm-like "crawling" movement. Cvetkovic et al.'s SLA 3D-printer's flexible control

over laser energy dosage enabled fabrication of bio-bots with tunable mechanical properties and structural conformations, allowing the testing of bio-bots with both symmetric and asymmetric pillar lengths, of which they found that asymmetric pillar designs afforded better controlled directional movement.

Besides biologics, additional utility can be gained by incorporating other components, such as functional nanoparticles – Zhu et al. reported 3D-printed biomimetic "microfish" with nanoparticle-granted locomotion and detoxification capabilities **(Figure 2d)**[24]. A DLP-3DP printer – a DMD-based microscale continuous optical printing system (μCOP) – directly printed the microfish, utilizing a photopolymerizable PEGDA-based hydrogel as the matrix material, additionally encapsulating functional nanoparticles. With the μCOP system's high resolution, Zhu et al. were able to print magnetic iron oxide (Fe_3O_4) nanoparticles and platinum (Pt) nanoparticles into the head and tail of the microfish, respectively, thus providing magnetically-controllable chemical propulsion in the presence of hydrogen peroxide as a fuel. As a proof of concept, they incorporated toxin-neutralizing polydiacetylene nanoparticles, granting detection and detoxification capabilities against the pore-forming toxin melittin. They further demonstrated that mobile microfish exhibited higher detoxification efficiency compared to stationary ones, and that the flexibility of their μCOP system enables the fabrication of freely-swimming microfish of various shapes and functional nanoparticle loadouts.

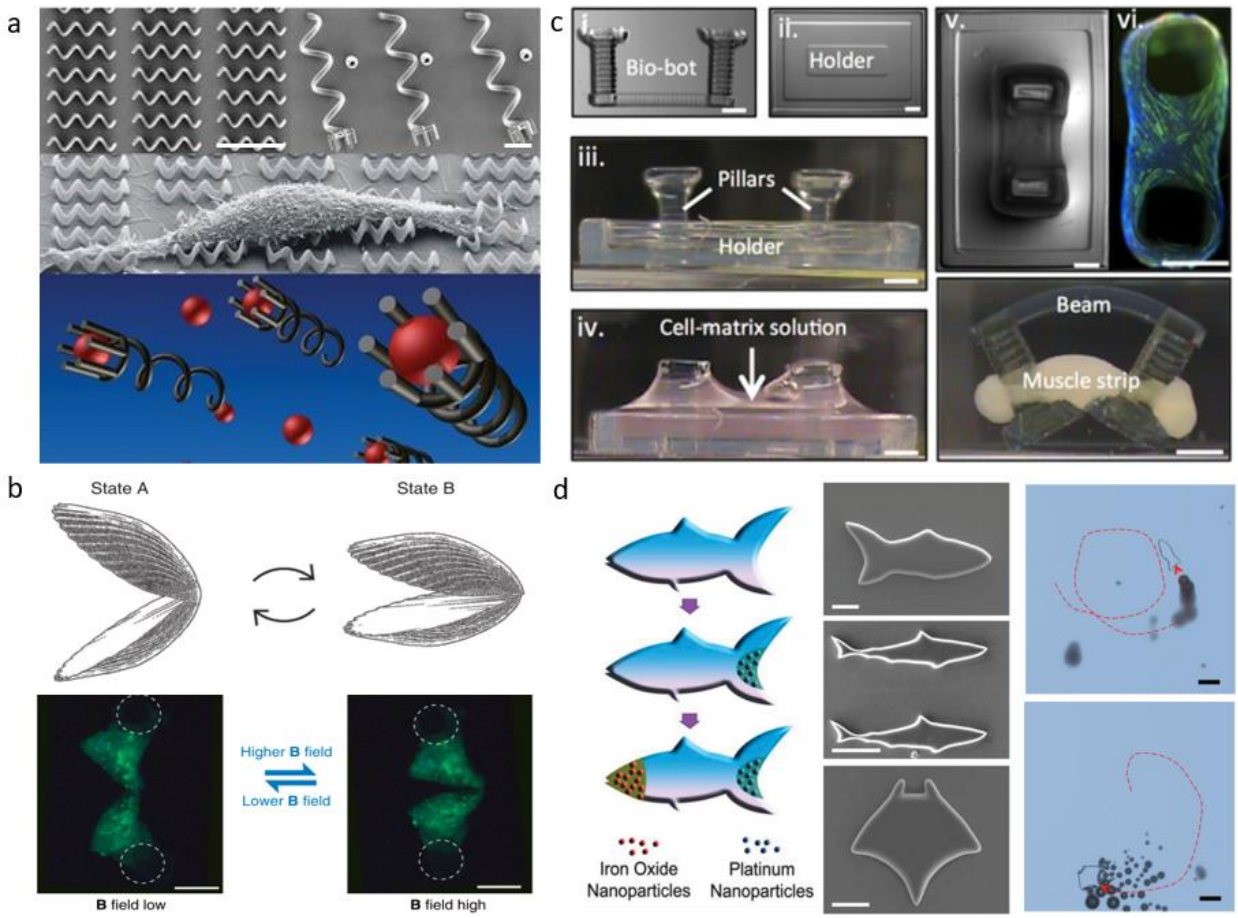

Figure 1.2: 3D-printing of micromachines and microrobotics.

(a) Magnetic helical micromachines fabricated by 2PP-based 3D-DLW21. Scale bar: 10 µm. Adapted with permission21. Copyright 2012, Wiley-VCH. (b) Magnetic micro-scallops capable of locomotion in non-Newtonian fluids, fabricated by MJM and PDMS microcasting22. Scale bar: 200 µm. Adapter under the terms of the Creative Commons Attribution 4.0 License22. (c) A hydrogel "bio-bot" powered by the actuation of skeletal muscle strips, fabricated by SLA 3D-printing23. Scale bar: 1 mm. Adapted with permission23. Copyright 2014, The National Academy of Sciences. (d) 3D-printed hydrogel microfish with diverse biomimetic structures and controllable locomotive capabilities24. Scale bar: 50 µm. Adapted with permission24. Copyright 2015, Wiley-VCH.

1.4.2. Pharmaceuticals and Drug Delivery

In the previous section, we discussed the development of micro-machines and robotics using different types of 3D-printing technologies. One potential application of such 3D-printed microdevices lies in the domain of customized medicines and targeted drug delivery, where

numerous efforts to explore the feasibility of 3D-printed approaches have been made[25–31]**.** Here, building off previous reviews in the field[32–35], we focus on recent examples of utilizing 3D-printing specifically for pharmaceutical manufacturing and drug delivery.

With pharmaceutical and biological compounds meant for human use, approval by the U.S. Food and Drug Administration (FDA) and similar institutions is a long and arduous process – the drugs themselves, as well as any excipients, solvents, and/or other process steps must be exhaustively tested. Inkjet-based and, more recently, extrusion-based 3D-printing technologies have come to the forefront of 3D-printing in pharmaceutical manufacturing, as with little-to-none mechanical modification they are well-suited to manipulating drug-excipient formulations, i.e. powder blends, aqueous binding, pastes, etc[33]. Scoutaris et al. explored the feasibility of using a modified inkjet printer to produce a 2D-array of microspot formulations for controlled drug release **(Figure 3a)**[26] – felodipine, an anti-hypertensive drug, was dispersed in the excipient (polyvinyl pirrolidone, PVP), and deposited as droplets with sub-100 μm diameters. The stable dispersion and intermolecular level interaction between the drug and the excipient were confirmed by atomic force microscopy (AFM) and attenuated total internal reflection infrared spectroscopy (ATR-IR). It was also found that the drug-release profile can be controlled by the drug-loading ratio, indicating the potential of using 3D-printing to tailor practical dosage forms to the individual needs of specific patients.

One limitation with the 2D micro-droplet deposition employed by Scoutaris et al. is that due to the 2D nature of the printed products, there is an upper limit to the amount of drug that can be loaded into the microdroplets. Khaled et al. addressed this limitation in their work, employing a nozzle-based extrusion 3D-printer to fabricate larger form-factor guaifenesin bilayer tablets (GBT) **(Figure 3b)**[31]. Their 3D-printed GBTs feature similar dimensions to their

commercial counterparts, and their formulations were adjusted such that they had comparable drug release profiles as well. By tuning the chemical composition of the drug and associated excipients, Khaled et al. was able to bring various physical and mechanical properties, such as weight uniformity, hardness, and friability into compliance with international standards set by the United States Pharmacopeia. The printing process in this study was achieved via a low-cost desktop 3D-printer operating at room temperature, underscoring the potential of using such techniques for printing personalized, point-of-care medicine in decentralized facilities, such as the patients" own homes.

Nozzle-based extrusion 3D-printers are flexible in both construction and utility, such that adding multiple nozzles enables multi-material 3D-printing, with each nozzle capable of extruding a different type of filament. Goyanes et al. employed such a setup to fabricate multi-drug caplets with two different types of internal structure – multi-layer, and core-shell configurations **(Figure 3c)**[30]. Paracetamol and caffeine were selected as the model drugs due to their prevalence in combinational use in commercial medicines. In the multi-layer configuration, caffeine and paracetamol layers were deposited in an alternating fashion, while in the core-shell configuration, they were the core and shell, respectively. Raman spectroscopy mapping was used to confirm the localization and separation of the two drugs in their respective compartments. Interestingly, unique drug release profiles were found for these two configurations due to their different internal structures. The multiplayer configuration showed a simultaneous release of the two drugs loaded in the adjacent layers, while with the core-shell configuration delayed release of the drug loaded to the core compartment was achieved and the lag-time could be modulated by the shell layer. This study highlights the advantages of 3D printing over conventional drug

manufacturing methods to fabricate devices loaded with multiple medicines and customize unique drug release profiles with specialized design configurations.

As another example of the viability and suitability of 3D-printing techniques for complex medication regimes, Khaled et al. demonstrated extrusion-based 3D-printing of a "polypill", a construct with five compartmentalized drugs, with two independently-controlled and well-defined release profiles, intended as a comprehensive cardiovascular treatment regime[29]. The polypill was formulated and printed such that there was an immediate release compartment of aspirin and hydrochlorothiazide, and three sustained release compartments of pravastatin, atenolol, and Ramipril, respectively **(Figure 3d)**. To prevent unwanted interaction between the five different drugs, a hydrophobic cellulose acetate shell with controlled porosity was printed first, then the separate drugs were extruded into their respective compartments. In addition to verifying immediate and sustained release profiles for their chosen drugs, X-ray powder diffraction (XRPD) and Fourier transform infrared (FTIR) data showed that there were no detectable interactions between the drugs and the polypill's excipients, as well as no detectable changes in the drugs' structural form. Their 3D-printed "polypill" concept represents not only improved on-demand personalization of drug combinations and release profiles, but a potential way to improve patient compliance with multi-drug and variable dosing regimens at the point of care. Indeed, the FDA recently approved the first 3D-printed pill for the drug levetiracetam in 2015, under the tradename Spiritam[36], underscoring the progress that 3D-printing has made in the pharmaceutical domain.

Light-based 3D-printing methods, such as direct laser writing (DLW) or stereolithography (SLA), have seen limited success on the pharmaceutical manufacturing front, likely due to the arduousness of approving photopolymerizable resins for human drug usage, in

addition to the potential degradation complications of using UV and/or visible light during the printing process[33]. That said, instances of using light-based 3D-printing as an approach for producing drug delivery methods have been reported, mostly in the form of microneedles as medical devices – a salient example being that of the successful delivery of an influenza vaccine utilizing microneedle arrays[37]. Conceptually, microneedles are miniaturized versions of the standard clinical hypodermic needle, but due to advances in microfabrication technology, they can be made to have more therapeutic utility: arrays of hollow microneedles can deliver or receive a broad range of compounds in clinically useful amounts while also avoiding some of the pitfalls of hypodermic needles, i.e. mishandling due to lack of training[38], or limited patient compliance due to pain[39] and needle-phobia[40]. More details and numerous examples of microneedle fabrication, function, and application can be found in other microneedle-specific reviews[38,41,42], but the next few examples focus on those microneedles that have been fabricated by light-based 3D-printing. Ovsianikov et al. used two photon photopolymerization (2PP)-3DP to fabricate hollow microneedles out of an organically modified ceramic material in an effort to impart durability during insertion into the skin as microneedle breakage could be detrimental to the therapeutic delivery process. Their microneedles were 800 μm long, with bases ranging from 150-300 μm in diameter, and were successfully tested on cadaveric porcine adipose tissue without microneedle fracturing[43] (see **Figure 3e** for a scanning electron microscopy (SEM) image of representative microneedles). Kochhar et al. utilized SLA-based 3D-printing to photopolymerize PEGDA hydrogels into microneedles containing bovine serum albumin (BSA) as a stand-in model drug[44]; these microneedles averaged 820 μm and 300 μm in average length and diameter, respectively. Their microneedles were found to be stable, of low cytotoxicity to human cells across three different cell lines, and most importantly, enhanced BSA delivery

through rat skin compared to passive diffusion, thus demonstrating the utility in transdermal therapeutic delivery. Lim et al. was able to successfully utilize DLP-3DP in printing microneedles onto a contoured surface, in contrast to most other fabrication methods that are limited mostly to planar surfaces (see **Figure 3f** to see the microneedle-laden contour). In a departure from the concept of having microneedles with drug reservoirs, Lim et al.'s microneedle array only penetrated the skin to provide enhanced absorption of topically-applied drugs, in this case a commercially-available topical diclofenac diethylamine 1.16% gel for pain associated with finger joint inflammation[45]. Their microneedles were 800 μm tall, with a base and tip diameter of 600 μm and 50 μm, respectively, and five-fold enhanced delivery of topical diclofenac via microneedles by 1.5 hours compared to intact skin permeation alone was able to be demonstrated. While Lim et al.'s microneedles were susceptible to fracturing at the tips, biocompatibility testing of their material deemed any tips that might be left behind in the skin to be non-irritative, an important consideration when dealing with numerous, fragile microneedles. Such examples showcase the potential for such microneedles to serve as an alternative to traditional hypodermic needle injections, and represent the continued advancement of a new paradigm in painless, versatile transdermal therapeutic delivery.

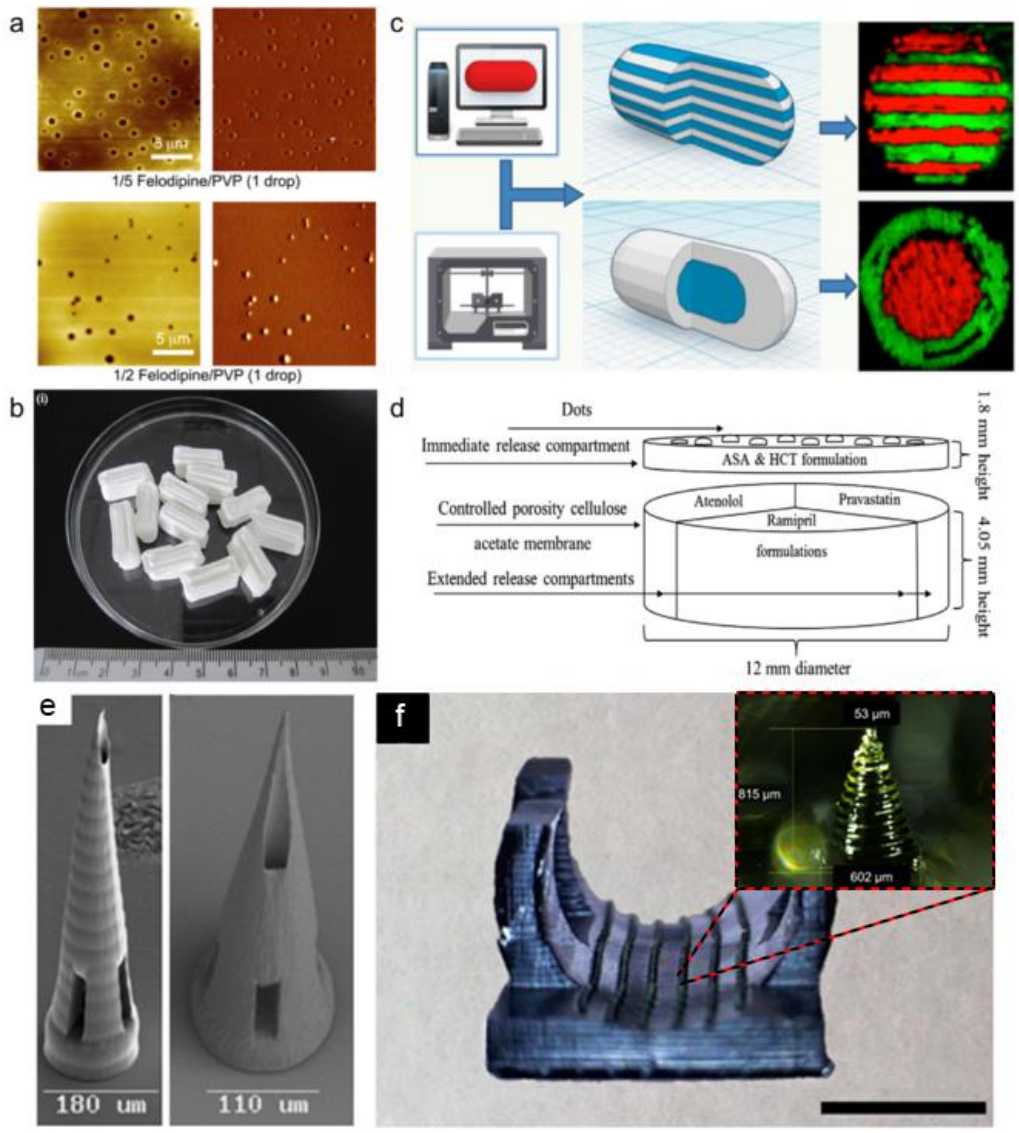

Figure 1.3: 3D-printing of medicines and drug delivery vehicles.

(a) 2D array of micro-spot formulations for controlled drug release, fabricated by an inkjet printer. Adapted with permission[26]. Copyright 2011, Elsevier. (b) 3D-printed guaifenesin bilayer tablets with sustained drug release profile, fabricated by an extrusion-based printer. Adapted with permission [31]. Copyright 2014, Elsevier. (c) Multi-drug caplets with two different internal structures: multilayer and core-shell, printed by a multi-nozzle 3D-printer. Adapted with permission[30]. Copyright 2015, American Chemical Society. (d) Schematic structural diagram of the 5-compartment polypill design. Adapted with permission[29]. Copyright 2015, Elsevier. (e) SEM image of MPP-3DP generated microneedles, fabricated from a commercially-available polymer-ceramic hybrid material. Scale bars: 180 µm for left, 110 µm for right. Adapted with permission[43]. Copyright 2007, The American Chemical Society. (f) DLP-3DP generated microneedles printed as part of a personalized contoured surface meant for splinting a finger with trigger finger disorder. Scale bar: 2 cm. Inset shows closeup view of one microneedle, sized 815 µm tall, 602 µm diameter base, and 53 µm diameter tip. Adapted with permission[45]. Copyright 2017, Institute of Physics.

1.4.3. Biosensors

Biosensors are a class of devices that interface biological analytes of interest with electrical, physical, and/or chemical transducers – they can "sense" the presence and/or amount of an analytical target, and thus are of significant interest to many industries, i.e. military, food science, and medicine[46]. The advance of the semiconductor industry in recent decades has created a robust variety of sensing technologies, but 3D-printers have found success in fabricating low-cost, custom-built objects that can not only function as supportive infrastructure for existing sensor technologies but also in making biosensing devices from the ground-up. Building off previous reviews in the field of 3D-printed biosensing technology[4,47,48], here we explore examples of 3D-printed biosensing platforms, ranging from assemblies of custom and commercial pieces to wholesale construction of new devices.

One class of technology significant to the biosensing domain is point-of-care devices – these devices are usually simple in construction, easy to operate, and portable, for decentralized use out in the field or on-demand. Assembling custom 3D-printed pieces with commercially-available technologies can enhance the properties of existing sensor technologies, such as allowing the interfacing of disparate components and increasing portability – an example of such comes from Gowers et al., whom utilized both DLP-3DP and MJM-3DP systems to fabricate microfluidic devices and electrode holders to not only pair with each other but also integrate with clinically-available microdialysis probes for real-time monitoring of metabolic activity[49]. They were able to demonstrate their setup in reporting the glucose and lactate levels of cyclists during exercise whilst the monitoring devices were attached to the cyclists themselves. Boehm et al. fabricated a microneedle-based fluid sampling system for assessing histamine contamination in tuna[50] – DLP-3DP was used to fabricate an array of fluid-capturing microneedles and a custom

lateral flow chamber, where commercially-available histamine-detecting test strip assays could be placed. Their microneedle arrays were stabbed into histamine-contaminated tuna for five seconds, where the fluid retained in the microneedles could then be flushed into their lateral flow chamber for detection via the test strips. While Boehm et al. observed a discrepancy between their custom system and the commercial kit at low histamine levels, improved statistical agreement was found between the procedures at higher histamine levels, which shows promise when combined with the fact that their microneedle-based assay utilized $1/7^{th}$ the volume of reagents and significantly less sample preparation as compared to the commercial kit's standard procedure.

Roda et al. combined a consumer-grade smartphone with parts fabricated via a low-cost FDM 3D-printing system to make a point-of-care biosensor package for measuring L-lactate levels in bodily fluids. A disposable 42 x 28 mm reaction analysis chamber was designed and fabricated such that it could attach to the smartphone, where its camera could measure the light produced by a luminol/H_2O_2/HRP CL enzymatic reaction carried out inside the attachment's body[51]. Their group was able to demonstrate real-time monitoring of lactate levels in human sweat during exercise. Similarly, Cevenini et al. utilized FDM to print smartphone-paired assay reaction chambers, reporting a cell-based toxicity biosensor utilizing the smartphone's camera to analyze toxicity-induced bioluminescence in genetically-engineered cells **(Figure 4a)**[52]**.** To improve assay longevity, the authors immobilized their chosen cells (human embryonic kidney cells transfected to produce luciferase) in agarose, and to provide ease-of-use they custom-coded their own smartphone application; their results were found to be comparable to commercial assays and centralized laboratory testing. These examples showcase the potential of portable,

point-of-care analysis that results from interfacing already existing technology with simple, low-cost 3D-printed plastics.

Beyond fabricating supporting infrastructure for existing sensor technology, 3D-printing also makes it possible to directly integrate sensing capabilities into the structures of printed constructs, thus more closely linking form and function. Miller et al. reported an electrochemical transducer platform consisting of DLP-3DP-fabricated hollow microneedle arrays[53], where the triangularly-sloped microneedles bore chemically-modified carbon fiber electrodes. These electrode-microneedle constructs were shown to be able to detect hydrogen peroxide and ascorbic acid, but in principle can be used to detect any analyte of interest so long as there is a corresponding chemical modification available for the electrodes used.

Kim et al. utilized DLP-3DP to directly photopolymerize polymer composites impregnated with piezoelectric nanoparticles into 3D microstructures, demonstrating free-form construction of piezoelectric polymers into arbitrary geometries[54]. As piezoelectric substances are capable of converting mechanical forces into an electric charge and vice versa, they show high potential for use in biosensing applications where traditional ceramic piezoelectric materials would be unsuitable. Gou et al. reported a biomimetically derived biosensor, utilizing DLP-3DP to fabricate a hybrid sensing/detoxification device – hydrogel composites were impregnated polydiacetylene nanoparticles and optically printed into 3D-microarchitectures resembling the hexagonally-based native architectures of liver lobules **(Figure 4b)**[55]. Their bio-inspired detoxification device demonstrated high efficacy in sensing, attracting, and neutralizing harmful pore-forming toxins.

In addition to static sensors, other groups have demonstrated sensors that can move and actuate to increase their functionality in addition to biosensing capability. Mandon et al.

demonstrated the use of DLP-3DP to fabricate antibody-laden hydrogels into 3D structures capable of directly interacting with their environment to enhance sensing sensitivity - one of their trials described a 3D-printed propeller composed of a PEG-DA hydrogel loaded with anti-brain natriuretic peptide (anti-BNP) monoclonal antibodies **(Figure 4c)** – rotating the propeller at 150 RPM in BNP solution increased the magnitude of chemiluminescent signaling five-fold compared to when it was not rotating at all[56]. Stassi et al. utilized DLP-3DP to fabricate bisphenol-A ethoxylate diacrylate (BEDA) into microcantilevers for mass-sensing applications – these polymeric microcantilevers incorporated acrylic acid into the prepolymer solution to impart biomolecular functionalization capability to the surfaces of the cantilevers **(Figure 4d)**[57]. Their one-step fabrication, combined with the intrinsic surface functionalization provided by the acrylic acid, was contrasted against traditional microfabrication processes for making silicon biosensing cantilevers. Stassi et al.'s microcantilevers were implemented in a gravimetric assay utilizing recombinant protein G and horseradish-peroxidase-conjugated goat anti-mouse immunoglobulin G, where they found that the presence of biomolecules on the cantilevers resulted in tangible shift of more than 20 times the cantilevers' mean relative resonant frequencies. Such devices demonstrate the potential for easily fabricated, "intrinsically functional" biosensors across a variety of sensing applications, and show promise in advancing 3D-printed biosensing platforms.

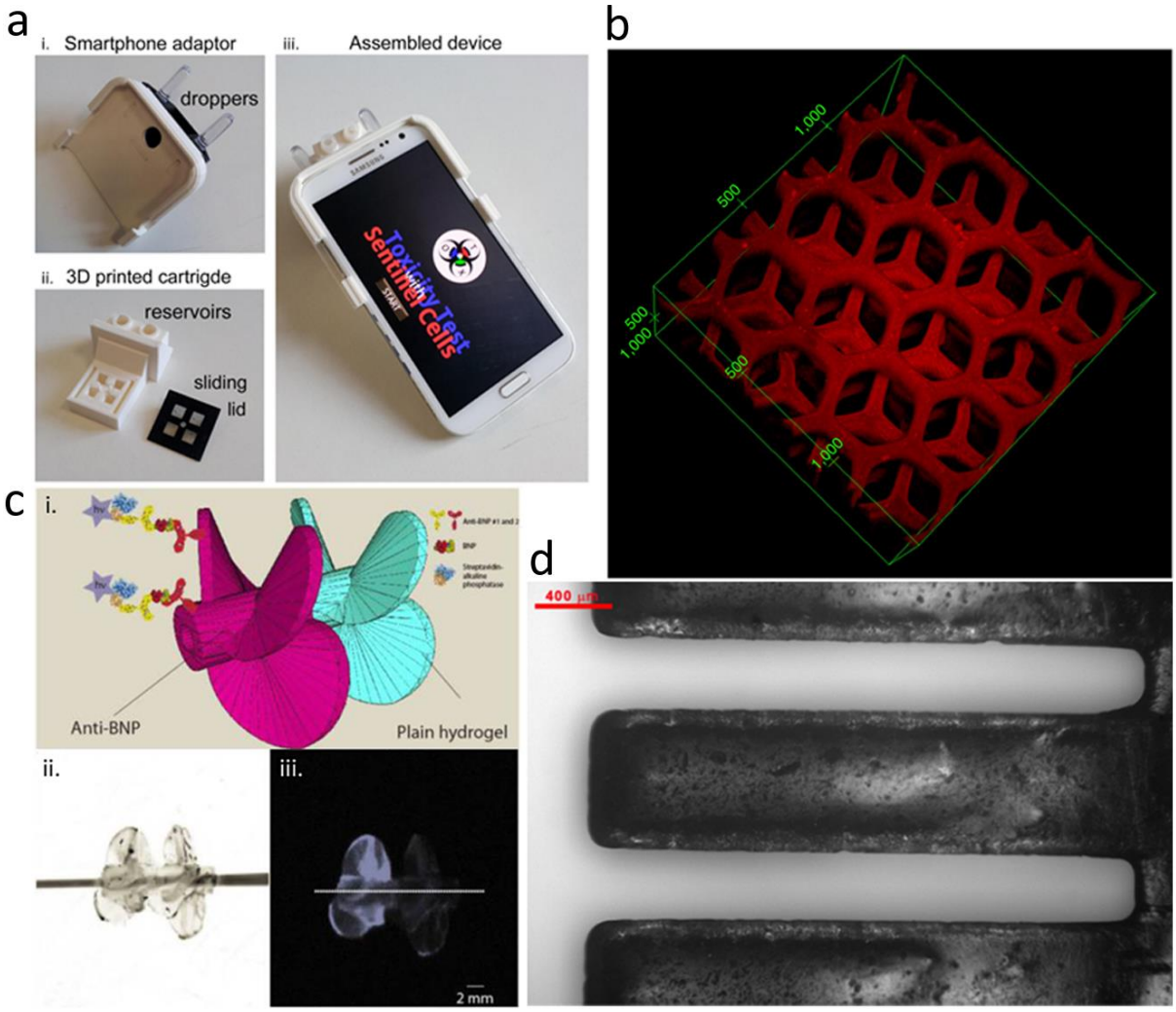

Figure 1.4: 3D-printing of biosensors.
a) Smartphone-coupled cell-based toxicity reactionware, printed via FDM-3DP[52]. Adapted with permission[52]. Copyright 2016, Elsevier. b) Dual-purpose toxin sensor and detoxification device based on liver microarchitecture, fabricated via DLP-3DP. Units shown: µm. Adapted with permission[55]. Copyright 2014, Nature Publishing Group. c) Impeller biosensor with antibodies incorporated into body fabricated via DLP-3DP; sensing efficiency increases when spun. Scale bar: 2mm. Adapted with permission[56]. Copyright 2016, American Chemical society. d) Mass-sensing cantilevers with incorporated functional groups, fabricated via DLP-3DP. Scale bar: 400 µm. Adapted with permission[57]. Copyright 2017, American Chemical Society.

1.4.4. Microfluidics

Microfluidic systems comprise the foundational basis for "micro total analysis" systems (μTAS), or "lab-on-a-chip" (LOC) devices, where microscale architectures can be used to precisely control small quantities of reagents and/or analytes of interest. Traditional methods of

manufacturing microfluidic systems are still largely rooted in cleanroom-based 2D photolithography and PDMS microcasting[58–60], but 3D-printing has gained prominence due to its design flexibility, rapid prototyping, and on-demand production capability. With an additive manufacturing approach, greater liberties can be taken in the construction of the final microfluidic device, with the possibility of creating architectures that may be challenging to produce using traditional methods – examples range from simply decreasing production time between design and fabrication (compared to photolithography/microcasting), the creation of challenging features such as high-aspect ratio 3D geometries for PDMS micromolding, or directly printing devices with isolated microchannels and void spaces.

Microfluidic devices crucially depend on precisely formed void spaces through which fluids, reagents, or other materials flow, and 3D-printers must take into account many different parameters to ensure success; examples include microchannel dimensions, interior surface smoothness, and sealable/perfusable interiors. Various groups have approached the problem of 3D-printing viable microfluidic devices, with differing levels of utility, complexity, and success - we review these bodies of work, building upon previous review articles in the field of 3D-printed microfluidics [5,61,62].

Morgan et al. recently reported using an off-the-shelf FDM-3DP to create flow-focusing junctions with channel dimensions as small as 400 μm, with the device itself exhibiting properties crucial to microfluidics, such as optical transparency and high structural strength (leak-free up to 2000 kPa)[63]. Bishop et al. utilized a commercial FDM-3DP to fabricate microfluidic devices geared toward Prussian Blue nanoparticle preparation and electrochemically-based hydrogen peroxide sensing, each with sealed, perfusable channels of 800 x 800 μm square dimensions[64]. Commercial entity Dolomite produces an off-the-shelf

desktop FDM-3DP system (Fluidic Factory) for direct fabrication of sealed, perfusable microfluidic devices out of cyclic olefin copolymer (COC) at a resolution limit of 320 μm (width) by 125 μm (height), and sells devices geared towards any number of biomedical applications, ranging from biomedical assays and diagnostics to chemical synthesis and drug development[65].

There are few examples of microfluidic devices made via multijet modeling (MJM)-3DP systems, in part due to the difficulty in removing the sacrificial materials utilized to fill the void spaces made during printing[66], but functional biomedical microdevices have nonetheless been reported. Erkal et al. utilized a commercially-available MJM 3D-printer to fabricate simple straight-channel microfluidic platforms that housed electrochemical electrodes[67]. Their featured electrodes were made of either glassy carbon or platinum black, for the detection of dopamine and nitric oxide, respectively, but the modular nature of their design allows for the possibility of multiplexing any potential number of electrochemical electrode setups. Begolo et al. utilized MJM-3DP to produce multimaterial "pumping lids" that could be placed over the inlet(s) of other microfluidic devices so as to provide equipment-free pressure and/or vacuum influence[68]. Causier et al. MJM-3D-printed a 4-piece "bubble pump" for use as a nuclear magnetic resonance imaging cell, and had a self-contained fluidic system comprised of a gas exchanger, pump, and circulator[69].

Among the light-based 3DP methods for fabricating microfluidic devices, most are centered on either directly fabricating the microfluidic features, or on producing master molds for PDMS microcasting. One of the relatively few MPP-3DP methods was reported by Lim et al., where a two-photon polymerization printer was used to fabricate a short, three-dimensional "crossing manifold micromixer" directly from two-photon crosslinkable resin[70]. With channel dimensions at 50 μm by 50 μm, and a series of horizontally and vertically aligned manifolds, the

micromixer was designed to quickly mix two liquids, and indeed homogenously distributed two fluids at 90% mixing efficiency within just 250 μm, or just 5 times the channel's width. Urrios et al. reported direct fabrication of millifluidic devices out of PEGDA-hydrogels, utilizing DLP-3DP to create optically-transparent, cytocompatible, and serpentine channels 1 mm in width and 2 mm in height **(Figure 5a)**[71]. Liu et al. recently demonstrated a combination passive mixer and cell culture chamber, utilizing DLP-3DP to fabricate variable-height master molds out of PEGDA hydrogels, upon which PDMS microcasting was performed to create the final device **(Figure 5b)**[72]. To demonstrate the device's utility, its variable height steps were used to passively mix gelatin methacrylate-based hydrogels and a fibroblastic cell line in a short length scale. Afterwards, they utilized the non-contact nature of DLP-3DP to fabricate additional structures inside the already-completed device, with the PDMS" optical transparency allowing direct photopolymerization of the cell-laden hydrogel inside the device's main chamber. Rogers et al. implemented DLP-3DP to produce microfluidic devices with integrated membrane-based valves[73], with the valves containing horizontal, rectangular cross-sectional inlets and outlets with dimensions as thin as 350 μm wide and 250 μm tall, in addition to vertical cylindrical control and flush ports with a diameter of 210 μm. The valves were demonstrated to work for up to 800 actuations. The ability to directly print the membrane-based valves onto glass enhances the likelihood of being able to include various substrates in printing, presenting the potential to lower the barrier-to-entry and aid in further research regarding lab-on-a-chip technologies.

Microfluidic devices are often custom-built for a single application, and unless care is taken to generalize their design, they may have limited use in other applications. Combined with the fact that microfluidic device production currently has a high cost-of-entry in terms of both skill and capital, there is interest in creating modularizable microfluidic components, for the sake

of accessibility. Bhargava et al.[74], Sochol et al.[75], and Tsuda et al. [76], are all examples of groups utilizing 3D-printing to fabricate discrete, modular, and networkable microfluidic components, with the intention that any number of potential components that can be mixed-and-matched at the end-users' discretion to create custom devices. As a more detailed example, Bhargava et al.'s study features SLA-3D-printed fluidic components 1 mm in length and fluidic cross-sections 750 μm in diameter, with standardized inlets and outlets such that they can be fitted together to form a collective microfluidic device. They demonstrated reconfigurable and tunable microdroplet generators, as well as a passive mixing device **(Figure 5c)**, with varying designs for each. Studies such as these aim to lay the groundwork for standardized "libraries" of microfluidic components, with the hope that advanced designs of high utility can be created easily by people who do not have the access, training, or time for cleanroom-grade micro-stereolithography.

There have been efforts to characterize the suitability of various 3D-printing types in fabricating microfluidics devices: if 3D-printers of different operating principles are tasked to make the same device, the resultant devices often will not be identical in form or function as an inherent consequence of the 3D-printers' operation. Lee et al. conducted a comparative study on MJM- and FDM-3DP capabilities in fabricating microfluidic rotational-flow devices and gradient generators, while also assessing parameters such as printer resolution, surface roughness, and biocompatibility[77]. As an example of comparative capability, they found that feature sizes under 100 μm were unattainable with both their MJM and FDM 3D-printers, but they were able to achieve a 5% accuracy rating for feature sizes above 500 and 1000 μm, respectively. Ultimately, they found that their chosen MJM 3D-printer was superior to that of their chosen FDM 3D-printer in terms of spatial accuracy, resolution, and smoothness across all three axes of motion, with an average deviation of 25.2 μm across all measurement series, as compared to 67.8

μm for the FDM; although they acknowledged that specialty tooling such as finer nozzles and motion controllers for their FDM 3D-printer could mitigate these shortcomings.

Macdonald et al. conducted a similar study, this time a direct comparison of their FDM, MJM, and DLP-based 3D-printers in fabricating a single, straight microfluidic channel - each of these were evaluated in the context of mixing efficiency of two flowing reagents **(Figure 5d)**[78]. Their FDM printer produced the roughest surfaces as an inherent consequence of fusing large, circular filaments, but performed the best at mixing as a result (100% mixing within 15 mm of the inlet for all flow rates tested). Their DLP 3D printer produced the smoothest features with the highest resolution, but as a result the microfluidic channel experienced a maximum mixing efficiency of only 32% at 25 mm from the inlet at 25 μL/min. Their MJM printer tread a middle-ground between the FDM and DLP 3D-printers – there was sidewall roughness in the channel due to the 16 μm layer size inherent to their MJM setup, but they were able to show 83% mixing at 25 mm from the inlet at 100 μL/min flow rates. While the authors cautioned championing any one modality as "the best", they did suggest optimum applications for each printing modality that took advantage of how each printer type inherently functioned: FDM 3D-printers would be well-suited for creating passive micromixers, or applications where mixing has no impact on the outcome; MJM 3D-printers would be optimal for complex geometries that do not require high precision; and DLP 3D-printers would be well-suited for microfluidic applications where precise control of features and fluidics is critical[78].

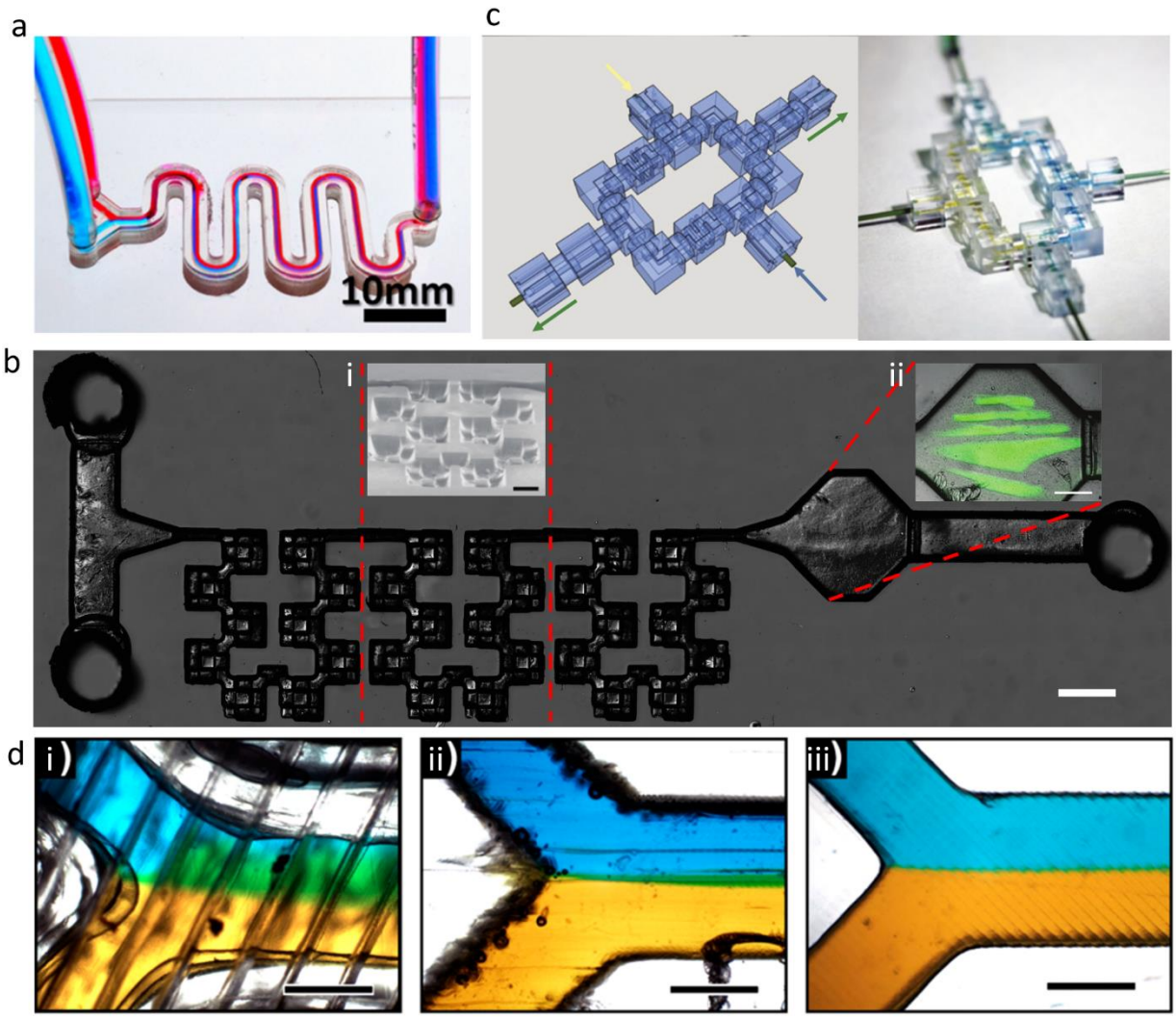

Figure 1.5: 3D-printing for microfluidics.

a) Direct DLP-3DP of millifluidic serpentine channels in PEGDA hydrogels. Scale bar: 10 mm. Adapted with permission[71]. Copyright 2016, Royal Society of Chemistry. b) 3D passive mixer and biofabrication chamber, constructed via PDMS microcasting of a DLP-3D-printed master mold. Scale bar: 1 mm. i) inset: SEM image of mixing region, pitched at 45 degrees. Scale bar: 500 µm. ii) inset: biofabrication chamber, where 3D cell-laden constructs were printed. Scale bar: 500 µm. Adapted with permission[72]. Copyright 2016, Royal Society of Chemistry. c) Discrete, modularizable, and networkable microfluidic components for user-defined devices, fabricated via DLP-3DP. Example shown is a single-circuit mixer; Left: 3D model; Right: device in reality. Connectors are 1mm in length, with fluidic cross sections at 750 µm in diameter. Adapted with permission[74]. Copyright 2014, The National Academy of Sciences. d) Comparison of Y-combinator straight-channel mixer, printed using i) FDM, ii) MJM, and iii) DLP 3DP, respectively. Scale bars: 500 µm. Adapted with permission[78]. Copyright 2017, American Chemical Society.

1.5. Discussion and Future Outlook

The rising popular of 3D-printing in many sectors of the consumer and professional market have driven significant leaps in sophistication and capability. Such advances improve the ability to actualize challenging manufacturing ideas, and as demonstrated in this review, have resulted in novel and functional biomedical microdevices. However, an important consideration is that device design can be highly situationally dependent, and, depending on the application, there are different 3D-printing limitations and challenges to overcome, which can encompass parameters ranging from material workability and suitability to construction speed and print resolution (**Table 1)**. We acknowledge that other reviews in the field have covered the technical minutiae of various 3D-printers" capabilities[3,5,32,33,66,79] - instead, here we consider in a more general sense the concepts, limitations, and relative advantages/disadvantages a potential 3D-printer user might consider important when selecting a particular modality for their specific application. Additionally, we discuss potential future directions the field of 3D-printing functional biomedical microdevices may take.

1.5.1. Considerations in Selecting a 3D-Printing Modality

Fundamental to any given 3D-printer's operation is the ability to add and/or shape material in a precise manner, and any movement in 3D space necessitates fine control of whichever mechanisms performing the construction operations. While 3D-printing technology has improved immensely in recent years, there still exist tradeoffs where one type of printer will excel in one domain compared to another.

1.5.2. Materials Selection

From a materials standpoint, 3D-printing technology has a large variety of materials to choose from, although the exact choice will differ depending material property suitability, and

the specific application's requirements. Sometimes these choices can be constrained by the materials' workability, or economic costs in acquiring and/or modifying materials for use, while other times the choice is an inherent consequence of how different classes of 3D-printers are often optimized for a specific type or category of material, usually tied closely to the method by which the 3D-printer operates.

As an example, extrusion-based 3D-printers (E-3DPs) at their most fundamental, depend on the controlled release/deposition of material through a forming tool, whether that be a nozzle, dropper, or some other physical aperture. The method of forcing extrusion can vary as well, from the use of mechanical feeding, positive/negative pressure, and/or hydrostatic forces, but ultimately E-3DPs are restricted to materials capable of liquid-like flow, such as hydrogels, viscoelastics, and/or thermoplastic polymers. FDM 3D-printers, the more restricted counterpart to ordinary nozzle-based 3D-printers, would be limited to thermoplastic materials extruded through a heated forming nozzle. With most MJM 3D-printers on the market, such as the ones available by the company Stratasys (CA, USA), their material choices are restricted in a similar fashion to that of the nozzle-based and FDM 3D-printers in that the build substrate must be flowable, but are unique in that the material must also be crosslinkable post-deposition, i.e. UV photopolymerizable in the case of Stratasys systems.

Light-based 3D-printers (L-3DPs), such as DLW, MPP, and DLP-3D-printers all crucially depend on photopolymerization, and as such are limited to materials that are liquid, photosensitive, and transparent (or at least sufficiently translucent). As most L-3DP methods happen in a build vat containing an excess of the photosensitive substrate, there is none of the selective deposition of materials to desired locations as with other E-3DP methods, raising an economic resource concern

Table 1.1: Feature comparison of E-3DP and L-3DP techniques in relation to functional biomedical micro-device fabrication

	Extrusion-based 3D-printing (E-3DP)			Light-based 3D-printing (L-3DP)		
Features	**Nozzle**	**FDM**	**MJM**	**SLA**	**MPP**	**DLP**
Operating principle	Controlled deposition of flowable materials via nozzle	Filamentous deposition of thermoplastic polymers via nozzle	Deposition of crosslinkable polymers via inkjet heads	Raster-scanned laser photopolymerization of photosensitive substrates	Photopolymerization via non-linear multiple photon absorption	2D cross-sectional photopolymerization of photosensitive substrates
X/Y Resolution	~5 μm - 200 μm	~5 μm – 200 μm	~50 μm / 100's of DPI	Light spot-dependent; can be sub-micrometer	Can defeat diffraction limit; sub-100 nm	Projected pixel size-dependent; can reach 1 μm
Speed	~500 μm/s - 24 mm/s	~sub-mm/s – 6 mm/s	~1-40 mm/s	~100's μm/s – cm's/s	~80 nm/s - 2 cm/s	~25 - 1000 mm/min
Advantages	Can utilize wide variety of materials, including biological	Tabletop form factor and cheap materials	May print multiple materials	Laser light enables high resolution prints at reasonable speeds	Can produce much smaller structures compared to other L-3DP techniques	2D projection enables higher throughput compared to raster-scanning
Limitations	Print resolution limited by extrusion aperture and motion controller precision			Print resolution can suffer non-specific photopolymerization due to light leakage into surrounding areas		
	Viscosity of substrate can impact nozzle performance	Circular cross-sections can prevent inter-filament and inter-layer fusion	Requires sacrificial support materials; removal can be difficult	Limited mainly to UV-sensitive resins; low throughput	Slow speeds limit larger form-factor fabrication; costly equipment	Prints require large volumes of photopolymerizable; wasted material can become cost-prohibitive
References	80–84	83–86	5,83,84,87	88–93	88–94	5,83,95

of wasting unpolymerized materials in the vat. Finally, in the context of biomedical applications, material biocompatibility is a key consideration – most solutions available on the commercial market are not optimized for biocompatibility, and often proprietary formulations make modifications difficult[5]. This sometimes requires users to come up with their own biocompatible materials, or resort to working with known biocompatible materials.

1.5.3. Resolution and Feature Size

From materials selection, we transition to resolution and feature size considerations: with E-3DPs, assuming that their extruded material does not experience post-deposition changes in size, are ultimately limited by the precision of their motion controllers and the physical size of their extrusion aperture(s), which in recent literature has reached a lower limit on the order of several microns for certain non-biological microextrusion printers[84]. In general, this resolution stands to be improved if finer nozzle features and motion control mechanisms are implemented. With FDM printers in particular, the nature of thermoplastically-extruding large filaments means that i) the filament sizes can sometimes be larger than the sizes of the desired features, ii) topologically, the filaments are round and can result in unwanted geometries, and iii) the bonding between adjacent filaments (and thus adjacent layers) is mechanically weak, thus prone to failures, leakages, and unwanted material properties. However, the advent of finer nozzle sizes and techniques for improving inter-filament and inter-layer fusion[95–97] have enabled easier fabrication of 3D constructs, and will only improve with time. Modern MJM-3DPs, such as ones built by Stratasys (CA, USA), often specify resolution in terms of dots per inch (DPI) through arrays of nozzles just 50 microns in diameter[98], but can suffer "smearing" at smaller feature sizes due to the action of a leveling device that smooths each layer after deposition[99].

With L-3DP systems, resolution is ultimately determined by the focal spot size of the incident light, and in the case of free radical photopolymerization, secondary consideration is given to the diffusion of free radicals outward from irradiated zone. Focusing optics can be used to further shrink the spot size of incident light – in the case of recent advances of DLP-3DP, resolutions of 1 micron can be achieved[83], and in the case of MPP-3DP, the diffraction limit can be overcome to achieve resolutions sub-100 nanometers[88,89,94]. Additionally, as the build material is liquid and transparent (or at least translucent), there is potential for non-specific photopolymerization to occur as light "leaks" deeper into the areas around the intended irradiation zone, which in turn further compounds the issue of unwanted free radical polymerization. To mitigate these issues, one potential solution might be to chemically modify the build material to include free radical absorption and/or light quenching molecules, i.e. Sudan I, 2-Hydroxy-4-methoxy- benzophenon-5-sulfonic acid (HMBS), or 2,2,6,6-tetramethylpiperidine 1-oxyl (TEMPO)[100,101],thus limiting the spread of non-specific polymerization.

1.5.4. Speed and Throughput

In terms of speed and throughput, 3D-printing inherently involves the successive building of layers in three-dimensional space, and how those individual layers are built can be loosely grouped into two paradigms: i) serial printing, where each layer is formed drop-by-drop or line-by-line (e.g. nozzle/FDM-3DP, DLW-3DP) before moving on to the next layer; and ii) parallel printing, where individual layers are fully-formed whole before being joined to the next layers (e.g. MJM-3DP, DLP-3DP). Parallel printing can also encompass efforts to employ multiple serial mechanisms in tandem, such as utilizing more than one extruder in nozzle-based or FDM-3DP[102], or multiple laser beams in SLA[103] or MPP-3DP[94] techniques.

3D-printers that operate in the serial fashion must form every feature of a given layer before moving onto the next – thus total print speed is bottlenecked by how fast the printing mechanism can physically move while still retaining print fidelity. As examples, consider how FDM-3DP is limited both by how fast its printhead can traverse its motion of axes; going faster than the printer's ability to spool thermoplastic filament and/or faster than what the extruded filament can handle during its post-deposition cooldown phase can negatively impact print quality. SLA-3DP can raster scan a laser very quickly across a resin's surface using mirror galvanometers, but is limited by the stop-and-go motion of its vertical stage as it passes from one layer to the next – some commercial SLA-3DPs have wipers that physically smooth the resin surface between every layer, further bottlenecking the print speed[104]. MPP-3DP systems can freely trace a laser in 3D space via mirror galvanometers, but time required to produce high-resolution features increases cubically as a result of needing to raster-scan in three dimensions[94]. In terms of throughput, attempting to fabricate multiple objects in one build session using serial printing will increase the build time – assuming all of the devices fit within the 3D-printers available build volume, this means that the printing mechanism(s) must now attend to each feature of a given layer for every additional device before it can begin to pass onto the next layer.

In contrasting serialized printing with parallel printing, entire 2D cross-sections can be formed at once in a single pass before moving onto the next layer. In MJM-3DP, parallel printing is achieved by virtue of having multiple printheads with many dispensing nozzles – an exemplar of this the Stratasys-built Objet500 Connex3[98], where eight printheads with 96 nozzles each move in tandem to deposit tiny droplets of photocurable polymer at an *X/Y* resolution of 600 dots per inch (DPI). Provided the total footprint of the intended 3D object is not larger than the available footprint of the printhead architecture, a single pass can deposit an entire layer of

features before moving onto the next layer. Combined with the ability to dispense multiple materials at controlled locations, MJM-3DP can create complex multi-material 3D objects in a shorter timescale than their serialized counterparts. DLP-3D-printers, by virtue of being able to project an entire 2D light plane, are speed-limited mostly by the vertical movement of the stage responsible for moving the projected focal plane within the build volume, with secondary consideration for the substrate's photoinitiation efficiency. Faster movement of the stage will often decrease build time, although this may be at the expense of build quality and feature resolution[19].

Many of the considerations discussed thus far are inextricably linked in compromise – larger and more complex objects will take more time to complete than smaller and simpler objects; build quality and feature resolution are often inversely proportional to speed; and attempting to print many objects may or may not slow the total build time, depending on the methodology used. By discussing some of the relative advantages/disadvantages associated with the 3D-printing techniques in this review, it is our hope that aspiring 3D-printer users have a better understanding of which techniques may best suit their specific application needs.

1.5.5. Future Outlook

Since the 2009 patent expiration on fused deposition modeling (FDM)-type 3D-printing, and the expiry of key stereolithography patents in 2014[66], public awareness of 3D-printing has grown, bringing attention not only to the various technologies that comprise the field, but also to their extensive manufacturing potential. 3D-printers of all kinds have become cheaper, smaller, and more sophisticated in the last decade, increasing public access and ease of production for the scientific, medical, and research communities. In the context of functional biomedical microdevices, 3D-printing represents a paradigm shift in manufacturing, as it significantly

reduces the amount of time and resources spent in turning a conceptual idea into reality, compared to traditional techniques such as photolithography, subtractive manufacturing, or high-throughput injection molding. It becomes possible to rapidly prototype and iterate through designs on a small scale before committing resources to large-scale and costly manufacturing processes, thus advancing research and development on both data and economic fronts. The capability of 3D-printing with multi-materials also enables the one-step fabrication of microdevices with functional parts, potentially eliminating aspects of the traditional multi-step manufacturing processes. For instance, in the context of microfluidic device manufacturing, instead of separately constructing and assembling the tubes, valves, and chambers, the entire microfluidic device could potentially be 3D-printed in one step, as well as other functional elements such as sensors and actuators if the application requires them. In this way, 3D-printing makes the manufacturing of more complex and versatile biomedical devices possible.

We also consider a domain only lightly discussed in this work - the frontier of tissue-engineered systems, such as vasculature and disease models. Of the many goals of tissue engineering, two prominent goals are: to produce tissues and organs that are of clinical-relevance for transplantation, and to create tissue-engineered models for investigating disease pathologies and/or pharmaceutical compound screening[1]. However, one of the fundamental limitations in producing clinical-scale tissues is the difficulty in producing functional vasculature – the diffusion limit of nutrient/waste transport in tissues is limited to the regime of 250 μm, and as such any larger-scale tissue-engineered constructs will critically require vascularization to maintain viability or be clinically-relevant[83]. This scenario is where microfluidic devices may fill an important niche in tissue engineering, as vasculature and microfluidic channels are similar from a geometric and fluidic perspective[105].

Producing biocompatible structures capable of supporting tissue-scale growth still remains an active area of research, as not all 3D-printing technologies support biocompatible materials, and fewer still are capable of producing vascularized tissues of meaningful utility. Existing methods for producing vasculature and tissue constructs vary greatly, from using sacrificial placeholders to directly printing negative spaces, but all invariably involve some manner of creating hollow, perfusable, biocompatible scaffolds in conjunction with cells of interest. Of the E-3DP and L-3DP methods described, several salient attempts at vascularization and tissue models have been reported: one example is Zhu et al.'s DLP-3DP fabrication of a multi-cellular, prevascularized tissue construct, where endothelial cells formed lumen-like structures *in vitro*, and successfully demonstrated host vasculature integration when implanted *in vivo*[106]. Another is Ma et al.'s DLP-3DP-based fabrication of a liver tissue construct, where human-induced pluripotent stem cell-derived hepatic progenitor cells and supportive cell types were spatially-patterned into hexagonal patterns reminiscent of liver lobule architecture[107]. Yet another is Kolesky et al.'s utilization of a nozzle-based 3D-printer, where sacrificial hydrogels were embedded in a block of gelatin methacrylate, then flushed and perfused with endothelial cells[108] - this method was later scaled up for larger constructs on the order of 1 cm[109]. Efforts such as these signal a brighter future in the domain of functional biomedical microdevices, as greater strides in 3D-printing biologically compatible materials will further enhance medical healthcare technology, regenerative medicine, and pharmaceutical drug discovery.

1.6. Conclusions

The functional biomedical microdevices described in this review showcase the wide range of capabilities and types of devices that 3D-printing can produce, and we believe that technological progress in the 3D-printing domain is inevitable. We have seen the sheer range of

applications that can be wrought, from micromachines and microfluidics to pharmaceuticals and biosensors. The capital cost, tooling, and maintenance requirements of 3D-printers of varying modalities shrink by the year, to the point where consumer-level desktop 3D-printers can be bought for recreational purposes. The fabrication capabilities of even consumer-grade 3D-printers can print features at the scale of tens of microns[104] with a wide variety of materials, and it is expected that both the cost and resolution of such printers will continue to shrink in the near future. The increasing popularity and decreasing cost of 3D printers will significantly increase its accessibility in both scientific research and industry to develop functional biomedical microdevices with less effort and better performance, at an accelerated yet economical pace. While we acknowledge that we have not covered all of the available technologies and capabilities of 3D-printing, we can see from the work discussed from just this past decade that in the context of functional biomedical micro-device production, technological progress in 3D-printing has enabled creative and innovative studies to flourish. We see an exciting time ahead for the future of 3D-printing, and as the various barriers from conception to production continue to be overcome, humanity's ability to advance research and development, bolster personalized healthcare, and improve the quality of life for all will continue to evolve.

Thus, having conducted a review of 3D printing modalities in the context of fabricating functional biomedical microdevices, we transition to this dissertation's narrative. Here, we focus on the utilization of Digital Light Processing (DLP)-based 3D printing in the context of tissue engineering and microphysiological systems, which are areas that are under active and enthusiastic investigation from both the scientific and industrial communities:

- In Chapter 2, we explore a particular application of DLP 3D printing as a dual-purpose microfluidic and *in situ* tissue scaffold fabrication technique - we developed a 3D passive

micromixer, evaluated its mixing efficiency, and leveraged the light-based nature of DLP 3D-printing to fabricate user-defined hydrogel scaffolds *inside* already-completed microfluidic devices, which would be challenging using traditional extrusion-based 3D printing techniques.

- In Chapter 3, we explore the extension of DLP 3D printing into *in situ* well-plate 3D printing in the context of high throughput pharmaceutical compound screening – the drug discovery-to-market pipeline has a high failure rate, in part due to the difficulties in transitioning between the various stages of 2D monocultures, animal models, and human clinical testing. We generated 3D bioprinted liver-based tissue scaffolds at high throughput rates in well-plates, quantified the speed and dimensional accuracy of printing, conducted chemotherapy testing as a stand-in for well-plate assays, and demonstrated multi-cellular 3D bioprinting.
- In Chapter 4, we explore the merging of DLP 3D printing and microfluidics in the production and validation of a novel Placenta-on-a-Chip microphysiological system – here we leverage DLP 3D printing to fabricate a 'hybrid' open/closed 3D microfluidic barrier model, utilize multiple primary cell sources to generate a tri-coculture *in vitro* model, as well as verifying tri-coculture viability, barrier integrity, and transfer rate of solutes-of-interest.

1.7. Acknowledgments

The work was supported in part by grants from the California Institute for Regenerative Medicine (Grant No. RT3-07899), National Institutes of Health (Grant Nos. R01EB021857, and R21HD090662) and National Science Foundation (Grant Nos. CMMI 1547005 and CMMI-1644967). Chapter 1, in full, includes a reprint of the published article: "3D-Printing of Functional Biomedical Microdevices via Light- and Extrusion-Based Approaches." The dissertation author was the primary investigator and author of this work.

CHAPTER 2: DIRECT 3D-PRINTING OF CELL-LADEN CONSTRUCTS IN MICROFLUIDIC ARCHITECTURES

2.1. Abstract

Microfluidic platforms have greatly benefited the biological and medical fields, however standard practices require a high cost of entry in terms of time and energy. The utilization of three-dimensional (3d) printing technologies has greatly enhanced the ability to iterate and build functional devices with unique functions. However, their inability to fabricate within microfluidic devices greatly increases the cost of producing several different devices to examine different scientific questions. In this work, a variable height micromixer (VHM) is fabricated using projection 3D-printing combined with soft lithography. Theoretical and flow experiments demonstrate that altering the local z-heights of VHM improved mixing at lower flow rates than simple geometries. Mixing of two fluids occurs as low as 320 μL min^{-1} in VHM whereas the planar zigzag region requires a flow rate of 2.4 mL min^{-1} before full mixing occurred. Following device printing, to further demonstrate the ability of this projection-based method, complex, user-defined cell-laden scaffolds are directly printed inside the VHM. The utilization of this unique ability to produce 3D tissue models within a microfluidic system could offer a unique platform for medical diagnostics and disease modeling.

2.2. Introduction

As trends toward improving global public health and point-of-care technologies gain traction in research and development, Lab-on-a-Chip (Loc) technologies designed for microfluidic manipulation of biological fluids and/or multi-species mixtures continue to be active areas of research.[110–112] LoC devices are especially attractive due to use of microfluidics to integrate

multiple fluidic and analytical processes, giving them many-fold advantages[113] over traditional laboratory functions, such as: 1) reduction in sample processing runtime, resource cost, and volume, 2) simplicity of assay deployment and user training, and 3) multiplexability and batch processing capabilities.

One function crucial to microfluidic LoC devices is the ability to mix and manipulate disparate substances to any desired degree.[114] However, microfluidic flow conditions are typically laminar and uniaxial, resulting in mixing being dominated by molecular diffusion rather than convective mass transfer.[113] Consequently, cells, particles, or other flowing species present tend to stay in their own fluidic streamlines, minimizing interactions with other species and/or critical structural features of the LoC device.[113] Current research in microfluidic mixers have yielded results in the form of active micromixers, which rely on externally-supplied energy and equipment to drive mixing, thus adding complexity to their design, construction, and operation.[115] Alternatively, passive micromixers' only energy requirement comes from the initial fluidic driver, otherwise utilizing device-level structural features for enhanced diffusion and advective mixing.[114] While planar passive mixers have been successful in microfluidic mixing due to their simplicity of design and construction, there is potential to improve efficiency by extending feature geometries into the third dimension such as with three-dimensional (3d) passive micromixers[116–118], but these can be onerous to manufacture due to limitations in current manufacturing methods.

The current gold standard in microfluidic device fabrication is soft lithography, a technique where a 'soft' material like polydimethylsiloxane (PDMS) is used to cast a 3D master molding with micrometer-scale features[119]. Traditional methods for 3D master mold fabrication often involve cleanroom-gated silicon wafer-based photolithography, where multiple expensive high-

resolution photomasks must sequentially-aligned and exposed to incrementally build up layers of photoresist into the desired 3D structure.[119–121] Photolithography tends to be tedious, challenging, and expensive in terms of time, training, and resources, thus limiting final device quality and reproducibility.[122,123] Within this context, 3D-printing is emerging as a more preferable method for rapid prototyping of microfluidic device designs and concepts.[124–131] However, traditional additive manufacturing techniques, such as extrusion-based[132] or inkjet-based 3D-printing[127] suffer from such limitations as poor feature resolution, limited build volumes, and long runtimes. Particularly for tissue engineering LoC applications, microfluidic devices fabricated with these methods tend to leave their users with limited monolayer culture analysis or bulk gel studies.[133,134] Recently, simple 3D structures have been printed within a microfluidic device using extrusion-based manufacturing techniques using three bioinks.[131] However the user must seal the microfluidic device before use, preventing any changes to the printed geometry and requiring the user to fabricate new devices for future 3D applications. 3D-printed modular microfluidic devices[135] have also been designed, with the ability to pick and choose various applications, like mixing, however for tissue engineering applications, users will be limited to thermal gelation of bulk gels within the microfluidic device. To further extend on this new emerging field of 3D tissue engineering, there is large potential in incorporating 3D tissue constructs with defined architectures into a microfluidic device to not only minimize waste of costly resources, but also enable studies of cell behavior and metabolic output in real time under flow.

Therefore, we present the application of digital micromirror device (DMD)-based printing in the construction of a novel 3D-printer enabled Variable Height Micromixer (VHM). DMD-based printing utilizes an array of millions of individually-controllable micromirrors to project a 2D

image onto a moving plane of photopolymerizable prepolymer solution, thereby allowing production of 3D high-resolution microstructures.[136–139] An advanced technology, Micro-Continuous Optical Printing (μCOP) utilizes a DMD and dynamically projects different images as a stage moves a prepolymer solution vertically through the system's optical focal plane, rapidly creating complex 3D microstructures. [126,140–147] This grants the ability to rapidly prototype and iterate through master mold generations without the time and resource-intensive issues that plague other 3D-printing techniques. In this report, the VHM design incorporates rectangular columns of varying heights within zigzagging block-shaped fluidic elements that lead to an optically clear chamber for later *in situ* fabrication of structures. The mixing performance of this device was investigated experimentally with fluorescence microscopy for a range of volumetric flow rates ranging from 20 μL/min to 2.4 mL/min. Then, capitalizing on the μCOP system's ability to fabricate structures without physical contact, we demonstrate the ability to fabricate a complex 3D scaffold within an already-completed microfluidic device, using on-chip mixing of a live cell suspension with a prepolymer solution. In addition to its effective mixing capability, this device showcases the capacity to facilely construct complex 3D microfluidic devices that enable direct study of how factors such as fluid flow and microarchitecture can affect cell behavior.

2.3. Experimental

2.3.1. Prepolymer Solution Preparation

Polyethylene glycol diacrylate (PEGDA, MW~700), 2-Hydroxy-4-methoxy-benzophenon-5-sulfonic acid (HMBS), 2,2,6,6-tetramethylpiperidine 1-oxyl (TEMPO, free-radical quencher) were purchased from Sigma-Aldrich. Photoinitiator Irgacure 651 was purchased from Ciba Inc. To prepare the 100% PEGDA solution, 1% (wt/vol) Irgacure 651, 0.5%

(wt/vol) TEMPO free radical absorber, 0.5% (wt/vol) HMBS was added and sonicated for one hour. Gelatin methacrylate (GelMa) and lithium phenyl-2,4,6-trimethylbenzoylphosphinate (LAP) was synthesized as described previously.[148,149] The prepolymer solution was prepared by mixing 10% (w/v) GelMA with 0.2% (w/v) LAP in PBS at 37°C.

2.3.2. Device Design and Fabrication

Sectioned standard microscope slides (VWR) were cleaned and subsequently functionalized with 3-(Trimethoxysilyl)propyl methacrylate (TMPSA, Sigma) as previously described.[141] Predefined 500 μm PDMS spacers were used to separate a methacrylated slide from a sacrificial platform, and this space was then filled with the PEGDA-based prepolymer solution. The gestalt microfabrication process is depicted in schematic form in Figure 1.1. In our previous work, we have demonstrated the use of continuous optical-based 3D-printing to fabricate complex 3D structures with high aspect ratios in very short time scales.[150] The μCOP system (Figure 1a) is comprised of 1) a UV light source (Omnicure 2000), 2) a Digital Micromirror Device (DMD), 3) UV-grade projection optics (Edmunds Optics), a high precision computer controlled x-y-z stage (Newport 426/433 series), and a 4) CCD Camera. The wavelength used to fabricate the PEGDA mold was 365 nm with a total output intensity of 2.4 W/cm^2.

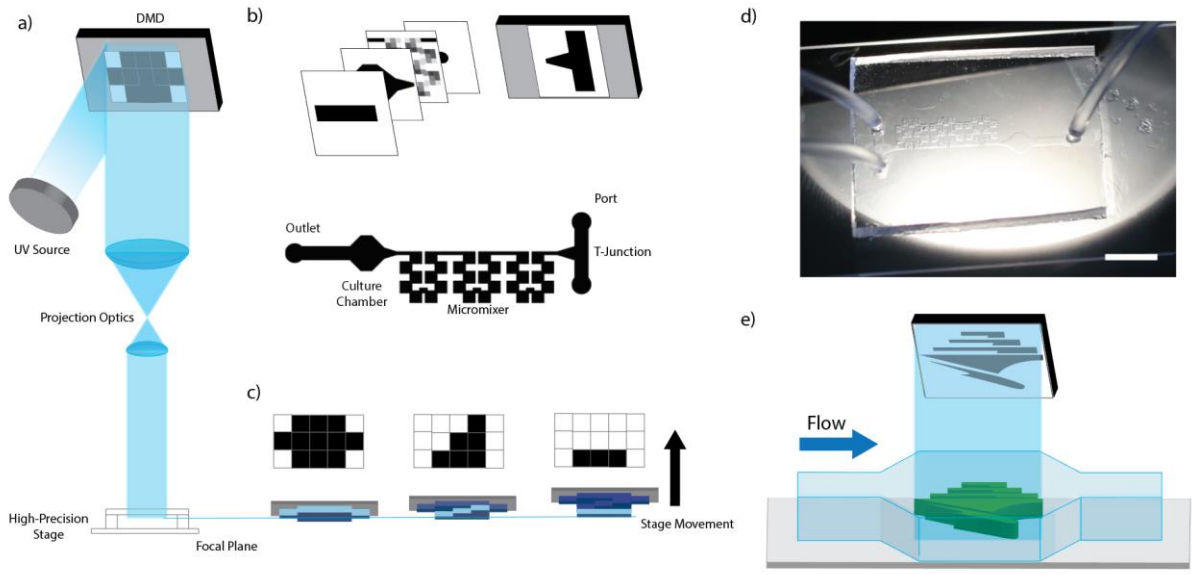

Figure 2.1: Schematic and process flow of Variable Height Mixer device fabrication.

a) Schematic of the μCOP system consisting of a UV source, DMD device to reflect user-specified patterns, projection optics to focus the light onto a prepolymer solution set on a high-precision stage. b) After producing a segment of the VHM device, the masks are changed and the device is stitched together using the xy-stage. c) Each segment is comprised of several virtual masks. The gray level determines the duration that the light is projected on a specific point, corresponding to taller structures. The light is modulated by changing masks corresponding to specified z-positions. d) Fabrication results of a VHM cast in PDMS, scale bar=5mm. Due to projection-based photopolymerization, the μCOP system allows for in-device printing e) of complex 3D structures when prepolymer solution is flowed in.

Virtual masks of the VHMs were designed using Adobe Photoshop with increasing exposure corresponding to darker shades of gray. The images were imported into MATLAB (Mathworks) and made into transverse z-slices. The series of masks are then fed continuously corresponding to their respective z-positions, spatially patterning and curing the prepolymer solution. The full device consists of grayscale images in segments Figure 1.1C: 1) Ports, 2) T-Junction, 3) micromixer unit, 4) culture chamber, and 5) an outlet. After each segment, the following segment's mask is aligned. The resulting polymerization of the five masks is a fully-featured, inverse-construct of our microfluidic device.

PDMS was then used in microcasting the PEGDA-based structural mold. PDMS is an attractive material for use in microfluidics due to its ease-of-use, material properties, and low costs, as demonstrated by its near ubiquity in microfluidic device fabrication. For the VHM, PDMS was created by using a 10:1 mixture of Sylgard 184 Silicone Elastomer and Sylgard 184 Curing Agent. Mixing of the PDMS was performed manually and then poured over the PEGDA molds to a controlled final thickness of 5 mm. In-solution bubbles from mixing were eliminated via vacuum at room temperature conditions for 1.5 hours. Curing of the PDMS casting of the PEGDA mold was done via convection oven at 100^{o}C for 1 hour.

Post curing, the PDMS cast was extracted from the PEGDA mold and cleaned of any residual debris. Porting of the device's inlets and outlets was performed with a 16G needle (Becton-Dickinson). The PDMS cast and its paired glass slide were cleaned with deionized water and isopropanol, then air-dried to remove residual water before undergoing RF-generated plasma cleaning in a Harrick Plasma PDC-002 plasma cleaner. The PDMS and glass were then bonded with firm manual pressing. Post plasma-bonding, the device was heated on a hotplate at 85°C for 8 minutes in order to finalize the bonding between the PDMS and glass. Once cooled, the device was visually inspected and underwent quality control checks for defects and/or leaks. An example device is presented in (Figure 1.1D)

2.3.3. Mixing Quantification

The device's mixing capability was evaluated by fluorescence imaging of on-chip mixing of a water-borne fluorescent dye. A Lucca Technologies GenieTouch^{TM} dual-channel syringe pump was used to drive two 20 mL syringes, connected to the micromixer via 0.02" ID Tygon tubing (Cole-Parmer) and 22 gauge blunt needles (Brico Medical). One 20 mL syringe contained a Fluorescein isothiocyanate (FITC)-Dextran fluorescent dye (Sigma, 20,000 MW) at 0.1 mg/mL

in deionized water (DI) water, and the other 20 mL syringe contained DI water. No discernible cross-reactivity or auto-fluorescence was observed between the two solutions and with the PDMS device.

The fluorescence intensity within the VHM was visualized under a Leica inverted fluorescence microscope. Baseline measurements of the fluorescence intensity at the inlet and outlet of the micromixer were taken with the device fully-infused with deionized water and the 0.1 mg/mL FITC-dextran dye solution. All subsequent measurements of mixing conditions were normalized with respect to baseline FITC-dextran dye infusement. Multiple volumetric flow rates were explored, starting from 10 μL/min and subsequently doubling until 1280 μL/min. At each flow rate, the device was allowed to stabilize to steady state before taking measurements. Twenty images over the course of one second were taken. Fluorescence intensity profiles were produced using ImageJ and averaged over time.

2.3.4. In-Device 3D Scaffold Printing

Variable Heigh Mixer (VHM) devices were primed with 70% ethanol and subsequently treated with TMPSA solution. Samples were rinsed with 5 mL of DI water to ensure clearing of the device of any residual TMPSA. A syringe of 10% GelMA (wt/vol), 0.2% FITC-Dextran (wt/vol), 0.4% LAP photoinitiator (wt/vol) in PBS and a second syringe of PBS was prepared. With the microfluidic micromixer deployed on the μCOP fabrication stage, the two solutions were injected at a volumetric flow rate of 640 μL/min each using the GenieTouch dual-channel syringe pump, for a total flow rate of 1280 μL/min. The solutions were injected for 30 seconds to allow the system to reach steady state, after which the syringe pump's flow was terminated, and the device outlet was clamped. The solution was allowed to settle for 15 seconds. To further

demonstrate the capability of μCOP samples were fabricated within the VHM originally produced from the same system (Figure 1.1E).

2.3.5. Cell Culture and In-Device Cell Encapsulation

C3H/10T1/2 murine mesenchymal progenitor cells were purchased from ATCC and cultured according to protocol provided by ATCC. 10T1/2 cells were cultured in Dulbecco's Modified Eagle Medium (DMEM, Gibco) supplemented with 10% fetal bovine serum, heat inactivated (Hyclone). Cells were maintained in a 37°C incubator with 5% CO_2. Before encapsulation, cells were treated with CellTracker^{TM} Green (ThermoFisher) per manufacturer's protocol. Prior to staining, cell culture media was aspirated and cells were washed using warm PBS. DMEM with CellTracker green (1:1000) in DMEM without serum was added to culture flasks and incubated at 37°C, 5% CO_2 for 30 minutes. Cells were harvested using 0.25% Trypsin/EDTA and counted using general protocol. Cells were centrifuged at 210 RCF to produce a cell pellet and re-suspended to a concentration of $5x10^6$ cells/mL in DMEM with 10% FBS and 1% penicillin-streptomycin. A 5 mL syringe was filled with the cell suspension and loaded on the GenieTouch dual syringe pump along with another 5 mL syringe filled with pre-warmed GelMA prepolymer solution. The prepolymer solution and cell suspension were both connected to each inlet of the VHM, the VHM was placed on the μCOP system and the solutions injected for 30 seconds to ensure steady state. The syringe pump flow was terminated, and the device outlet was clamped. The solution was allowed to settle for 30 seconds. Samples were exposed to patterned 365 nm light from the μCOP system within the fabrication chamber for 30 seconds and imaged with fluorescence microscopy.

2.4. Results and Discussion

2.4.1. Fabrication Result Analysis

Three microfluidic micromixer molds of increasing complexity (Figure 1.2A: 1x1-unit, 3x3-unit, 9x9-unit) were printed using the μCOP system. A set of 2D masks were created with 9 shades of gray, with the 1x1-unit requiring only one shade. For the 9x9-unit device, 9 shades are repeated 9 times, appearing once every ⅓ segment of the single unit. The micromixer segment of the microfluidic device was comprised of 48 masks. To ensure proper polymerization of the entire structure, a set of eight base layers was required to initialize polymerization for the entire structure. Each subsequent darker shade of gray was exposed for four more layers than the preceding lighter shade, arriving at a total of 48 masks. The exposure time per layer was determined empirically to be 0.3 seconds to ensure that the fluid path fully formed with varied heights. Utilizing the xyz stage, the total microfluidic device was stitched from 9 exposures, three ports, a T-junction, three micromixers, the culture chamber, and an outlet. The total time to produce a single VHM mold was less than 5 minutes.

The PEGDA-based prepolymer solution, once fully cured, proved to be a useful prototyping medium for PDMS microcasting of our microfluidic device. 100% PEGDA's mechanical stiffness[138] proved sufficient to survive the rigors of PDMS microcasting at elevated temperatures while accurately preserving critical device features. The final casting of the 1x1-unit, 3x3-unit, and 9x9-unit PDMS molds can be observed in stereo microscope and scanning electron microscopy (SEM) images of the PDMS castings of the VHM molds (Figure 1.2B, C).

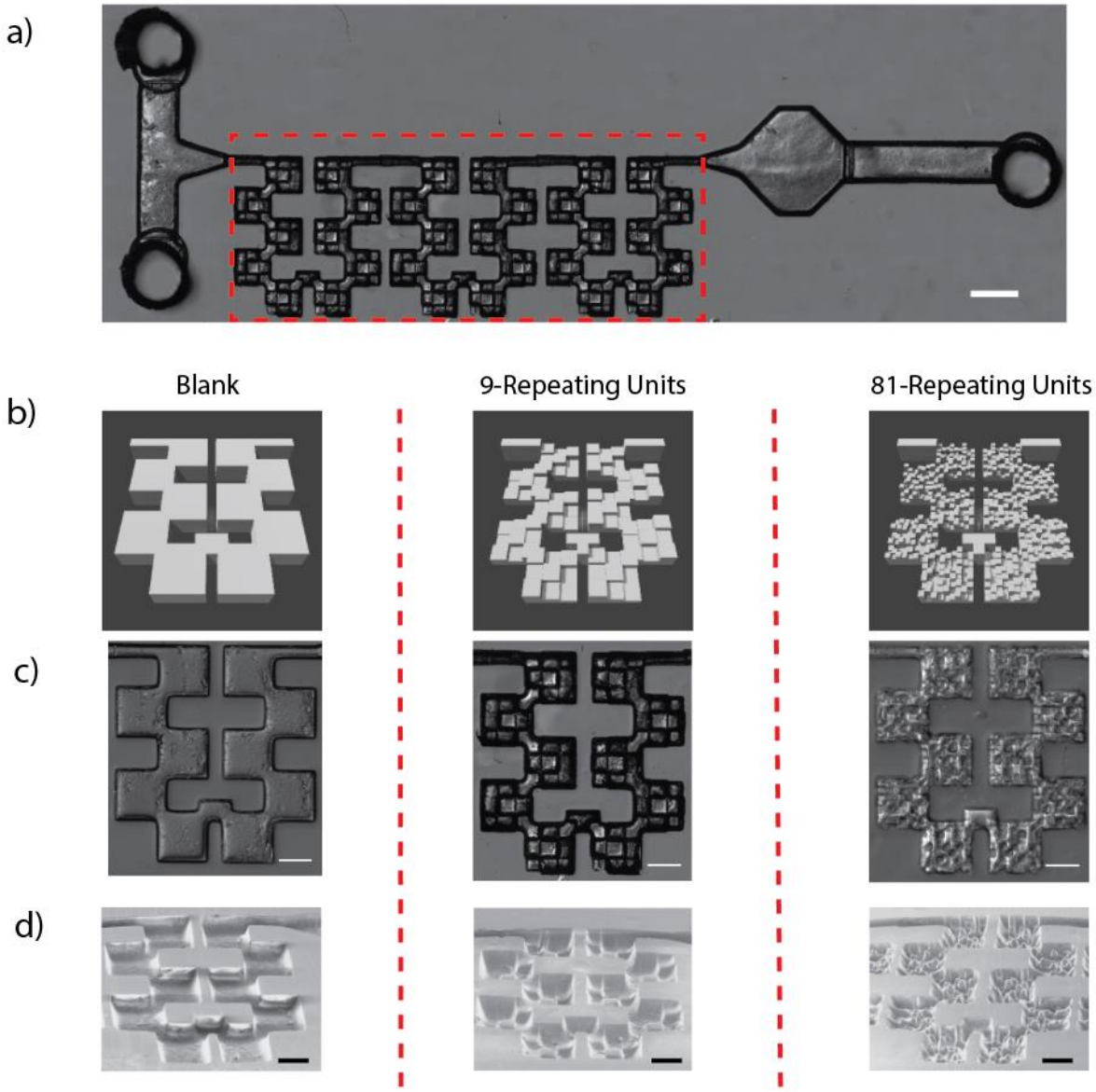

Figure 2.2: Varying VHM complexity.

Schematic of μCOP-enabled VHM device. a) DIC images of a full VHM device (scale bar = 1 mm). From left to right, blank, 9-repeating unit, and 81-repeating unit micromixer are shown, b) Solid models, c) DIC images (scale bar = 500 μm), d) and SEM micrographs pitched at a 45 angle (scale bar = 500 μm).

2.4.2. Structural Design and Simulation Analysis

As a passive micromixer tends to have no moving parts beyond its fluidic driver, mixing must be accomplished by means of interfacing fluid streams with the device's geometry in such a way to enhance diffusion and/or create chaotic advection. In planar micromixers, the designer is

by definition restricted to two dimensions, but operating in 3D allows for more variation within the same physical footprint. Here, we propose a Variable Height Micromixer (VHM) that combines a T-junction with repeating zigzagging chains of block-like elements dubbed 'macro-squares,' with each macro-square spatially patterned with grids of rectangular columns that range from 100 μm to 400 μm in height (Figure 1.1). With a maximum device height of 500 μm, any given particle in the device is forced to not only navigate in 2D, but over and around obstacles of varying heights. These rectangular columns obstruct flow within the VHM, causing fluidic tumbling and chaotic advection that enhances mixing of fluids before their arrival in an octagonal fabrication chamber, where additional structures may then be constructed via μCOP.

Three VHM variations were numerically simulated using finite element method analysis. First, a control structure (designated '1x1-unit') was designed to emulate a planar micromixer set at a constant 500 μm in height throughout the device. The next iteration (designated '3x3-unit') introduced a 3x3 grid of 300x300 μm square columns of varying heights into every macro-square as described. The last level of complexity (designated '9x9-unit') was for each macro-square to have a 9x9 grid of 100x100 μm variable-height square columns, effectively a 3-fold increase in fluidic perturbation. These three variations were virtualized in 3D with the aid of computer modeling program AutoCAD (Figure 1.SI1), and mixing was simulated using the Microfluidics Module of commercial finite element software (COMSOL Multiphysics). First, the solutions for single-phase, incompressible laminar flow was applied throughout the entire geometry of each of the three VHM models for a variety of wide variety of flow rates, with no-slip conditions at the sidewalls and the outlet pressure (*p)* set to zero. Second, the concentration profile of the simulated fluorescent dye was solved for using the previously-solved laminar flow solution. Additional assumptions include: 1) concentration of the simulated fluorescent dye did not affect

dynamic viscosity and density of the water carrier fluid, 2) wall surface tension, gravitational forces, and body forces were considered negligible. Free tetrahedral meshes optimized for fluid dynamics were chosen for the VHMs, with the number of mesh elements ranging from approximately 146K domain elements for the 1x1-unit model, to 1.2M domain elements for the 9x9-unit model.

In characterizing the VHM, consideration must be given to the device's Reynolds number and Peclet number and how they change throughout the device due to the 3D nature of the device. They are governed by the equations:

$$Re = \frac{\rho v D_H}{\mu} \quad (1)$$

$$Pe = \frac{v D_H}{D} \quad (2)$$

where ρ is fluid density, v is linear flow rate, D_H is the characteristic dimension, μ is fluid dynamic viscosity, and D is the mass diffusion coefficient of the solute species. In rectangular-shaped microchannels, the characteristic dimension is equivalent to the hydraulic diameter, which is given by the equation:

$$D_H = \frac{4A}{P} \quad (3)$$

where A is the cross-sectional area of the flow region, and P is the wetted perimeter, which is the perimeter of the cross-sectional area in contact with the aqueous medium.

From the model's geometry, the largest possible flow region barring the main fabrication chamber is the inlet region just before the tapered entry into the micromixing region, where the cross-sectional area is 5.00×10^{-7} m^2 and its corresponding D_H is 6.67×10^{-10} m. The smallest possible flow region among the VHMs can be found in select chokepoints of the 3x3-unit VHM, such as the overlapping area between the 6th and 7th macro-square (amounting to approximately

a 5% overlap in linear footprint). The cross-sectional area for this region is 3.77×10^{-8} m^2, with a corresponding D_H of 1.81×10^{-4} m. We empirically determined that a total input volumetric flow rate of 1280 μL/min as the minimum rate at which effective mixing occurs. In Table 1, the local Reynolds numbers and Peclet numbers for the largest and smallest flow regions can be approximated based on model-derived estimates of maximum linear flow velocities at those regions (ESI Movie SI1, SI3, SI5).

VHM Type	Q [μL/min]	Re_{Inlet}	$Re_{Chokepoint}$	Pe_{Inlet}	$Pe_{Chokepoint}$
1x1-unit	1280	3.20×10^{-5}	1.37×10^{2}	0.339	1.45×10^{6}
3x3-unit			1.65×10^{2}		1.75×10^{6}
9x9-unit			2.34×10^{2}		2.48×10^{6}

Table 2.1: Approximations of local Reynolds and Peclet numbers for each VHM, at their largest and smallest flow regions.

The pressure drop experienced by laminar fluid flow in rectangular microchannels is governed by the Hagen-Poiseuille equation:

$$P = \frac{12L\mu Q}{WH^3} \quad (4)$$

where Q is the volumetric flow rate, μ is fluid dynamic viscosity, and L, W, and H correspond to the length, width, and height of the microchannel. Due to the way the VHMs have abrupt changes in width and/or height over the course of the device, pressure drops for each device's mixing regions were determined analytically. At an input volumetric flow rate of 1280 μL/min, the pressure drop across the 1x1-unit, 3x3-unit, and 9x9-unit VHMs from the inlets to the outlet of the 30^{th} macro-square were approximated to be 631 Pa, 3.48×10^3 Pa, and 5.13×10^3, respectively (ESI Figure 1.SI2).

2.4.3. Mixing Analysis

In order to determine how well the VHM can homogeneously mix different solution streams, DI water and a solution of 0.1 mg/mL FITC-Dextran were introduced via a T-junction at various flow rates. To better understand the effects of the VHM's on mixing of disparate fluids, fluorescent images were taken across the entire device and stitched into a gestalt image (Figure 1.3A).

Across all three VHM variations, the collected data show that the two streams flow into the VHM and remain visually-distinct from each other while in the T-junction flow region. Mixing was negligible across all tested flow rates in this initial zone, likely due to the low residence time in the T-junction where only molecular diffusion dominates. Only once the combined fluid streams reached the zigzagging macro-squares did we begin to see the first signs of mixing. In the case of the 1x1-unit VHM, visually there is distinct separation between the two fluids until an input flow rate of 640 μL/min, where multiple slipstreams of DI and fluorescent dye begin to manifest. At an input flow rate of 640 μL/min (Figure 1.3A), chaotic vortices begin to make their first appearances at the second macro-square, however a formation of slipstreams of DI and fluorescent dye are prevalent. It is not until 2,400 μL/min does the 1x1-unit device achieve proper mixing prior to the outlet.

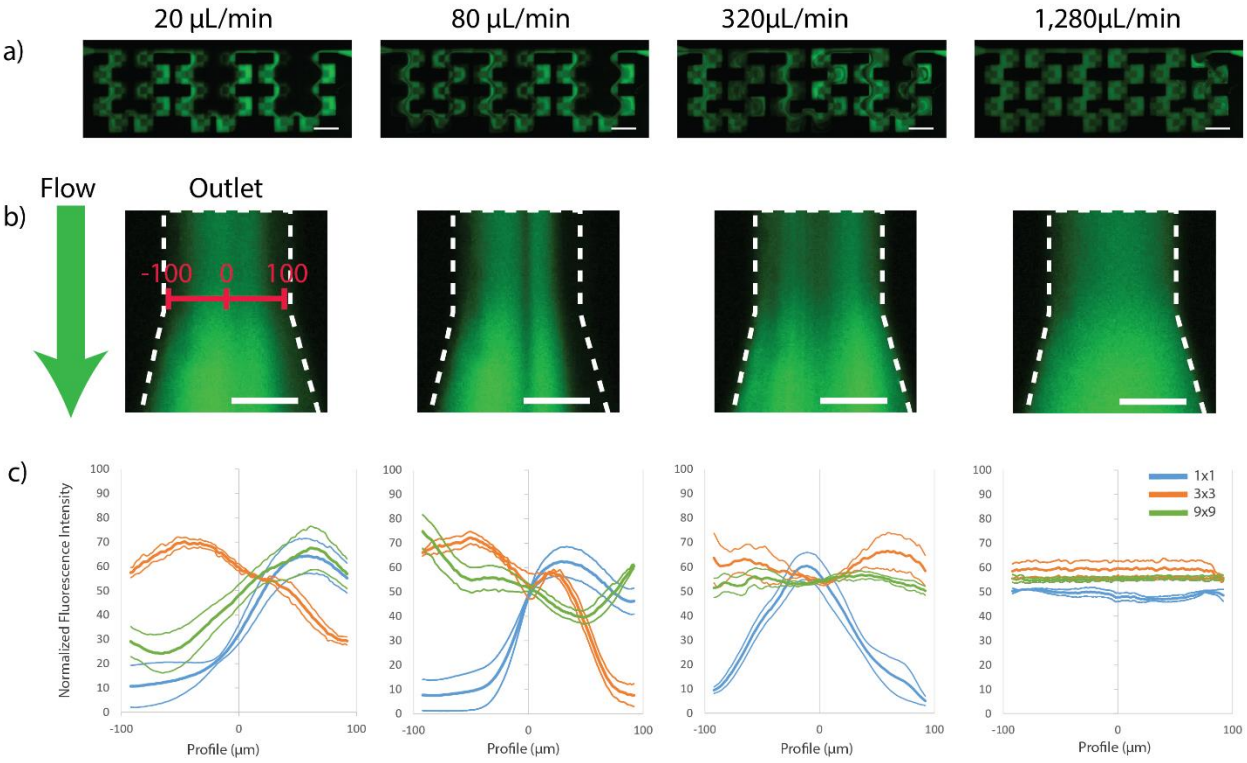

Figure 2.3: Mixing behavior of VHMs as a function of surface complexity vs. flow rate.

Mixing behavior of VHM devices. a) fluorescent images of a 3x3-unit VHM device across the total length of the zigzag micromixer (scale bar = 1 mm). b) fluorescent images of the outlet of a 3x3-unit VHM at 40, 160, 640, and 2.4 ml/min (scale bar = 100 µm) where the c) intensity profiles were analyzed (blue = 1x1-unit, orange = 3x3-unit, green = 81x1x1-unit, n = 3)

The 3x3-unit VHM improved superior mixing behavior compared to the 1x1-unit VHM; with numerous multi-lamellar streamlines forming by 160 µL/min, and significant chaotic advection behavior by 320 µL/min. By 640 µL/min, the fluid streams have mixed near 100% completeness at the outlet (30th macro-square). At 1,200 µL/min and 2,400 µL/min full mixing occurred by the 14th and 7th macro-square, respectively. The 9x9-unit VHM exhibits better advective mixing capability compared to the 3x3-unit VHM, with multi-lamellar streamlines forming by 80 µL/min, and significant chaotic advection behavior by 320 µL/min. At 640 µL/min, by the 24th macro-square, the fluid streams have mixed to 100% completeness. At 1,280 µL/min and 2,400 µL/min, full mixing occurred by the 12th and 10th macro-squares,

respectively. The experimentally-recorded concentration patterns of the VHMs agree well with the simulated data (ESI Figure 1.SI3-SI4, Movie 1.SI2, 1.SI4, 1.SI6).

However, as we shift from the 1x1-unit to the 9x9-unit VHM, the decrease in feature size actually increases the variability of the fluidic path, thus increasing the variability in fluorescence intensity. This makes it difficult to accurately determine the level of mixing, thus higher magnification images were taken using a 10x object at the inlet and outlets of the three VHMs. An intensity profile was determined by drawing a line perpendicular to the flow direction across the outlet using ImageJ. 20 images were taken over 1 second, at 5 ms exposures were averaged at each pixel across the profile. Fluorescence profiles across the outlets of three samples of each VHM geometry, 1x1 (blue), 3x3 (orange), and 9x9 (green), were taken (Figure 1.3C). At 20 μL/min and 40 μL/min (Figure 1.3C), we observe laminar flow with minimal streamline formation and lamellation. At 80 μL/min input flow rate, we begin to see the 9x9-unit exhibit the formation local eddies and displaced streamlines, whereas the 3x3-unit and 1x1-unit VHMs do not. At 160 μL/min, the 9x9-unit continues to form larger vortices and increasingly more lamellation of fluorescent streamlines, whereas the 3x3-unit and 1x1-unit only just begin to shift their streamlines toward the midline of flow (Figure 1.3C). At 320 μL/min, the 3x3-unit and 9x9-unit VHMs fluorescent lamellations begin to merge into homogeneity, whereas the 1x1-unit still exhibits a focusing of fluorescent streamlines toward the middle of the device, suggesting that the variable height geometries of the 3x3-unit and 9x9-unit VHMs are generating increased instances of mixing throughout the fluid path. By 1,280 μL/min, the fluorescence profiles of the 3x3 and 9x9 stabilize into complete homogeneity, whereas the 1x1-unit still exhibited the incompletely-mixed multi-lamellar behavior that the 3x3-unit and 9x9-units had long since surpassed (Figure 1.3C). Finally, at the final flow rate of 2,400 μL/min, all three devices were

fully mixed, indicating that even the 1x1-unit's smooth features were able to induce mixing by virtue of its zigzagging geometry. After empirically determining that both the 3x3-unit and 9x9-unit VHMs induced proper mixing by 1,280 μL/min, we opted to utilize the 3x3-unit VHM at this flow rate for the demonstration of 3D-printing a cell-laden construct within a VHM.

2.4.4. In-Device Spatial Patterning and Cell Encapsulation

To further the capabilities of the μCOP system beyond producing a mixing device, the ability to fabricate complex structures within the culturing chamber was explored. Pre-warmed syringes of 10% GelMA, 0.2% FITC-dextran, and 0.4% LAP and PBS was injected into the VHM at 640 μL/min, or a total flow rate of 1,280 μL/min (Figure 1.4A). After 30 seconds of flow, the outlet was clamped and the device was allowed to rest for 15 seconds. Images captured during the exposure of the prepolymer solution for 30 seconds indicated successful printing within the VHM (Figure 1.4B; ESI Movie 1.S1). The FITC-dextran/GelMA structure was imaged under fluorescence microscopy, which exhibited a faithful rendering of the 2D mask. Samples were cleaned using 0.25% trypsin/EDTA, filling the VHM, incubating samples for 5 minutes at 37°C and were rinsed with DI water. Samples were retreated with TMPSA solution for 30 minutes and printed in again, demonstrating the ability to reuse the VHM as necessary.

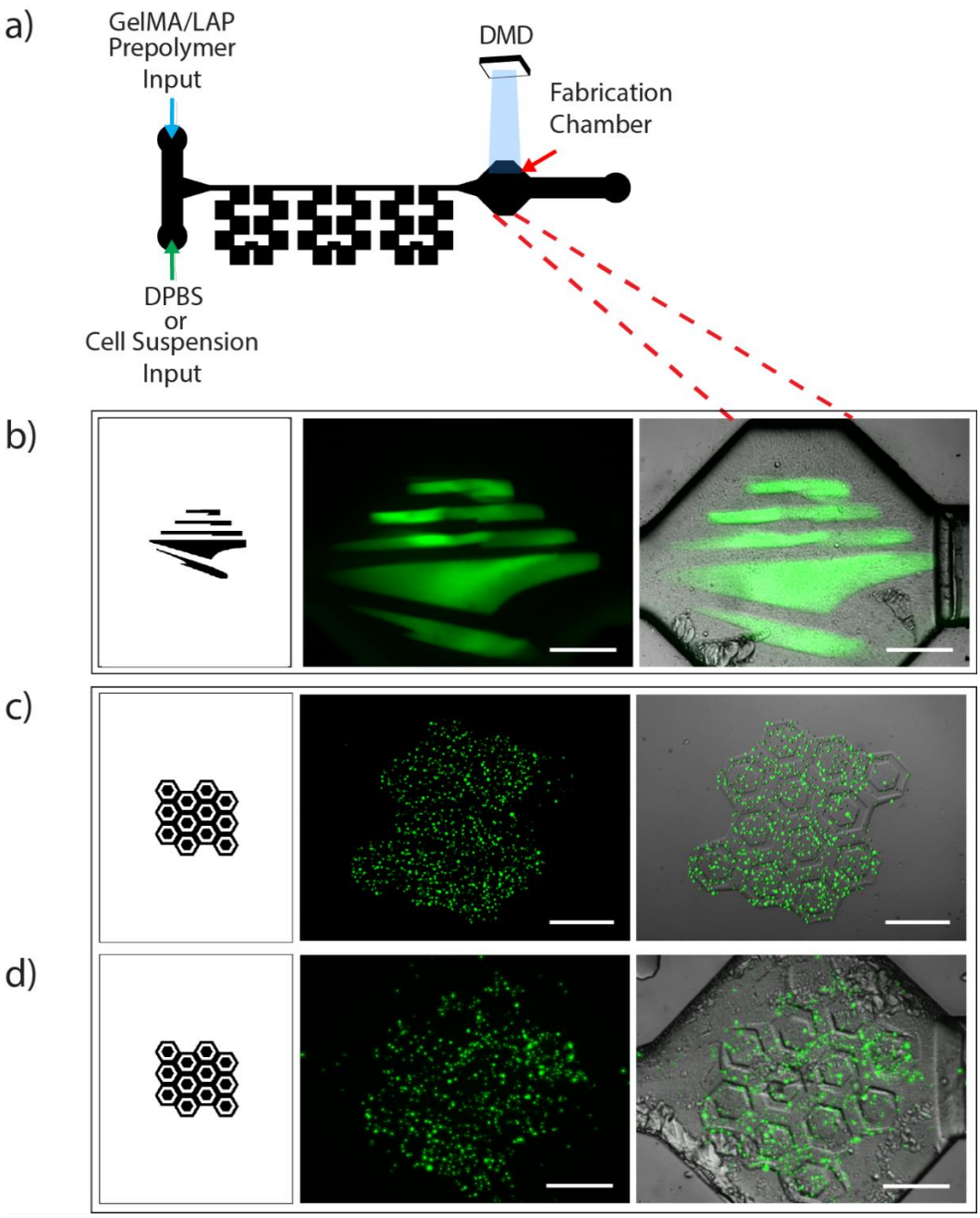

Figure 2.4: Fabrication of 3D scaffold shapes and cell-laden hydrogels inside VHMs.

a) A schematic of the VHM device with the 10% GelMA, 0.4% LAP prepolymer solution connected to one inlet and DPBS or a 10T1/2 cell suspension connected to the other. The solutions were injected through the VHM at a total flow rate of 1280 µL/min to induce mixing. The mixed prepolymer solution was subjected to a digital mask reflecting 365 nm light. b) A fluorescent (left) and composite image (right) of the UCSD logo 3D printed within the VHM fabrication chamber. c) Fluorescent and composite images of a biomimetic hepatic lobule structure was printed with premixed CellTracker green cells and prepolymer solution (1:1) compared to d) 10T1/2 cells mixed against the prepolymer solution within the VHM device. Scale bar = 1 mm.

Whereas several 3D-printing technologies, including stereolithography[123] and extrusion-based[128,131,151] have produced functional microfluidic devices for 2D and 3D culture[133] and mixing,[115] these devices do not allow for post-fabrication design of simple or complex architecture. That is, the design of the microfluidic device will also dictate and limit the scope of studies that can be performed *in situ*. The μCOP system as used in this report enables users to print complex 3D geometries within a completed microfluidic device, potentially allowing for further studies in how cell interaction with materials are affected by flow. The VHM system along with *in situ* polymerization of prepolymer solutions can be extended to study cell interactions with gradients of materials, localized changes in stiffness by controlling exposure time, or the introduction of multiple materials.

Ultimately, the purpose of the VHM was designed to limit the amount of time the cells were exposed to the prepolymer solution prior to cell encapsulation. A 5 mL syringe of 10T1/2 cell suspension ($5x10^6$ cells/ml), treated with CellTracker green and a 5 mL syringe of 10% GelMA, 0.4% LAP solution placed on the syringe pump and was injected into the VHM at 640 μL/min, or a total flow rate of 1,280 μL/min (Figure 1.4A). The mixed cell suspension/prepolymer solution within the fabrication chamber was subjected to an exposure of 365nm light from a digital mask comprised of hexagons for 30 seconds. 10T1/2 cells were successfully encapsulated *in situ* within a spatially patterned hexagonal pattern in the GelMA construct and excess cells and prepolymer solution were gently flushed with DMEM with 10% FBS before imaging at 10 μL/min from the outlet for 5 minutes. Cells premixed 1:1 within a 1.5 mL centrifuge tube and polymerized on a methacrylated slide (Figure 1.4c) were compared with a cell/prepolymer solution mixed using the VHM (Figure 1.4D). Pattern fidelity was maintained and cells were successfully encapsulated utilizing the μCOP system in constructs printed using

manual mixing and VHM mixing methods. The presence of cell aggregates in the VHM mixed samples may indicate a gentler mixing. Upstream agitation of the syringes was not employed prior to mixing through the VHM and may be necessary for future cell studies utilizing this method, especially with higher cell concentration suspensions. Cell viability studies, along with long-term culture under fluidic conditions are reserved for future studies. By demonstrating the ability to both produce a complex VHM device and to spatially pattern cells in complex geometries post-fabrication within the device, *the* μCOP system can be a useful platform to produce cost-effective microfluidic devices that can serve multiple purposes and to study the effects of fluid flow on complex 3D-Printed tissues.

2.5. Conclusions

In this report, we describe the ability to efficiently mix two fluids within a microfluidic device such that a tissue scaffold can be printed *in situ* within the device. The variable-height features within each of the 3x3-unit and 9x-9-unit VHMs induced better mixing capability when compared to the 1x1-unit VHM. The experimental data for each of the VHMs show good agreement with the simulated results for our tested range of flow rates, with a Reynolds number range of 3.2E-05 < Re < 234 across the slowest and fasted regions of the VHMs, respectively. The pressure drop range was 631 Pa < ΔP < 5,130Pa for the 1x1-unit and 9x9-unit VHMs, respectively. A dual-channel syringe pump was used to drive the 10T1/2 cell suspension and GelMA prepolymer solution into the device, where hierarchically patterned features induced passive mixing of the two substances such that a three-dimensional, cell-encapsulating tissue scaffold could be fabricated out of the mixed solutions. We believe that low-flow rate microfluidic mixers of this type can be used in a wide variety of applications where in-device mixing of reagents is preferable to pre-mixing external to the device, such as in 3D-printing,

where mixing live cells with prepolymer solutions may be deleterious. Longer term goals involve optimizing the micromixer design for improved mixing efficacy, and tailoring the concept for application-specific needs that require micromixing and *in situ* 3D-printing. The ability to print 3D architectures within a microfluidic chamber, along with the ability to spatially pattern cells greatly extends the capabilities and future direction of microfluidic device design.

2.6. Acknowledgements

This project received support from the Department of Defense (W81XWH-14-1-0522), California Institute for Regenerative Medicine (RT3-07899) and National Science Foundation (CMMI-1332681 and CMMI-1547005). We also acknowledge the UCSD Neuroscience Microscopy Shared Facility grant P30 NS047101 for use of confocal imaging and give thanks to the Darren Lipomi Lab for allowing the use of their plasma cleaning system.

Chapter 2, in full, includes a reprint of the published article, "Direct 3D-Printing of Cell-Laden Constructs in Microfluidic Architectures." Liu, Justin; Hwang, Henry H.; Wang, Pengrui; Whang, Grace; Chen, Shaochen. Lab on a Chip, 2016. The dissertation author was a co-primary investigator and a co-author of this work.

2.7. Electronic Supplementary Material (ESI)

Scanning Electron Microscopy Preparation

To obtain a high-resolution scanning electron microscopy (SEM) image of the microfluidic structure, the sample surfaces were first coated by a thin layer of iridium by Emitech K575X Sputter Coater prior to imaging. The SEM images were obtained by using Philips XL30 ESEM with electron beam of 3.0 kV.

3D Models of Variable Height Micromixers (VHMs)

The three variations of the VHMs (1x1-unit, 3x3-unit, and 9x9-unit) were created in a computer-aided design software (AutoCAD), and converted into .STL format readable by finite-element method analysis software (COMSOL):

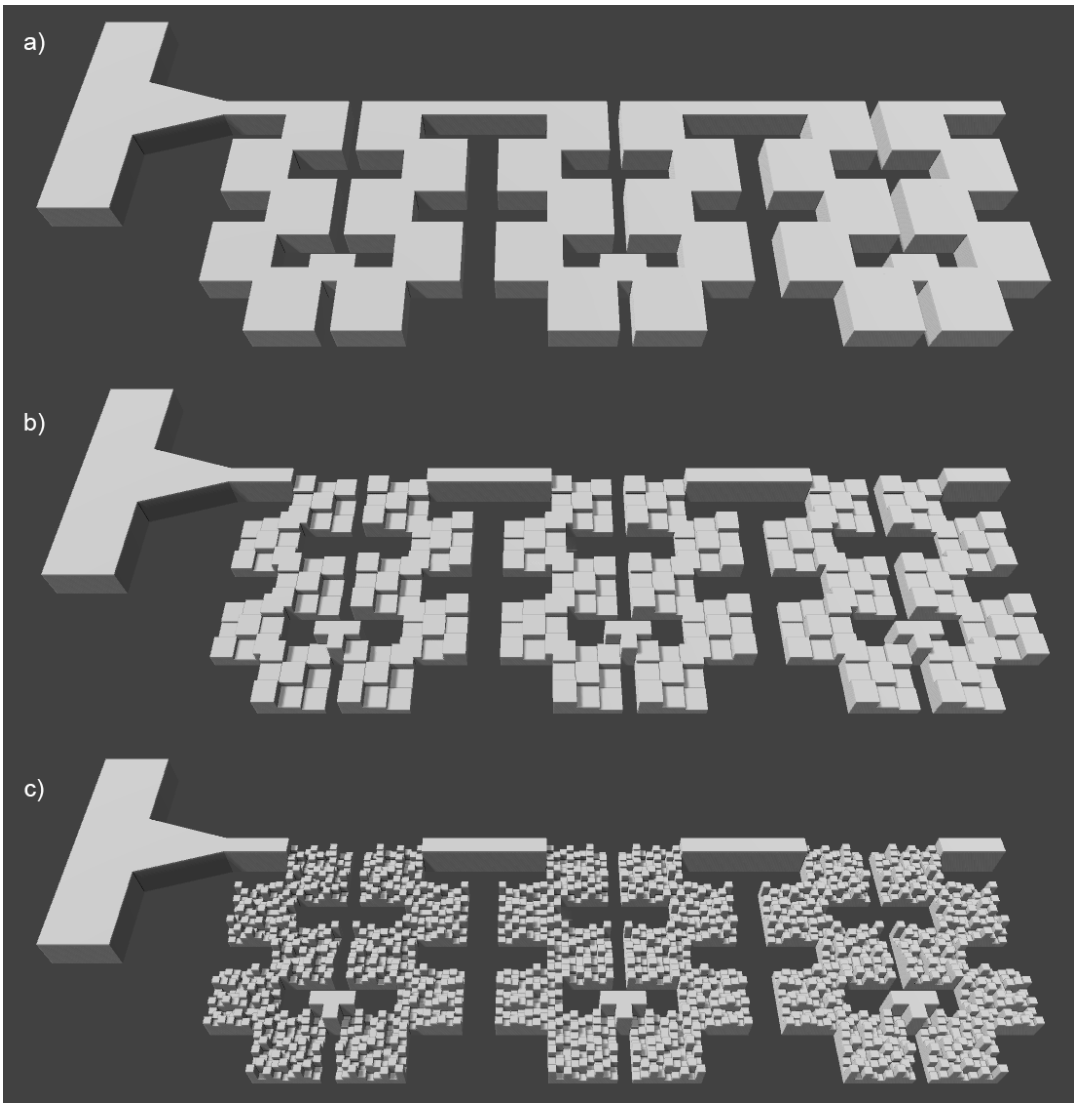

Figure 2.5: ESI Figure SI1: Computer-generated model of VHM micromixing regions. a) 1x1-unit VHM, b) 3x3-unit VHM, and c) 9x9-unit VHM.

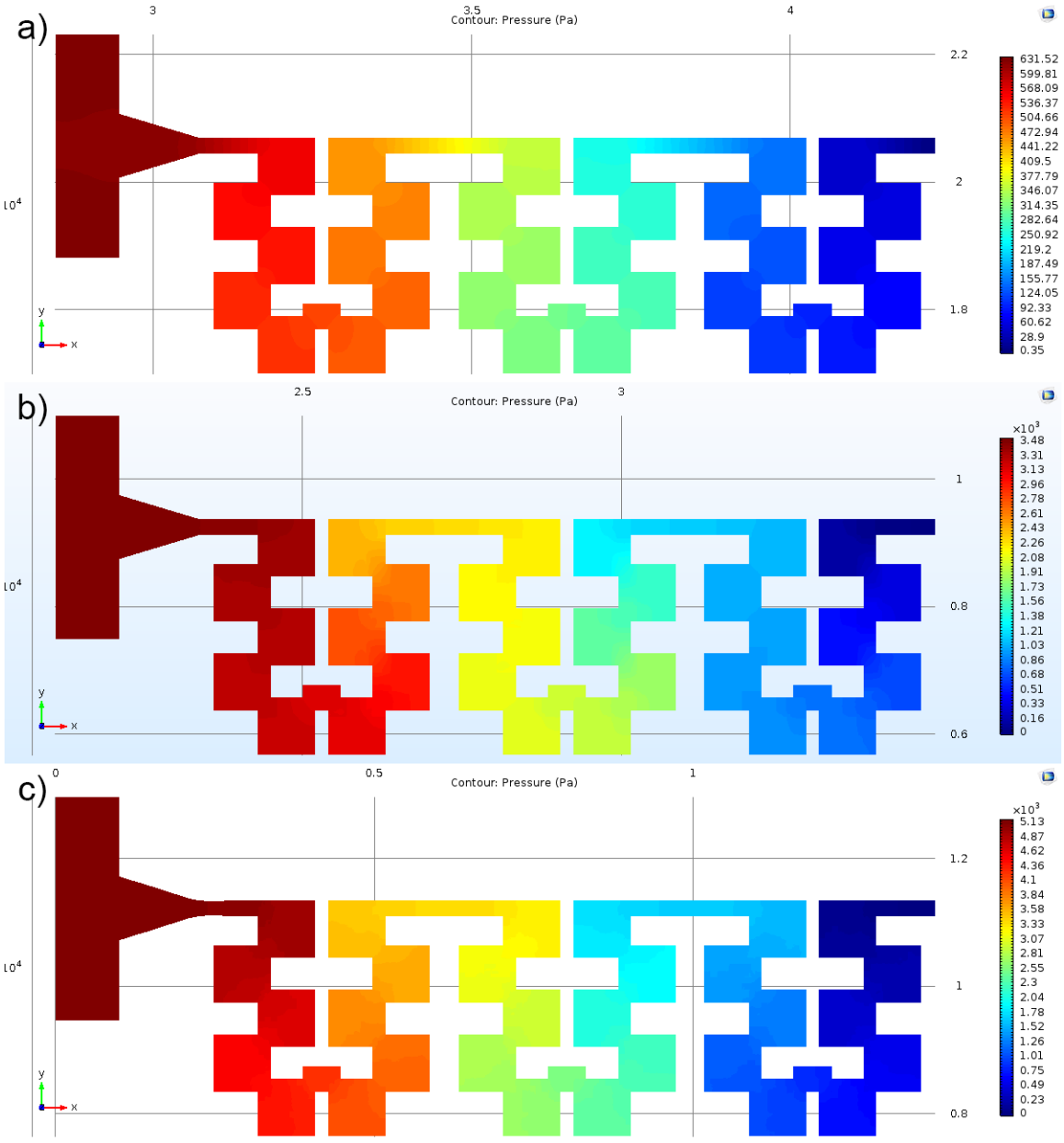

Figure 2.6: ESI Figure SI2: Theoretical pressure drop across VHM micromixing regions. a) 1x1-unit VHM, b) 3x3-unit VHM, and c) 9x9-unit VHM.

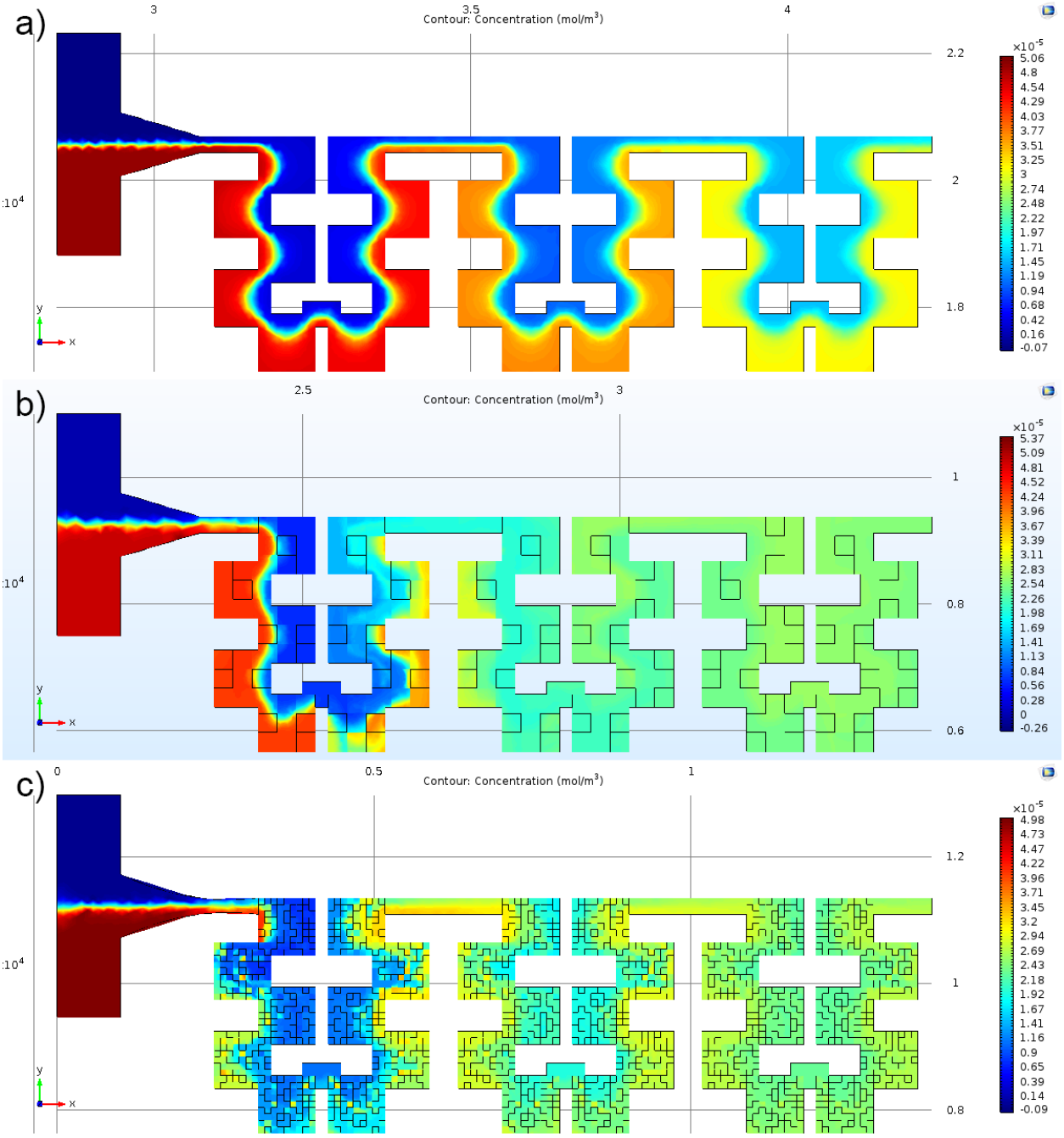

Figure 2.7: ESI Figure SI3: Theoretical concentration map across VHM micromixing regions.

a) 1x1-unit VHM, b) 3x3-unit VHM, and c) 9x9-unit VHM.

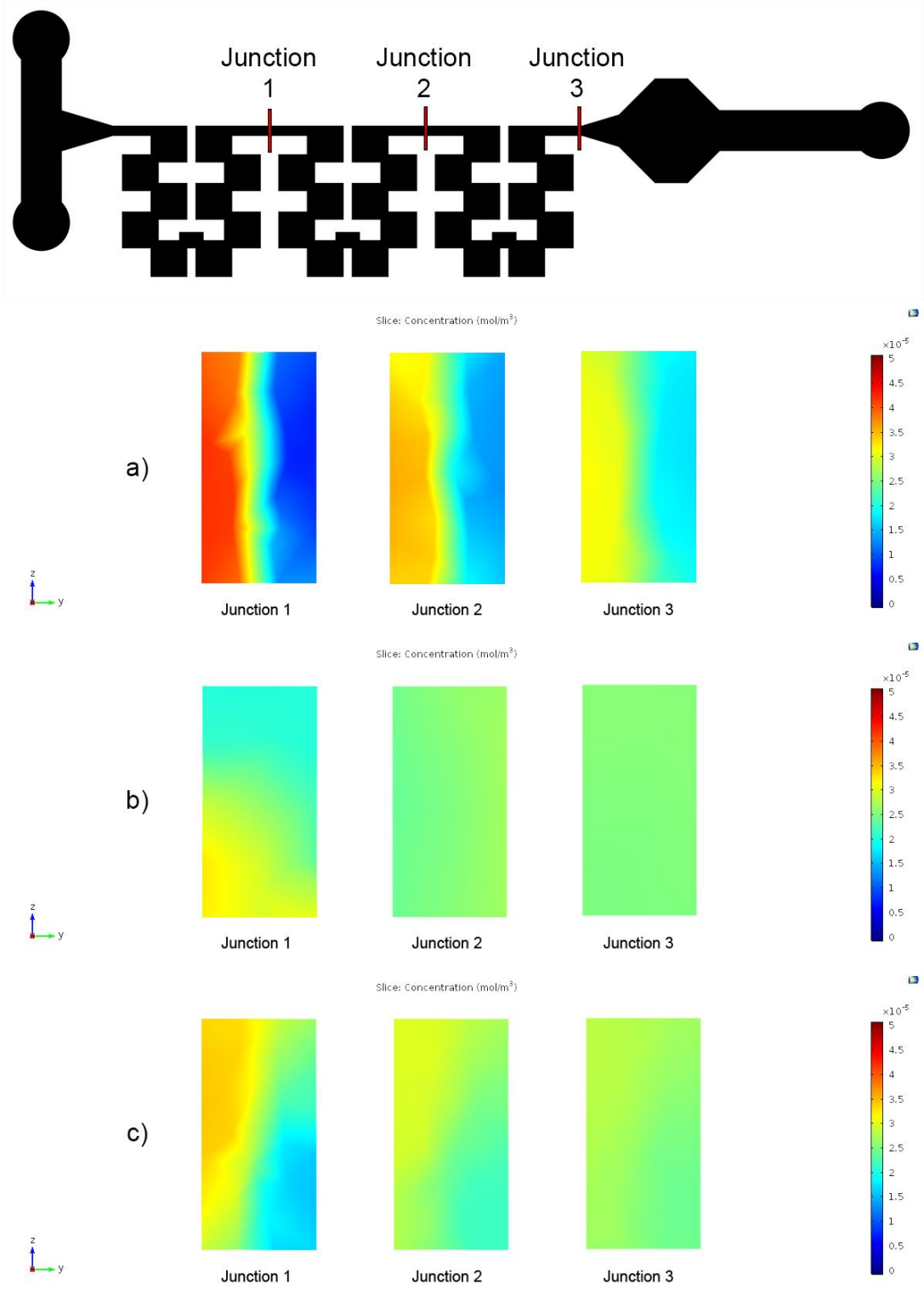

Figure 2.8: ESI Figure SI4: Theoretical cross-sectional concentration maps of VHM junctions.

a) 1x1-unit VHM, b) 3x3-unit VHM, and c) 9x9-unit VHM.

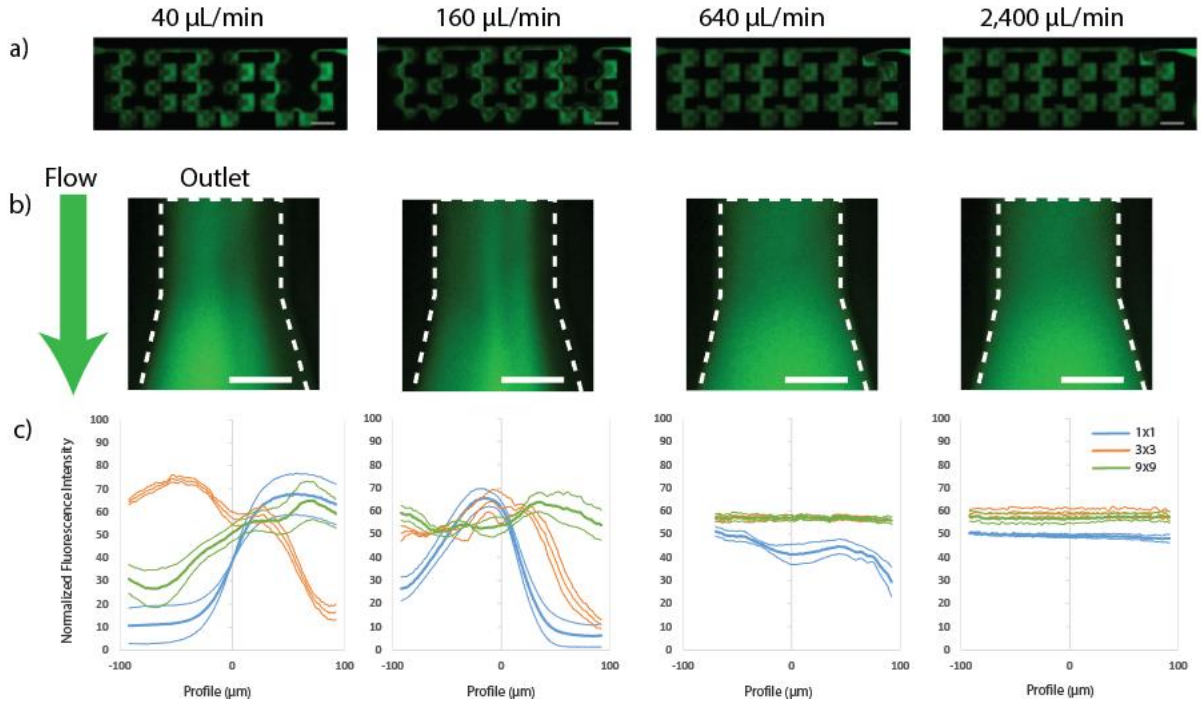

Figure 2.9: ESI Figure SI5: Mixing behavior of 3x3-unit type VHM device.

a) Fluorescent images of a 3x3-unit VHM device across the total length of the zigzag micromixer (scale bar = 1 mm). b) Fluorescent images of the outlet of a 3x3-unit VHM at 40, 160, 640 and 2.4 mL/min (scale bar = 100 um) where the c) intensity profiles were analyzed (blue = 1x1-unit, orange = 3x3-unit, green = 9x9-unit, error bars = SEM, n = 3).

Electronic Supplementary Information (ESI) Movies:
Supplementary movies are available as separate video files.

Movie 2.1: ESI Movie SI1: Theoretical simulation results (velocity) for the 1x1 VHM.
Cross-section views of velocity profile at 1,280 µL/min.

Movie 2.2: ESI Movie SI2: Theoretical simulation results (concentration) for the 1x1 VHM.
Cross-section views of concentration profile at 1,280 µL/min.

Movie 2.3: ESI Movie SI3: Theoretical simulation results (velocity) for the 3x3 VHM.
Cross-section views of velocity profile at 1,280 µL/min.

Movie 2.4: ESI Movie SI4: Theoretical simulation results (concentration) for the 3x3 VHM.
Cross-section views of concentration profile at 1,280 µL/min.

Movie 2.5: ESI Movie SI5: Theoretical simulation results (velocity) for the 9x9 VHM.
Cross-section views of velocity profile at 1,280 µL/min.

Movie 2.6: ESI Movie SI6: Theoretical simulation results (concentration) for the 9x9 VHM.
Cross-section views of concentration profile at 1,280 µL/min.

Movie 2.7: ESI Movie SI7: In-device fabrication.
Video captured with a UV filter over 50 seconds. Prepolymer solution is flowed in from the two inlet ports and mixed through the VHM. The syringe pump is stopped and the outlet is clamped. The masks are loaded and the UV exposure begins and lasts for 30 seconds. The resultant structure is visualized after the mask is removed.

CHAPTER 3: HIGH THROUGHPUT DIRECT 3D BIOPRINTING IN MULTIWELL PLATES

3.1. Abstract

Advances in three dimensional (3D) bioprinting have enabled the fabrication of sophisticated 3D tissue scaffolds for biological and medical applications, where high speed, high throughput production in well plates is a critical need. Here, we present an integrated 3D bioprinting platform based on microscale continuous optical printing, capable of high throughput *in situ* rapid fabrication of complex 3D biomedical samples in multiwell plate formats for subsequent culture and analysis. Our high throughput 3D bioprinter (HT-3DP) was used to showcase constructs of varying spatial geometries of biomimetic significance, tunable mechanical properties, as well as reproducibility. Live hepatocellular carcinoma 3D tissue scaffolds were fabricated *in situ* in multiwell plates, after which a functional drug response assay against the chemotherapy drug doxorubicin was performed. Dual cell-type populations involving both live hepatocellular carcinoma as well as human umbilical vein endothelial cells were also printed to demonstrate dual-tissue fabrication capability. This work demonstrates a significant advancement in that the production rate of 3D bioprinted tissue scaffolds with controllable spatial architectures and mechanical properties can now be done on a high throughput scale, enabling rapid generation of *in vitro* 3D tissue models within conventional multiwell cell culture plates for high throughput preclinical drug screening and disease modeling.

3.2. Introduction

Pharmacological research and development is currently a tedious and failure-prone endeavor, with an approved product taking potentially up to 12-15 years[152] and upwards of $2.6 billion USD in development costs[153] before making it to market. The failure modes often involve

the transition between validation phases of the development pipeline, e.g. hits generated from *in vitro* screenings failing in pre-clinical animal models[154], or the few successful hits in animal models failing to successfully translate to humans during clinical testing[155]. In this context there is significant interest in using human-origin *in vitro* models, specifically three-dimensional (3D) engineered tissue constructs, whose efficacy and potential to approach the complexity of human *in vivo* systems outstrips that of traditional 2D monolayer cell culture systems[156–160]. While advances in three-dimensional (3D) bioprinting have enabled precise fabrication of engineered tissue scaffolds of varying complexity, low throughput and low reproducibility can limit these technologies' use in applications where large quantities of consistent, functional samples are important, such as the high throughput screening (HTS) methods commonly employed in various biological, chemical, and pharmaceutical domains.

In this work, we present a digital light processing (DLP)-based, rapid continuous 3D-bioprinting platform capable of automated well plate printing, for high throughput *in situ* fabrication of 3D tissue constructs of up to 96 samples per batch. This is especially significant when creating 3D tissue scaffolds where many functionally-identical copies of a particular sample may be required, especially in HTS operations where repeatability is paramount. Even in operations that print acellular scaffolds, such as those meant for implantation or regenerative medicine purposes, process time minimization is highly beneficial, as this allows for scalable and extensible processes. Using this high throughput 3D bioprinter (HT-3DP), we showcase system capability by presenting a variety of different 3D-printed spatial geometries and control over biomaterial mechanical properties. Additionally, we demonstrate direct in-well 3D bioprinting and culturing of biomimetic human hepatocellular carcinoma scaffolds, as well as an example of drug screening utility with a functional drug response validation test of a commonly-used

chemotherapy drug, and finally an example of dual-tissue printing capability. This work represents the first DLP-based 3D bioprinter capable of truly high throughput production of 3D tissue scaffolds of user-defined size, complexity, cell source, and tunable mechanical properties. A platform of this kind can be utilized to quickly and consistently produce custom tissue scaffolds on a high-volume scale and may accelerate discovery in such domains as pharmacological lead screening, disease modeling, and drug testing.

3.3. Results

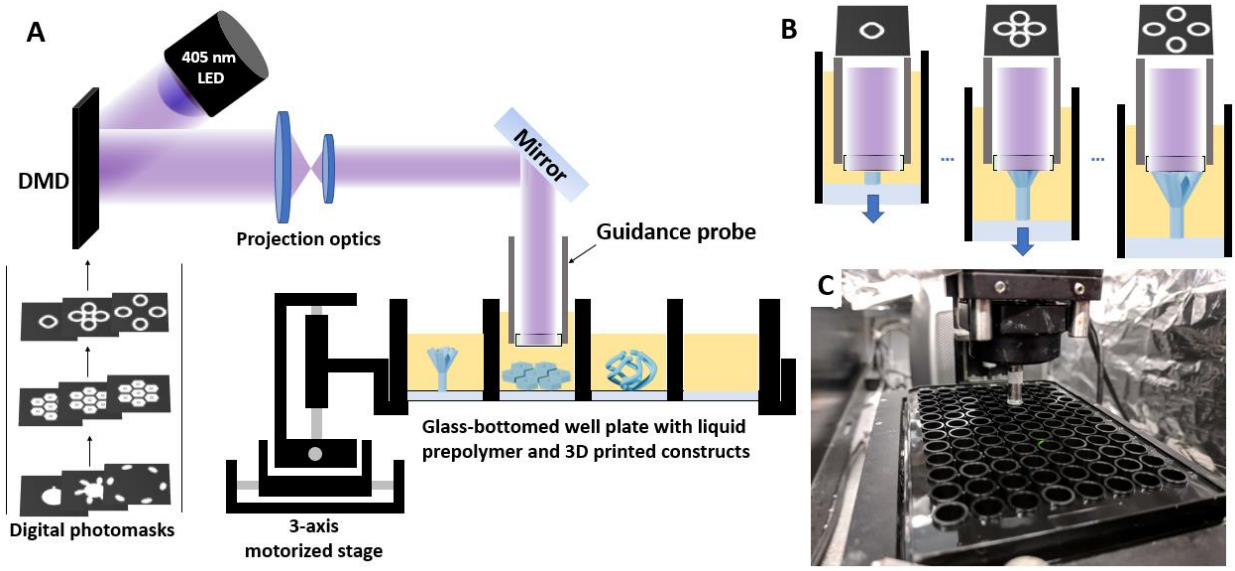

Figure 3.1: High Throughput 3D-Printing (HT-3DP) system.

A) Schematic depiction of high throughput 3D bioprinter (HT-3DP). Digital photomasks uploaded to a digital micromirror device (DMD) modulate projected light striking photosensitive prepolymer solutions held in a well plate on a 3-axis motorized stage. Computer-assisted synchronization of the light source, DMD pattern, and motorized stage enables rapid, continuous 3D printing on a high throughput scale. B) Schematic time lapse depiction of HT-3DP's rapid continuous 3D-printing of a single construct. As time moves forward, projected digital photomasks advance synchronously with controlled downward stage motion, enabling fast production of 3D constructs. C) Photograph of HT-3DP setup performing prints on a standard 96-well plate; probe shown in midground above the multiwell plate.

3.3.1. Design and Performance of the HT-3DP System

The core of the HT-3DP system shown in Figure 1A is the digital micromirror device (DMD, Texas Instruments), which has an array of approximately four million (2560x1600) individually-addressable micromirrors – these micromirrors can pitch at defined angles to selectively reflect incident light, such that adjusting the total array of micromirrors enables dynamic reproduction of any input 2D image. Supporting technologies for the HT-3DP system include: a visible light source in the form of a 405 nm light emitting diode (LED) for photopolymerization; projection optics for projecting the DMD-reflected light; a 3-axis motorized stage with a well plate holder; and finally a computer with custom software for coordinating all hardware components. Together, these allow dynamic flexibility and reproducibility of printing parameters.

The 3D-printing workflow is as follows: the desired 3D construct is designed in computer-aided design (CAD) software and then digitally 'sliced' into a series of individual 2D cross-sectional images, which are then uploaded into the DMD. These designs may come from patient-derived medical imaging data, e.g. magnetic resonance imaging (MRI) or computed tomography (CT) scanning, thus enabling close approximation of a desired tissue type, or alternatively be user-defined custom geometries. The light source is then used to illuminate the DMD's micromirror array, the resultant reflection creating a 2D plane of spatially-modulated light that then dynamically changes as the image sequence displays. The reflected light pattern is projected via optics through a hollow guidance probe, which by virtue of the 3-axis stage can descend into any given well of a well plate, which can be prefilled as needed with photosensitive prepolymer solution. The guidance probe's structure terminates with an optically clear glass window coated with polydimethylsiloxane (PDMS) to prevent adhesion of the polymerized

construct. For a given prepolymer solution formulation, final feature sizes are dependent on the terminal projected pattern – each pixel of the projected image is reflected by an individual micromirror on the DMD (around 7.6 μm in size), which when combined with select focusing optics, condenses the final image down to the microscale. The final resolution of the printed construct is dependent on a number of factors, including but not limited to: the optical setup used to focus the reflected image from the DMD onto the prepolymer solution, i.e. lense choice, aberrations, etc.; material-induced light absorption and/or scattering, and free radical diffusion into areas outside photoexcited areas. The guidance probe starts submerged and nearly flush with the bottom of the well, and selective photopolymerization of the solution trapped between the probe's surface and the bottom of the well occurs based on the pattern of incident light. With the guidance probe held stationary relative to the well plate, synchronization between the projected light pattern and the movement of the 3-axis motorized stage enables continuous photopolymerization of the solution, thus resulting in a 3D construct (Figure 1B) fabricated directly in any given well. Repetition and/or changing of print instructions can then occur across any arbitrary number of wells in the well plate. A photograph of the active build area can be seen in Figure 1C, where the guidance probe is shown in the midground above a 96-well plate suspended on the 3-axis motorized stage. For a given prepolymer hydrogel solution, total fabrication time is limited only by individual scaffold printing time and the time required to reposition the well plate for subsequent prints. Depending on the complexity of the printing structure, the total fabrication time for a fully-populated 96 well plate typically ranges from 20 to 40 minutes.

We chose to utilize poly(ethylene glycol) diacrylate (PEGDA) and gelatin methacryloyl (GelMA)-based materials as exemplars of the synthetic and biologically-derived materials

commonly used in tissue engineering, but in principle any material capable of undergoing photopolymerization would be compatible with the HT-3DP. This affords flexibility across a number of user-defined choices, such as selection of scaffolding material and cell type, or desired biological and mechanical properties. Our system is particularly well-suited for biological applications, as the use of a 405 nm LED visible light source to photopolymerize aqueous, biologically-derived solutions eliminates any potential concerns regarding UV-radiation damage to living cells.

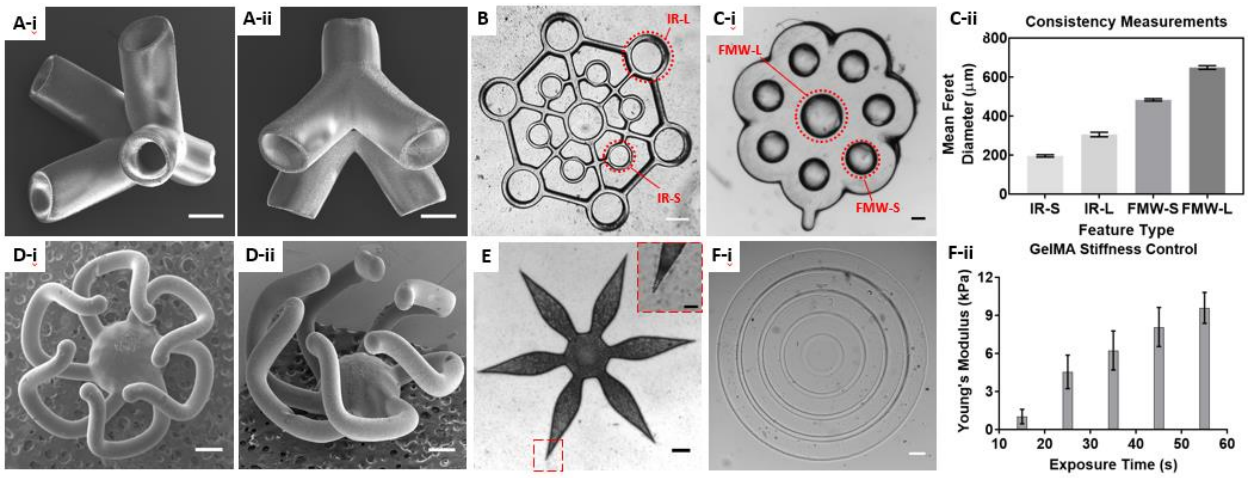

Figure 3.2: Various HT-3DP printed geometries and characterization data.

A-i,ii) SEM images of a bifurcated hollow tube; scale bar = 500 μm. B) Brightfield top-down image of hollow tubes and interconnected struts; scale bars = 200 μm. C-i) Flower-like microwells with smooth concavities; scale bar = 200 μm. C-ii) Quantitative plot showing the feature size precision for selected representative features across two 3D-printed constructs. Interlocking Rings – Small (IR-S, N=18) and Interlocking Rings – Large (IR-L, N=21) from Figure 2B; Flower Microwells – Small (FMW-S; N=42) and Flower Microwells – Large (FMW-L; N=6) from Figure 2C-i. Error bars are presented as standard deviations. D-i,ii) SEM images of parallel spirals construct; scale bar = 500 μm. E) Brightfield image of star-shaped construct; scale bar = 200 μm; inset shows sharp small feature < 10 μm; inset scale bar = 50 μm. F-i) Brightfield image of concentric GelMA rings printed with varying exposure times. Innermost dot received 15 seconds of exposure time and outermost ring received 55 seconds, with increments of 10 seconds; note increasing definition of ring borders from inner-to-outer; scale bar = 200 μm. F-ii) Quantitative plot showing relationship between compressive modulus and printing exposure time one day after printing. Error bars are standard deviation; N = 8 for all data points.

3.3.2. 3D-Printing of Biologically-Relevant Architectures

To establish HT-3DP fabrication capability, we 3D-printed exploratory architectures that employ a variety of different geometries and controllable parameters, using a PEGDA-based hydrogel. Figure 2 shows representative images of the various structures created, including 1) hollow bifurcations and complex tubes (Figures 2Ai, 2Aii, 2B), 2) smooth concave surfaces (Figure 2Ci) 3) overhanging structures (Figure 2Di, 2Dii), 4) sharp features under 10 microns in size (Figure 2E), and 5) concentric rings that also demonstrate control over hydrogel mechanical stiffness (Figure 2Fi, 2Fii). These shapes were chosen based as exemplars of features that may be found in biological reality, or features that would otherwise be challenging to produce using other 3D printing modalities – together they represent a wide dynamic range of the types of structural complexity, length scales, and feature sizes that might be encountered in generating tissue scaffolds.

3.3.3. Tunability of Scaffold Mechanical Properties

Figures 2Fi, 2Fii show our ability to control the mechanical properties of our scaffolds – free radical photopolymerization induces crosslinking in the target material, and by modulating factors such as base material composition, light intensity, and exposure time, we can tune the final mechanical properties of our tissue scaffolds by controlling the crosslinking density. Here, we held constant the constituent concentrations of one of our prepolymer solutions at 7.5% GelMA and 0.6% lithium phenyl-2,4,6-trimethylbenzoylphosphinate (LAP), as well as the intensity of the incident light at 16.7 mW/cm^2. Then, in a single print session that utilized a five-part image sequence comprised of concentric rings surrounding a circle, we varied the exposure time such that each separate part of the construct received a different exposure time, and evaluated the effects of exposure time on elastic modulus (Figure 2F-i). Starting from the

innermost ring and moving outwards, each ring received successively longer exposure times in 10 second increments, with the innermost ring starting at 15 seconds and the final ring receiving 55 seconds. As can be seen from Figure 2F-ii, we see that this linear increase in exposure time produces a similarly linear trend in elastic modulus, ranging from 1.03 ± 0.57 kPa at the softest to 9.60 ± 1.22 kPa at the stiffest – this allows for the ability to precisely modulate mechanical stiffness in the same scaffold in one single print. These results represent testing for a single variation of prepolymer hydrogel but are easily extensible to other formulations depending on the desired mechanical properties.

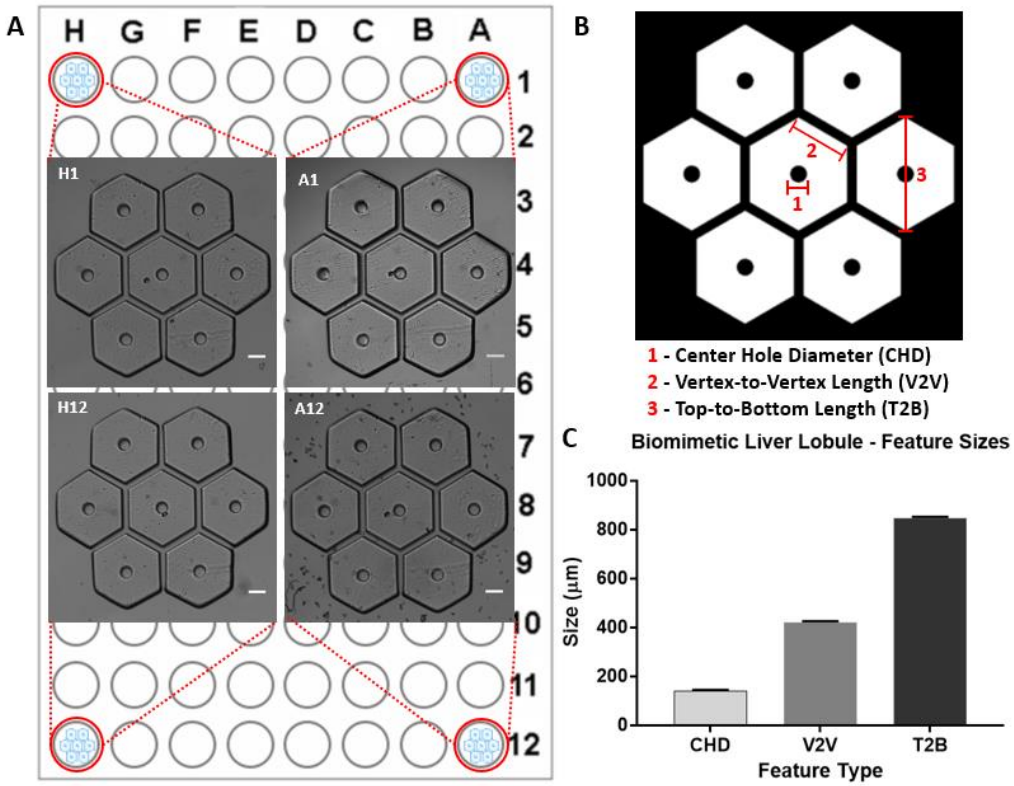

Figure 3.3: 96-wellplate extremes consistency check and characterization.

A) Schematic depicting the locations of the four extremes of a 96-well plate where the HT-3DP printed. Insets: Brightfield images of acellular 3D-printed biomimetic liver lobule scaffolds printed at the four extremes depicted in the background. Scale bars = 200 μm. C) Quantitative plot depicting consistency of size measurements of the features shown in Figure 3-B. CHD = "Center Hole Diameter" (N = 4); V2V = "Vertex to Vertex Length" (N = 24); T2B = "Top to Bottom Length" (N = 4). Data represented as means, with error bars representing standard deviation.

3.3.4. High Throughput Production and Consistent Reproducibility of Printed Scaffolds

The HT-3DP's 3-axis motion stage is designed to accept commercially-available standardized well plates (typical dimensions 127mm x 83 mm). With its current optics and guidance probe tooling, the system can accommodate well plate densities of up to 96-wells, allowing rapid 3D-printing of any user-defined scaffold across any arbitrary number of wells. As an example, utilizing a 24-well plate, we printed a tubular conduit approximately 2.5 mm in outer diameter and 3 mm in height with an individual print time of 10 seconds per well. Printing 24 copies of such a construct takes approximately just 16 minutes (Supplementary Video 1); scaling the same construct up to a 96-well plate would result in a total fabrication time of just under 40 minutes (Supplementary Video 2). By leveraging the standardization and consistency of well plate technology in conjunction with the speed afforded by our automated, micro-continuous projection printing method, we can dramatically improve our ability to 3D-bioprint structures on higher throughput scales.

We also evaluated the HT-3DP's ability to print scaffolds in terms of fabrication consistency, by having it print the same types of scaffolds multiple times in a row, and then comparing the measurements of select key features. Figure 2Cii shows the mean Feret diameters of four circular features in two of the exploratory architectures – Figure 2B shows a series of hollow tubes connected via struts, dubbed 'interlocking rings' (IR), and Figure 2Ci shows a flower-like microwell (FMW) series. In the interlocking rings (IR) structure, we measured the Feret diameters of both the small (IR-S) and large (IR-L) hollow cylinders present in the structure, and similarly in the flower-like microwell (FMW) structure we measured the Feret diameters of the small (FMW-S) and large (FMW-L) microwells. As can be seen from Figure 2Cii, each feature's standard deviation is small with respect to the original feature, with the

lowest and highest standard deviations recorded as ±5.82 μm for the IR-S and ±11.71 μm for the IR-L, respectively (2.98% and 3.83% of the original feature sizes, for N = 18 and N = 21, respectively). We conducted an additional test of print precision using a 96-well plate, fabricating acellular copies of a hexagonal scaffold biomimetically-inspired by liver lobule tissue in the four corner extremes of the plate (Figure 3A). These locations were chosen as exemplar positions after the system was calibrated to ensure any loaded multiwell plates were coplanar with the build probe at any arbitrary position. Quantitative measurements were taken of three physical features of scaffold and evaluated for precision: the center hole diameter (CHD), the vertex-to-vertex length (V2V) of one edge in the center hexagon, and the top-to-bottom length (T2B) of the vertical chord in the center hexagon (3B). As can be seen in Figure 3D, we evaluated printing precision in a manner similar to that of Figure 2Cii, where the standard deviation is small with respect to the feature size: the smallest and largest standard deviations recorded were ±1.71 μm for the CHD and ±4.4 μm for the T2B, respectively (1.19% and 0.52% of the original feature size, for N = 42 and N = 6, respectively).

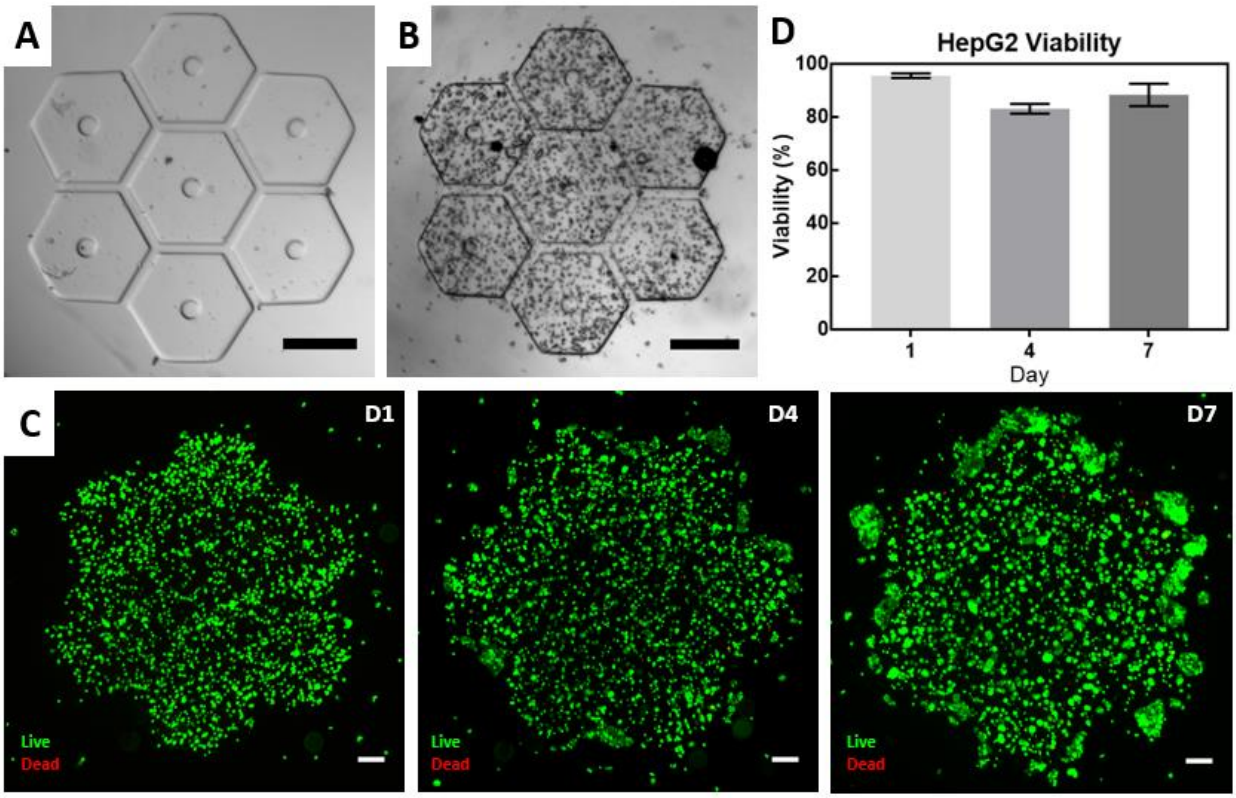

Figure 3.4: 3D bioprinted cancerous tissues + Live/dead.

A) Brightfield image of an acellular 3D-printed scaffold, biomimetically patterned after liver tissue; scale bar = 500 μm. B) Brightfield image of a HepG2-cellularized 3D-bioprinted scaffold; scale bar = 500 μm. C) Representative fluorescent images showing Live/Dead™ staining of HepG2-cellularized 3D-bioprinted scaffolds over 1, 4, and 7 days respectively; scale bars = 200 μm. D) Quantitative plot depicting HepG2 cell viability over the course of 7 days; viability remains >85% at day 7. Data represented as means, with error bars as standard deviation. N = 3 for all data points.

3.3.5. 3D-Bioprinting HepG2 Tissue Scaffolds and Functional Testing Against Doxorubicin

To establish the HT-3DP's live cell printing capability, we utilized a well-established hepatocellular carcinoma cell line (HepG2) in 3D-printing biomimetic liver-inspired tissue scaffolds, whose shape and dimensions were chosen to mimic native hepatic lobule structure[107]. The liver carries out many critical functions related to metabolism, with any dysfunction closely tied to both disease- and drug-related pathologies[161] – thus HepG2s serve as a suitable model cell line for testing tissue scaffold fabrication techniques. A 7.5% (wt/vol) GelMA hydrogel solution

was used, with print parameters chosen such that the final polymerized matrix stiffness was similar to that of native liver tissue. An acellular version was printed first to verify shape accuracy (Figure 4A). Following verification, HepG2 cells were mixed with the GelMA hydrogel solution at a final concentration of 3 million cells per mL, and then printed using the HT-3DP as previously described, thus creating a 3D-printed tissue model of hepatocellular carcinoma (Figure 4B). Live and dead cells were characterized by calcein AM and ethidium homodimer-I staining and imaged over the course of one week (Figure 4C). Live/dead quantification (Figure 4D) revealed that the majority of the cell population (>85%) were live cells at the end of one week, thus suggesting that the tissue scaffold was highly viable.

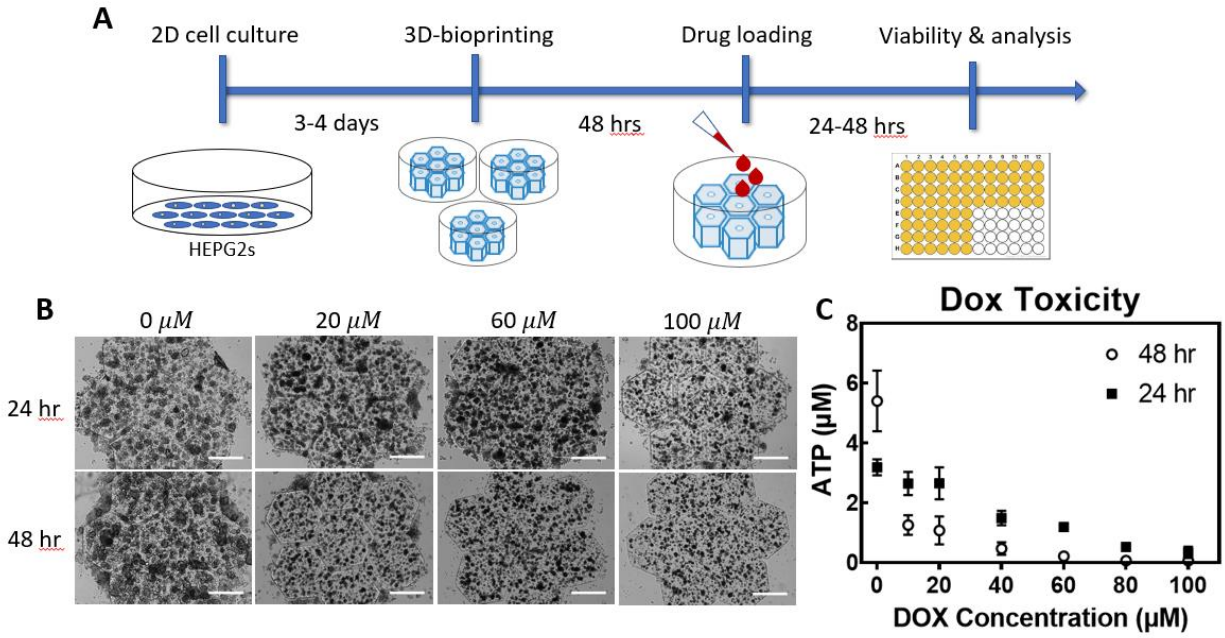

Figure 3.5: Doxorubicin viability testing of 3D bioprinted cancerous tissues.

A) Schematic depiction of the process timeline, starting from culturing and 3D-printing to drug loading and viability analysis. B) Representative brightfield images of HepG2 scaffolds at varying doxorubicin concentrations and time points; scale bars = 500 μm. C) Quantitative plot depicting results of CellTiterGlo-3D viability assay, where a decreasing trend in ATP concentration occurs as doxorubicin concentration and exposure time increases. Data represented as means, with error bars as standard deviation.

Having established HepG2 tissue viability, we next explored the functional utility of the 3D-bioprinted constructs, by conducting a simple well plate drug screening assay (Figure 5A), which we deemed a suitable stand-in for any arbitrary drug screening assay capable of being conducted in a well plate. We chose the well-established chemotherapy drug doxorubicin, which is commonly used to treat a number of oncological targets including liver-related issues in clinical patients, as well as in *in vitro* testing of human cell lines including HepG2[162]. 3D-printed HepG2 constructs were exposed to varying concentrations of doxorubicin, from 0 μM to 100 μM, and cell viability was evaluated at 24 and 48 hr time points afterwards (n = 3 per concentration, per time point, for a total of 42 samples). After the designated time points, a commercially-available cell viability kit (CellTiterGlo 3D) was used to assess relative cell viability, in which the amount of fluorescently-labeled intracellular ATP is used as a quantitative indicator of metabolically active (thus live) cells. Considering doxorubicin's use as a chemotherapy drug, we thus expected and subsequently observed a decrease in viable HepG2 cells as we increased the doxorubicin concentration and/or exposure time. Brightfield images of treated HepG2 scaffolds (Figure 5B) show how with increasing drug concentration, cell morphology visibly changes from the large, slightly translucent appearance of healthy cells to the shriveled, dark, and opaque characteristics of dead cells. This qualitative appearance is consistent with the quantitative data (Figure 5C), where a 2-way ANOVA was run on data from the 42 tissue scaffolds to compare the effect of doxorubicin concentration and exposure time on output ATP concentration. A significant effect of exposure time (p<0.0001), doxorubicin concentration (p<0.0001), and an interaction between exposure time and doxorubicin concentration (p<0.0001) was found. Therefore, ATP levels (thus cell viability) can be easily controlled using both exposure time

and/or doxorubicin concentration, confirming our expectations regarding the use of chemotherapeutic drugs on cancerous cells.

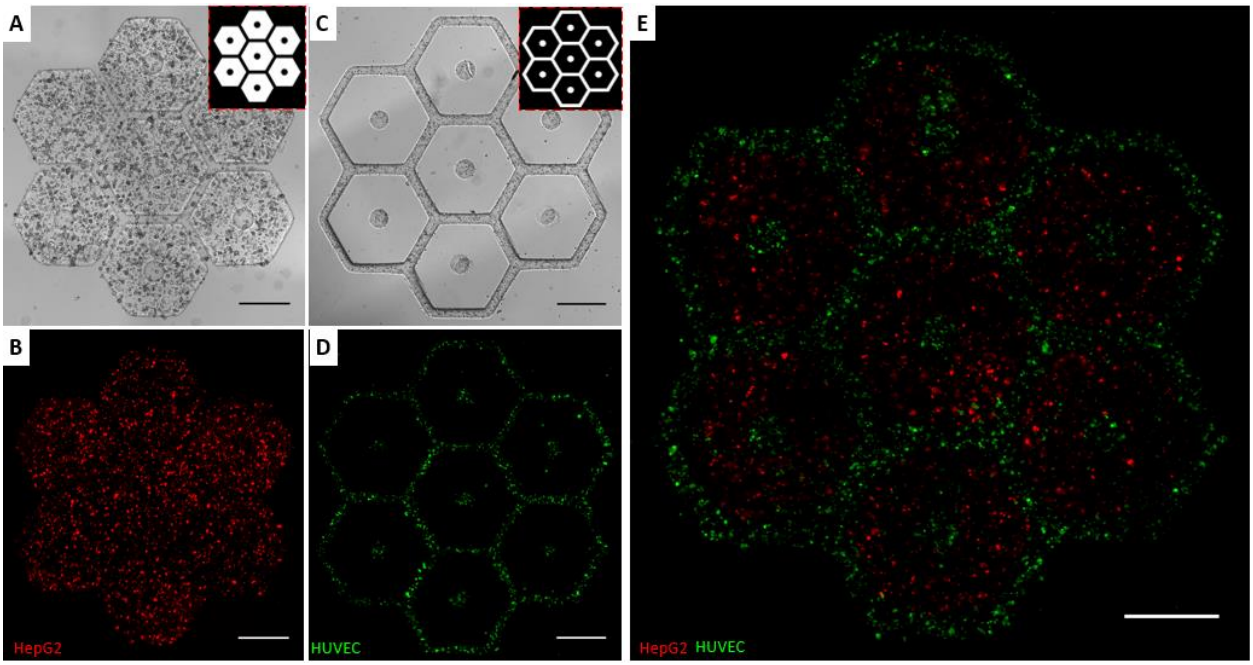

Figure 3.6: Dual cell population 3D-bioprinting of HepG2s and HUVECs.

A) Brightfield image of a HepG2-only tissue scaffold; inset: projected image pattern. B) Fluorescence image of a HepG2-only tissue scaffold. C) Brightfield image of a HUVEC-only tissue scaffold, colored red via RFP-transfection; inset: projected image pattern. D) Fluorescence image of a HUVEC-only tissue scaffold, colored green via CellTracker^{TM}-Green. E) Fluorescence image of a combined HepG2 and HUVEC tissue scaffold. Scale bars = 500 μm.

3.3.6. Dual Cell-Type Population 3D-Bioprinting

While we demonstrated the feasibility and utility of a HepG2-based tissue scaffold, it is composed of a single cell type. There is significant interest in tissue scaffolds incorporating multiple cell types, as these may better simulate the natural complexity of native tissues - interactions between multiple cell types may play crucial roles in various stages of development for both maturation and pathology-related domains[160]. To demonstrate the HT-3DP's capability in this regard, we fabricated dual-type tissue scaffolds (Figure 6) comprised of: HepG2 cells for their liver-specific drug response, and human umbilical vein endothelial cells (HUVECs) for

their well-documented vasculature-forming behavior[163] and potential interaction with fetal liver tissue[164].

Similar to the procedure used to print the HepG2-only tissue scaffolds, a 7.5% (wt/vol) GelMA, 0.6% LAP hydrogel solution was used as the carrier solution for the cell populations. HUVECs and HepG2s were grown using best 2D tissue culture practices, and subsequently incorporated into their own individual GelMA carrier solutions. With print parameters again chosen such that the final polymerized matrix stiffnesses were similar to that of their representative native tissue, the HUVEC-encapsulated GelMA was first printed *in situ* in the well plate to generate a 3D vasculature network, using a projection pattern 'inverted' from that of the HepG2 pattern (Figure 6A, 6B). After carefully flushing and removing the unreacted material, HepG2-encapsulated GelMA was input into the same well where the HUVEC-encapsulated print resided, and subsequently 3D-printed into the previously-used liver lobule shape (Figure 6C, 6D). Our control over the well plate's movement ensures close spatial coordinate registration, as can be seen in the spatial proximity of the two different tissue types even across two stages of printing (Figure 6E).

3.4. Experimental Methods

3.4.1. 3D Construct Build Materials

Poly(ethylene) glycol diacrylate (PEGDA, M_n =700 Da) was purchased from Millipore-Sigma (USA). Gelatin methacryloyl (GelMA) was synthesized as described previously[165]. Photoinitiator lithium phenyl-2,4,6-trimethylbenzoylphosphinate (LAP) was synthesized in-house as described previously[166]. Photoinitiator Irgacure 819 was purchased from BASF.

The printing solution used for demonstrating controllable spatial architectures (Figures 2A-2E) was a hydrogel solution based on PEGDA. The solution was prepared as follows: 50%

v/v PEGDA-700 as the prepolymer component, 1% wt/wt Irgacure 819 (BASF) as the photoinitiator, and 5% v/v yellow food dye (Wilton) as a visible light absorber for increasing spatial resolution, all in 1x Dulbecco's phosphate-buffered saline (DPBS) as the solvent. The printing solution used for demonstrating mechanical stiffness control and for the HepG2-encapsulated scaffolds was prepared by mixing GelMA at 7.5% wt/vol and LAP at 0.6% wt/vol in 1x DPBS. The printing solution used for printing the HepG2-encapsulated tissue scaffolds was prepared by mixing a solution of 15% wt/vol GelMA and 1.2% LAP wt/vol at a 1:1 ratio with a HepG2 cell suspension at a concentration of 6 million cells/mL, for a final solution of 7.5% wt/vol GelMA, 0.6% LAP, and 3 million HepG2 cells/mL. The printing solution used for printing the HUVEC-encapsulated tissue scaffolds was prepared by mixing a solution of 15% wt/vol GelMA and 1.2% LAP wt/vol at a 1:1 ratio with a HUVEC cell suspension at a concentration of 6 million cells/mL, for a final solution of 7.5% wt/vol GelMA, 0.6% LAP, and 3 million HUVECs/mL.

3.4.2. High Throughput 3D-Printer

All 3D-printed constructs shown in this work were printed via the described High Throughput 3D-Printer (HT-3DP) setup. The DMD chip utilized in the HT-3DP setup is the DLP® LightCrafter™ 9000 Evaluation Module (Texas Instruments), and has a 2560x1600 micromirror array. Constructs were digitally designed in CAD software (Autodesk, AutoCAD), with the resulting 3D models in .STL format sliced with in-house MATLAB script into a series of digital photomasks. Photomask series were digitally-uploaded to the DMD, with individual photomask display synchronized to digitally-controlled motion of a 3-axis motorized stage (Zaber) while under controlled illumination from a 405 nm visible light LED. Synchronization of

all hardware components was coordinated with a computer running in-house software (Visual Studio).

Briefly, the printing process is as follows: a defined volume of prepolymer solution is dispensed into a target well in a methacrylated[167] well plate placed on a controllable 3-axis motorized stage. Then, the well plate is maneuvered such that by way of relative positioning, the HT-3DP's printing probe is submerged in the target well, with the probe's bottom surface flush with the well's floor (or a methacrylated glass coverslip laid in said well, if necessary). A thin coating of polydimethylsiloxane (PDMS) adhered to the bottom of the probe head creates a non-stick surface – combined with the prepolymers' acrylate chemistry, this enables in-progress 3D constructs to preferentially stick to the targeted methacrylated well bottom, as well as ensuring long-term stable attachment during tissue culturing. At the start of printing, software coordinates the hardware components such that light source activation, DMD photomask sequence, and stage motion are synchronized – as the projected light pattern selectively photopolymerizes a volume of prepolymer solution, the stage (and thus the well plate) can move down relative to the probe's position, allowing fresh solution to move into the vacated space and be polymerized in turn. The stage motion can also be set to stationary, allowing the user to photopolymerize a static layer of prepolymer solution if desired. With full control over the stage's motion, the probe head itself can also be used to pre-agitate the liquid prepolymer in any given well, in the event of significant cell settling due to gravity over long time scales. In this way, the HT-3DP can rapidly and continuously print 3D constructs, as the combination of the projection of an entire 2D plane of light and controllable stage motion allows significant reduction in fabrication time compared to serially-printing extrusion-based printers.

3.4.3. Mechanical Stiffness Control

Concentric GelMA rings of varying stiffnesses showcased in Figure 2F were fabricated with our HT-3DP setup as previously described. The build material utilized GelMA, and was prepared as follows: 7.5% wt/vol GelMA as the prepolymer component, 0.6% wt/vol LAP as the photoinitiator, all in 1x Dulbecco's phosphate-buffered saline (DPBS) as the solvent. A five photomask series was used, starting with a 500 μm diameter circle in the center, followed by four nested rings of increasing diameter; the outermost ring has a diameter of 3.5 mm, and each ring has a lateral thickness of 250 μm. The innermost dot received 15 seconds of 405 nm light exposure time, and going outwards, each subsequent ring received an additional 10 seconds of exposure time, for a final exposure time of 55 seconds for the outermost ring.

3.4.4. Liver-Biomimetic and Vasculature-Biomimetic Tissue Scaffolds

The hexagonal liver-biomimetic scaffolds (2.4mm x 2.4mm x 250μm), both acellular and cell-laden versions, were fabricated with our HT-3DP setup as previously described. A liver-biomimetic design was used to create the photomask series. The vasculature-biomimetic scaffolds shown in the dual cell population prints were similarly patterned and fabricated. The build material used for these prints was GelMA - acellular versions used 7.5% wt/vol GelMA + 0.6% wt/vol LAP solution as previously described, and the cell-laden versions used the same, with the addition of the respective cell type at a final concentration of 3 million HepG2s or HUVECs cells/mL. HepG2 (human hepatocellular carcinoma, ATCC) and HUVEC (human umbilical vein endothelial cell, ATCC) were cultured using standard 2D cell culture best practices. HepG2 cells were maintained in Dulbecco's modified eagle medium (DMEM, Gibco) supplemented with 10% fetal bovine serum (FBS), 1% PenStrep, and 0.2% Normacin. HUVECs were maintained in Endothelial Cell Growth Medium-2 (EGM^{TM}-2, Lonza) supplemented with

EGM™-2 SingleQuots™ supplements). Before bioprinting, HepG2 or HUVEC cells were digested via 0.05% trypsin-EDTA and gently mixed with pre-prepared GelMA/LAP hydrogel prepolymer for a final solution consisting of 7.5% wt/vol GelMA, 0.6% LAP, and 3 million cells/mL density. Fluorescence in the dual cell population prints was achieved via Red Fluorescent Protein (RFP)-transfection of the HepG2s (shown in red) and CellTracker™-Green (ThermoFisher Scientific) staining of the HUVECs.

3.4.5. Micro-Mechanical Testing

GelMA hydrogels used for the hepatocellular carcinoma scaffolds were measured for their bulk elastic modulus via micro-scale compression testing on the commercially-available platform 'Microsquisher' (CellScale), with results gathered through the included software (SquisherJoy). Briefly, the system operates by means of a piezoelectric actuator moving a cantilever of defined stiffness against a target sample – this cantilever compresses the sample while in view of a high-resolution camera. By comparing on-screen cantilever displacement with force data measured during compression, the elastic modulus can be calculated from the linear region of the generated stress-strain curve, which was done by in-house MATLAB scripts. Cylindrical samples (D=500 μm, H=250 μm, N=6 per exposure time) matching the exposure times of the individual concentric rings construct were compressed at 10% strain with a 2 $\mu m/s$ strain rate after overnight acclimation in a room temperature 1x DPBS bath.

3.4.6. Image Acquisition and Processing

Scanning electron microscopy (SEM) images of both the 'bifurcated tube' and 'parallel spirals' constructs were prepared as follows: a cleaning soaking session in 100% isopropyl alcohol (IPA), followed by air-drying at room temperature for 24 hours, then sputter coating with iridium for 7 seconds, followed by imaging using a Zeiss Sigma 500 scanning electron

microscope. Brightfield and fluorescence images of all other 3D-printed constructs were acquired with a Leica DMI 6000B microscope (Leica Microsystems), with 2.5x or 5x objectives and included tile-and-stitch software. Photographs and video of HT-3DP infrastructure taken via consumer DSLR and smartphone cameras. FIJI/ImageJ (National Institutes of Health) was used to collect measurements for feature size comparison and consistency check data.

3.4.7. Quantification of Feature Sizes in 3D-Printed Constructs

Brightfield images of 3D-constructs were taken via light microscopy (Leica) at 5x magnification and processed in image analysis software FIJI/ImageJ (NIH). For measurements made for ellipsoidal regions of interest, minimum and maximum Feret diameters were obtained for each region of interest via manual fitting of the oval-shaped measuring tool. Data reported as mean $\pm$ standard deviation, where the mean was calculated as the square root of the product of the minimum and maximum Feret diameter. For edge length and otherwise non-ellipsoidal regions of interest, measurements were obtained via the line measuring tool, and data reported as mean $\pm$ standard deviation.

3.4.8. Statistical Analysis

Data points on all graphs represent mean values, with error bars representing standard deviation where stated. Visual inspection of box-and-whisker plots revealed normally distributed data with no significant outliers. A 2-way analysis of variance (ANOVA) with replication was conducted on doxorubicin toxicity data. All statistical analysis and associated graphical output was done using Excel (Microsoft) or GraphPad Prism (GraphPad**)**.

3.4.9. Quantification of cell viability in Live/Dead® assay

A cell viability assay kit (LIVE/DEAD$^{(R)}$ Viability/Cytotoxicity Kit, Invitrogen) was used to assess cell viability for the constructs on Days 1, 3, and 7 post-printing. Briefly, the

tissue constructs (n = 3 for each time point) were washed with 1x DPBS after removing the culture medium, after which they were stained with a solution comprised of 2 μM calcein AM (live cell stain) and 4 μM ethidium homodimer-1 (dead cell stain) in DPBS. After incubating at 37 ºC for 30 minutes, fluorescent and bright field images of the constructs were taken with a Leica DMI 6000B microscope (2.5x Objective, Leica Microsystems). Live/dead cells were counted manually in FIJI/ImageJ (NIH) in blinded experiments for each sample, with data reported as mean ± standard deviation.

3.4.10. Quantification of cell viability in doxorubicin exposure and CellTiter-Glo(R) luminescent assay

Liver tissue constructs (2.4mm x 2.4mm x 250μm) were printed with 7.5% GelMA + 0.6% LAP, encapsulating 3 million/mL HEPG2 cells, and were allowed to grow. At Day 3 post-fabrication, the constructs were exposed to varying concentrations of doxorubicin {0, 10, 20, 40, 80, and 100 μM, N=4 for each concentration}, for two different time points {24 and 48 hours, N=4 for each time point}. Doxorubicin solution preparation was as follows: powdered drug was resuspended in DMSO to a stock concentration of 80 mM. An aliquot was taken and further diluted to 10 mM, upon which 0, 2, 4, 8, 16, and 20 μL were added to separately prepared aliquots of 2 mLs prepared cell culture media to make 0, 10, 20, 40, 80, and 100 μM doxorubicin solutions, respectively. The cell constructs in the well plates were aspirated of any existing media, and were then loaded with the doxorubicin-laced media. After 24 hours of doxorubicin exposure, a CellTiter-Glo® luminescent cell viability assay kit was used as recommended to assess the cell viability of the constructs post-doxorubicin exposure. The assay indirectly determines cell viability by quantitating the amount of ATP present, an indicator of metabolically active cells. After the requisite amount of drug exposure, the first step of the CellTiter-Glo® assay was

performed, where a cell lysis reagent was added to wells containing the cell-laden scaffolds, thus lysing any cells present and releasing intercellular ATP content into the surrounding solution. Afterwards, a secondary reagent was added that luminesces on interaction with ATP – the strength of the luminescence is quantifiable by means of a luminescence plate reader (Infinite 200 PRO, Tecan, Mannedorf, Schweiz), and is directly proportional to the amount of ATP present in the solution. By comparing the luminescence values of our samples against a co-prepared standard curve, we can establish a relative assessment of cell viability.

3.5. Discussion and Outlook

In recent years 3D-bioprinting technology has advanced greatly, with a widely-varying selection of modalities, from extrusion-based to light-based techniques[168]. Extrusion-based 3D bioprinters have previously shown promise in structured dispensing of hydrogel biomaterials and/or cells to create novel and functional tissue models of varying types[108,169], but invariably have resolution and throughput limitations due to extrusion aperture constraints and their serialized approach to 3D-printing, respectively[170]. Certain types of light-based 3D bioprinters, such as 3D-stereolithography (SLA) systems, can circumvent the physical limitations of nozzle extrusion by directly tracing lines of photopolymerization of aqueous hydrogels, yet are still hampered by the nature of serial printing, as 'line-by-line scanning' is inherently slower than 'layer-by-layer'[168]. Digital light processing (DLP)-based systems can further overcome the limitations of serial-type light-based 3D-printers by projecting entire 2D planes of light in a layer-by-layer fashion, which can significantly lower the total fabrication time due to the elimination of serial scanning processes[171]. Indeed, DLP-based 3D bioprinters have demonstrated the ability to produce sophisticated 3D tissue scaffolds across a range of different tissue types,

including vasculature[106,108], cardiac tissue[172], skeletal muscle[173], hepatic tissue[107,174], and the nervous system[175].

Recently, further DLP-based advancements have been shown, including the use of grayscale for functional grading[176], construct layer continuity[177], and even transitioning from layer-to-layer to volumetric-style printing[178–180]. While such techniques can print complex structures of varying length scales quickly, and indeed offer improved resolution and printing speed compared to their extrusion-based counterparts, these tend to be limited to 'single-vat' prints, not compatible with HTS which is often conducted in a multiwell plate. In HTS, large numbers of easy-to-use, consistent, and functional samples are required for ensuring accurate assays and evaluations; existing systems capable of high throughput printing of biological constructs tend to sacrifice 3D sophistication in favor of speed[181–183]. Thus, there is an unmet need for a 3D-bioprinting system capable of fabricating complex tissues, with an emphasis on high throughput scale.

Our HT-3DP system combines micro-continuous projection printing with automated well plate registration to quickly and scalably generate 3D tissue constructs at high throughput scales, thus overcoming limitations that other 3D bioprinters may have. With this technique, we were able to quickly produce 3D biomimetic HepG2 scaffolds for a functional drug response assay in the same well plate they were printed in, with minimal post-print processing. The materials used in printing are biocompatible, quickly photopolymerizable, and tunable for both feature resolution and mechanical properties. While this setup necessarily requires the use of photocrosslinkable materials, this technology is not solely limited to those – other naturally-derived materials yet non photocrosslinkable materials such as collagen, Matrigel, fibrin gels, or even animal-derived decellularized extracellular matrices[165,184] can be included in composite

formulations with a photopolymerizable material such as GelMA as the carrier component, so as to confer their biologically-beneficial properties to the final product.

The HT-3DP's enabling of direct encapsulation of chosen cell types with biocompatiable materials enables facile creation of 3D tissue models with immediate utility. While we chose a cellular density of 3 million cells per mL to mitigate light scattering issues and to better showcase the structural features of our tissue scaffolds, previous works utilizing similar light-based 3D printing have successfully printed tissue scaffolds with cell densities as high as 40 million cells per mL[107]. The dose- and time-dependent doxorubicin toxicity of our 3D-printed HepG2 scaffolds are comparable with previous reports using similar drug concentrations[185]. Additionally, the tested dosages of doxorubicin fall within the ranges commonly used in therapeutic settings, and the extremes mimic those of other studies that perform similar doxorubicin dosage testing[185,186]. The doxorubicin assay, while simple in concept, is both extensible and scalable to potentially any *in vitro* drug screening assay that can be conducted in a well plate, underscoring the utility of the HT-3DP's ability to produce 3D tissue constructs on a high throughput scale. Furthermore, we show that the HT-3DP can print even more complex tissues by printing more than one cell type within the same construct, by printing the same HepG2 scaffold surrounded by a biomimetic vasculature network comprised of encapsulated HUVEC cells. This technique demonstrates how the HT-3DP can expand its application to creating models or pathologies that affect more than one tissue domain.

In summary, we present a 3D-bioprinting platform, capable of rapid, continuous 3D printing of constructs for drug screening purposes on a high throughput scale. We demonstrate capability in fabrication of small feature sizes (<10 microns), consistent reproduction of complex shapes, as well as mechanical property control over tissue scaffold stiffness. Our HT-3DP system

combines micro-continuous projection printing with automated well plate printing to quickly and scalably generate functionally-identical 3D tissue models in standard well plates, enabling *in situ* well plate-based assays of functional drug response of human-type tissues. Future work in this domain may include enhancing the parallelization of fabrication, for even higher throughput scaffold production. Compared to lower-volume throughput 3D bioprinters, we anticipate that platforms such as our HT-3DP would create a new paradigm for drug and small molecule discovery, because high throughput combinatorial-screening investigations can potentially be conducted against 3D human-type tissue models instead of 2D monolayer cultures or non-human animal models, thus greatly increasing the efficiency of the drug discovery process.

3.6. Acknowledgements

The authors would also like to thank Dr. David Berry for mentoring and advice. This work was supported in part by grants from the National Institutes of Health (R01EB021857, R21AR074763, R33HD090662) and National Science Foundation (1644967, 1937653).

Chapter 3, in full, includes a reprint of the published article, "High Throughput Direct 3D Bioprinting in Multiwell Plates." Hwang, Henry H.*; You, Shangting*; Ma, Xuanyi; Kwe, Leilani; Victorine, Grace; Lawrence, Natalie; Wan, Xueyi; Shen, Haixu; Zhu, Wei; Chen, Shaochen. Biofabrication, 2021. The dissertation author was a co-primary investigator and co-first author of this work. * = these authors contributed equally.

3.7. Supplementary Material

Movie 3.1: 10x timelapse of HT-3DP system executing dry-run of 24-well plate.
Individual constructs were 10-second prints.

Movie 3.2: 10x timelapse of HT-3DP system executing dry-run of 96-well plate.
Individual constructs were 10-second prints; four sequent prints conducted. 96-well run truncated to avoid excessive video run time.

CHAPTER 4: HUMAN PLACENTA-ON-A-CHIP: A BIOMIMETIC MICROFLUIDIC 3D TRANSPORT MODEL (WORK IN PROGRESS)

4.1. Abstract

The human placenta is a vital component of pregnancy, functioning as both a selectively permeable barrier and a vital material exchanger between the maternal and fetal circulatory systems, thus providing a safe environment for both the mother and fetus during gestational development. Existing *ex vivo* systems lack long-term viability and standardization between setups, and *in vivo* animal models lack sufficient human physiological relevance. Additionally, due to the myriad physical and ethical challenges associated with studying human female reproductive system physiology *in vivo*, there is significant interest in the creation of *in vitro* microphysiological systems that can accurately recapitulate both structure and function of the native placenta. In this report we describe the creation of a novel tri-coculture 3D placenta-on-a-chip microphysiological system, in which 3D-printing, microfluidics, and 2D/3D cell culture is used to emulate the maternal-fetal interface *in vitro*. Primary placenta-derived stromal fibroblasts (PDSFs), human trophoblast stem cells (hTSCs), and human umbilical vein endothelial cells (HUVECs) are 3D-bioprinted and seeded into a hybrid open/closed microfluidic device, where they are grown under both static and perfusion flow conditions. Tri-coculture viability and showcase salient physiological and functional aspects of the membrane were assessed. Various barrier integrity assays were also performed, including tetrazolium dye viability (XTT) assay, sodium fluorescein transport, and glucose molecule transport. This placental microphysiological system may provide a potentially useful model for investigating both fundamental understanding and translational studies for female reproductive health.

4.2. Introduction

The human placenta is a remarkable organ, and part of a complex system of reproductive physiology involved in the gestation, sustenance, and growth of a fetus during pregnancy. There is significant interest in studying the placenta, ranging from the need to track gestational development and fetal health during pregnancy, to the effect of endogenous risks such as genetic abnormalities, to the effect of exogenous factors such as environmental pollutants and pharmaceutical compounds. In particular, pharmaceutical and medication use during pregnancy has increased significantly over the last three decades, with the use of four or more medications more than tripling – by 2008, approximately 50% of women reported taking at least one medication[187]. Existing approaches to study the human placenta include a) *ex vivo* perfusions of placental tissue explants, b) *in vivo* examinations of animal models such as mouse, rabbit, or goat, c) *in vivo* examinations of human females actively undergoing gestation, and/or d) *in vitro* recapitulations of some aspect of placental tissue, usually in a microfluidic microphysiological system[188].

Each of these approaches have their advantages and disadvantages: a) *ex vivo* perfusions of donated placental tissue are difficult to standardize between patients and typically have short lifetimes[189]; b) *in vivo* examinations of animal models lack relevance to human physiology[190]; and c) *in vivo* examinations of actively gestating humans have obvious physical and ethical challenges. *In vitro* recapitulations in a microfluidic model, or microphysiological system, have the highest potential for standardized fabrication, long-term culture, physiological relevance, and experimental control. Indeed, in recent years there have been several microphysiological systems that aim to recapitulate the unique physiological and functional aspects of the human placenta, typically involving a synthetic membrane cell culture insert like the commercially available

Transwell (Corning)[191] or natural materials like vitrified collagen[192]. Common themes to these microfluidic *in vitro* models include two separate layers, or compartments, separated by the aforementioned membrane, with appropriate model cell lines for the maternal and fetal 'sides' seeded within their respective chambers[192–199]. A fundamental challenge of attempting to recapitulate human placental physiology using microfluidics is associated with the simplification of the placenta system to a closed bicameral microfluidic device such as the ones shown in previous literature. The 'closed' nature of the microfluidic device makes it challenging to include the multiple cell types and spatial localization necessary to better recapitulate the placental barrier. Additionally, most of the cell types used in these previous studies are limited to immortalized lines derived from carcinogenic sources, such as BeWo, JEG3, and JAR, thus making their behavior and expression profiles markedly different from that of healthy placenta tissue[200].

There is room for optimization in this space, where: A) cells derived from primary human placenta tissue can be more physiologically relevant than immortalized carcinogenic lines, B) multiple cell types can be co-cultured in spatially distinct, 3D form factors that better recapitulate placental structure, and C) perfusion can be utilized to have dynamic microenvironmental control over fluid and concentration gradients. In this report we describe the creation of a novel 3D microfluidic *in vitro* model of the placenta, utilizing a combination of 3D-printing, microfluidics, as well as both 2D and 3D cell culture. Using our biomimetic microfluidic 3D transport model, we showcase its ability to recapitulate some of the salient physiological and functional aspects of actual placenta tissue. We co-culture three different human cell lines (primary human-derived placental stromal fibroblasts, primary human-derived trophoblast stem cells, and human umbilical vein endothelial cells), and show that the model

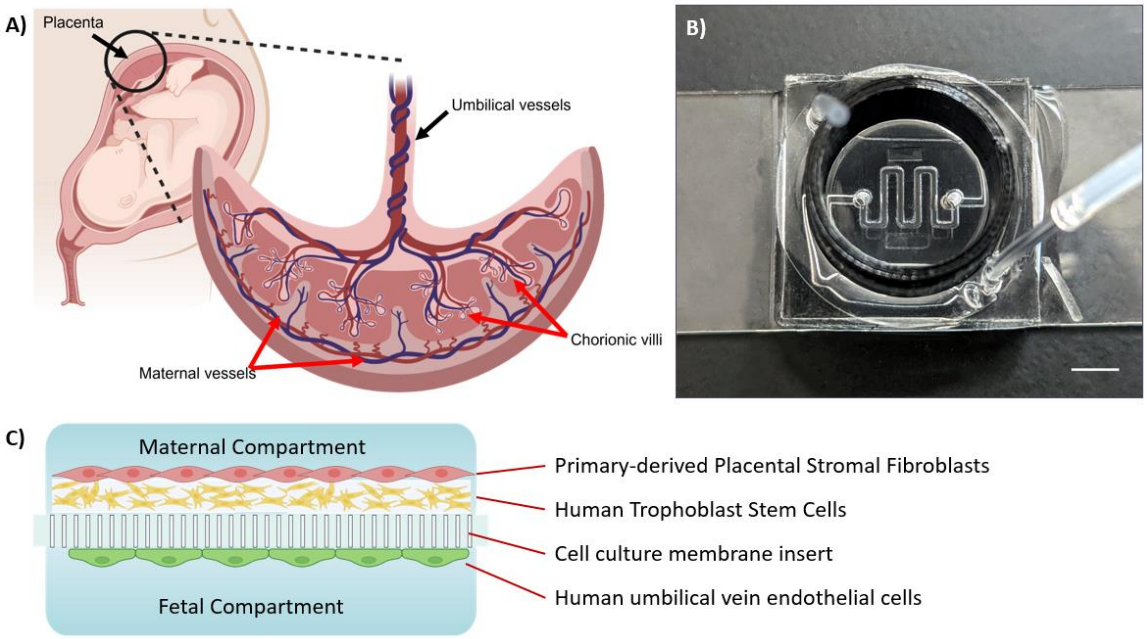

Figure 4.1: Microfluidic placenta-on-a-chip device.

A) Schematic representation of the human placenta, with callouts to the chorionic villi that facilitate the maternal-fetal exchange. B) Photograph of an acellular microfluidic placenta device. This is a sandwiched multi-layer construction, with a fetal 'capillary' channel of cross-sectional dimension 0.5 x 0.5 mm visible in the center of the device. Scale bar is 5 mm. C) A schematic representation of the cross-section of the tri-coculture model used in this study, where two primary-tissue derived human cell lines are used in the maternal compartment, and a human umbilical vein endothelial cell line used in the fetal compartment. A, C) Figures created using Biorender, with permission.

maintains both viability and functionality over the course of the model's lifetime. Assays were also performed to assess barrier integrity, including Cell Proliferation Kit II (XTT) assay, sodium fluorescein transport, and glucose molecule transport. This work has the potential to significantly advance fundamental understanding and translational work for women's reproductive health.

4.3. Methods

4.3.1. Materials synthesis and preparation

For fabricating the positive master molds of the fetal capillary compartment and fluidic reservoirs, a poly(ethylene glycol) diacrylate (PEGDA)-based solution was used. The photoinitiator phosphine oxide, phenyl bis(2,4,6-trimethylbenzoyl) (trade name: Irgacure-819,

BASF) was added to 100% (w/v) liquid PEGDA-250 (MW 250, Sigma-Aldrich) for a final concentration of 1% photoinitiator (w/v).

For the PDSF-encapsulated layer of the maternal compartment, a gelatin methacryloyl (GelMA)-based bioink was used as the carrier. The GelMA was synthesized as previously described[201], and used at a 7.5% (w/v) concentration in 1x DPBS. The photoinitiator lithium phenyl-2,4,6 trimethylbenzoylphosphinate (LAP) was synthesized as previously described[201], and added to the 7.5% GelMA solution at a final concentration of 0.6% (w/v).

The polydimethylsiloxane (PDMS) used during the construction of the device was Sylgard 184 (Dow Corning) and used at a standard 1:10 mass ratio of curing agent and elastomeric base. Components were weighed and mixed using a planetary centrifuge (ThinkyMixer) in a cleanroom environment.

4.3.2. Primary Cell Culture Viability Optimization on 3D Bioprinted GelMA Slabs

GelMA slabs of varying stiffnesses were DLP-3D printed, with either PDSFs encapsulated within during the time of printing or hTSCs seeded atop afterwards. PDSFs were encapsulated at a density of 75,000 cells/mL, and hTSCs were seeded at a density of 300,000 cells/mL and maintained in their respective growth media for seven days. Live/Dead viability testing was done on Days 1, 3, and 7 to assess cell viability of the cells at varying stiffness conditions to optimize the material properties of the gel layer present in the maternal compartment.

4.3.3. Placenta-on-a-Chip Device Design and Fabrication

DLP-based 3D printing was utilized as previously described[72], where a PEGDA-250 + 1% Irgacure 819 solution was 3D printed into glass-bonded microfluidic master molds for polydimethylsiloxane (PDMS) microcasting. Microfluidic architecture was designed using

computer-aided design (CAD) software (AutoCAD, Autodesk). An in-house DLP-based 3D-printer was utilized to fabricate positive master molds out of the 100% PEGDA-250 + 1% Irgacure-819 solution for both the microfluidic fetal capillary compartment and fluid reservoirs. Due to low fluid volume within the fetal capillary compartment, additional microfluidic fluid reservoirs were aligned and stacked with the fetal capillary to augment the local media reserves - this had the effect of extending time-between-feedings during HUVEC static culture. PDMS was mixed at a 1:10 mass ratio, poured over the master molds, de-gassed, and cured overnight at 80C. The fetal capillary compartment and fluidic reservoir devices were cut, ported, and oxygen-plasma bonded in a cleanroom-grade space.

For the membrane separating the fetal and maternal sides of the device, a commercially available cell culture insert membrane (polyethylene terephthalate with 0.4-micron pores, cellQART) was used. A 1:1 mixture of toluene and standard-mix PDMS was spun-coat onto a glass slide (60s, 1500 RPM) to function as 'glue,' after which the fetal side of the device-in-progress was 'stamped' onto the spun-coat to coat the negative spaces without adversely impacting channel patency. The membrane was aligned and placed atop the fetal capillary space, and cured for ten minutes at 80C. Afterwards, the retaining cup of the cell culture insert was bonded atop the membrane with additional PDMS, thus completing the maternal compartment. Microfluidic tubing (0.5 mm ID, Tygon, Cole-Parmer) was used to interface with the ports in the device, as well as with the peristaltic pump (PeriWave Micro, CorSolutions) used to perfuse the system.

4.3.4. Cell Culture: Tri-coculture model components and assembly

The current study involving human-sourced tissues used in biomedical research was approved by the Institutional Review Board.

Primary Placenta-Derived Stromal Fibroblasts (PDSFs): After obtaining written informed consent from donors, third trimester placenta (gestational age 36 to 38 week) from uncomplicated pregnancies were collected and transported to the lab on ice, within 1 hour of delivery. Primary placenta-derived stromal fibroblasts (PDSFs) were isolated from placental chorionic villi using the explant culture method as previously described by Igura K. et al[202]. Briefly, the basal and chorionic plates were excised using surgical scissors and discarded to avoid any maternal cell contamination. Then, lobes of placental villi were dissected from the placenta (avoiding large blood vessels) and rinsed thoroughly in sterile phosphate-buffered saline (1x DPBS) until all maternal blood was washed away. Each villus section was placed in a petri dish of warm DMEM-high glucose media and dissected into 7 mm to 10 mm-wide explant villi. Ten such explants were attached onto 10 cm TC-treated culture dishes and allowed to dry for 1 hour at room temperature. Once the explants were attached to the plate, 15 mL of warm growth (DMEM-High glucose + 10% FBS + 1% Penicillin-Streptomycin) was gently pipetted from the side, being cautious not to dislodge the explants. These plates were cultured in a humidified incubator at 37^{0}C, 5% CO_2 and normoxia for up to 4 weeks during which placental fibroblasts began to migrate out of the cut explants. Growth medium was replenished once every 3 to 4 days. The migrated cells were harvested using 0.05% trypsin-EDTA solution (3 minutes at 37°C) and subcultured for LN2 banking and future experiments. The cells used for encapsulation studies were within 12 population doublings (approximately four to six passages).

Human Trophoblast Stem Cells (hTSCs): Human trophoblast stem cell (hTSCs) lines were established from 1st trimester (6 to 8 week GA) placenta as described by Okae et al.[203] and maintained in tissue culture plates coated with 5 μg/mL collagen-IV (C0543-1VL, Sigma-Aldrich) and iCTB media (Advanced DMEM/F12 supplemented with 1x N2/B27 supplements, 2

mM glutamine, 150 μM 1-thioglycerol, 0.05% BSA, and 1x KSR) with 2 μM CHIR99021, 500 nM A83-01, 1 μM SB431542, 5 μM Y-27632, 0.8 mM valproic acid sodium salt, 100 ng/ml FGF2, 50 ng/ml EGF, 20 ng/ml Noggin, and 50 ng/ml HGF). For the induction of multinucleated syncytiotrophoblast (STB) formation *in vitro*, hTSCs were switched to STB differentiation media (Advanced DMEM/F12 (no HEPES, ThermoFisher Scientific) supplemented with 1% ITS-X, 3.2% KSR, 30% BSA, 55mM beta-mercaptoethanol, 10 mM Y27632, and 10 mM forskolin).

Human Umbilical Vein Endothelial Cells (HUVECs): Human umbilical vein endothelial cells (HUVECs) were purchased from the American Type Culture Collection (ATCC). Prior to seeding within the device, they were maintained via 2D culture in EGM-2 endothelial cell growth medium containing 2% FBS and VEGF (Lonza). During static culture in the model, media was manually replenished daily, and then replenished continuously during perfusion.

Multicellular Assembly into Tri-coculture 3D Model: Prior to cell culture, both the fetal and maternal compartments of the device were incubated for at least 1 hour at 37°C using a solution consisting of 5 μg/mL rat tail collagen type I and a 1:25 dilution of bovine plasma-derived fibronectin in 1x DPBS, to augment cellular attachment. On Day 1, we created the placental-derived stromal fibroblast (PDSF) layer in the maternal compartment, with a 7.5% GelMA + 0.6% LAP solution used as the carrier solution to encapsulate approximately 75,000 DiD-stained PDSFs. DLP 3D bioprinting was used to create a 125 μm thick layer of GelMA-encapsulated PDSFs atop the cell culture insert that separated the maternal compartment from the fetal compartment. The following day (Day 2), HUVECs at a concentration of approximately 8E6 cells/mL were manually seeded into the fetal compartment and statically cultured for two days. On Day 3 of culture, the human trophoblast stem cell (hTSC) layer was created by suspension-seeding approximately 500,000 hTSCs atop the PDSF-encapsulated layer formed on

Day 1, with gravity assisting the hTSC deposition process while they grew in iCTB media. On that same day, a peristaltic pump (PeriWave Micro, CorSolutions) was used to begin perfusion on the fetal chamber of the device at a volumetric flow rate of 3.5 µL/min, and was subsequently perfused for an additional three days. The maternal supernatant was collected daily over those three days, with maternal compartment media being replaced with STB-specific media with forskolin in it. After 3 days of syncytialization and perfusion, placenta barrier formation and integrity checks such as viability assays, fluorescent molecule transport assays, and imaging were conducted.

4.3.8. Imaging and Characterization

An upright fluorescence microscope with motorized stage (Leica DMI6000B, Leica Microsystems) was used in conjunction with a stage top cell culture incubator (Tokai Hit, Incubation Systems for Microscopes (INU) for continuous live imaging of the tri-co-culture system for the first day after perfusion was introduced into the system. 5x tile scan images were taken across multiple fluorescence emissions at defined time points, and images were automatically mosaic-merged through the onboard Leica Microsystems software (LAS-X). A fluorescence confocal microscope (Leica SP5 Confocal, Leica Microsystems) was used to capture 3D images of different planes of the syncytiotrophoblast layer, and images were automatically mosaic-merged, max Z-projected, or compiled into a 3D model through the onboard Leica Microsystems software (LAS-X).

4.3.9. Viability Assays:

Live/Dead® Viability Staining: For assessing cell viability on a live or dead basis, a commercially available cell viability assay kit (LIVE/DEAD® Viability/Cytotoxicity Kit, Invitrogen) was used. Briefly, calcein AM and ethidium homodimer-1 were combined at 1:2000

(2 μM, live cell stain) and 1:500 (4 μM, dead cell stain) dilutions, respectively, in serum-free media for each Live/Dead assay of a given cell type. Cell cultures were incubated with this combined staining solution for up to 30 minutes in cell culture incubator conditions (37 °C, 5% CO2) to ensure adequate permeation. Cell cultures were rinsed with fresh media to remove extra staining solution and then imaged using a fluorescence microscope (Leica DMI 6000B, Leica Microsystems), with green and red cell coloration for live and dead cells, respectively.

Cell Proliferation Kit II (XTT) Viability Assay: It is challenging to separate the live/dead populations in 3D culture systems with multiple cell types in coculture. In this scenario, a commercially available colorimetric cell viability assay kit (CyQUANT XTT Cell Viability Assay, Invitrogen) was used. This assay uses a two-part system involving an electron coupling agent, where mitochondrial enzymes of healthy cells convert the normally yellow XTT dye is converted to an orange-colored compound called formazan. As this can only happen in live cells, we can assess gross cell viability of a complex coculture system over time by colorimetric assay without lysing the cells for analysis. Briefly, fresh XTT working solution created by mixing 5 mLs of XTT labeling reagent with 0.1 mL of the electron coupling reagent to obtain a clear solution. The XTT working solution was added to the maternal and fetal compartments at a final concentration of 0.3 mg/mL, after which supernatant samples from both sides were collected every 15 minutes for 3 hours to measure the spectrophotometrical absorbance of the samples using a microplate reader (Tecan Infinite 200 Pro, Tecan). The wavelength to measure the absorbance of the formazan product is between 450 – 500 nm utilizing ELISA filters, with a reference wavelength of more than 650 nm.

4.3.11. Barrier Integrity Assays:

Fluorescein Isothiocyanate-Dextran (FITC Dextran): 1000 μg/mL FITC Dextran in STB media was added to maternal compartment, and then allowed to equilibrate for 30 minutes. Fetal compartment samples were collected and then analyzed using a microplate reader (Tecan Infinite 200 Pro, Tecan) at an excitation of 490 nm and emission of 520 nm. Studies were conducted both on-chip as well as bare acellular membranes as a control.

Sodium Fluorescein Permeability: Sodium fluorescein salt (Sigma-Aldrich) was utilized as a fluorescent tracer. Given its small molecular weight of 376.3 g/mol and similar size to sucrose (342.3 g/mol), it has found usage as a small molecule probe for blood brain barrier transport studies[204] and can adequately represent a 'worst case scenario' of unwanted molecular transport through a barrier. Here, we added sodium fluorescein solution at a final concentration of 40 ng/mL to the maternal compartment and let it equilibrate for 30 minutes. Fetal compartment samples were collected and analyzed via a microplate reader (Tecan Infinite 200 Pro, Tecan) at an excitation of 485 nm and an emission of 528 nm. Studies were conducted both on-chip as well as bare acellular membranes as a control.

Glucose Transport: Physiological rates of glucose transfer measured in *ex vivo* human placenta ranges from 26.5 – 38.3%[205]. Glucose transport in the human placenta is an active process, mediated primarily by GLUT1 receptors of the GLUT family within the placental membrane[206]. The STB media and the EGM media used for the maternal and fetal compartments respectively have their own glucose as part of their composition Maternal and fetal concentrations of glucose in the media were measured to be approximately 300 mg/dL and 100 mg/dL, respectively. Glucose samples from the fetal compartment were sampled at appropriate time points, and then analyzed using a commercially available glucose reader (GlucCELL

Glucose Monitoring System, Chemglass Life Sciences). Studies were conducted both on-chip as well as bare acellular membranes as a control.

4.4. Results

4.4.1. Design and Fabrication of the 3D Placenta-on-a-Chip

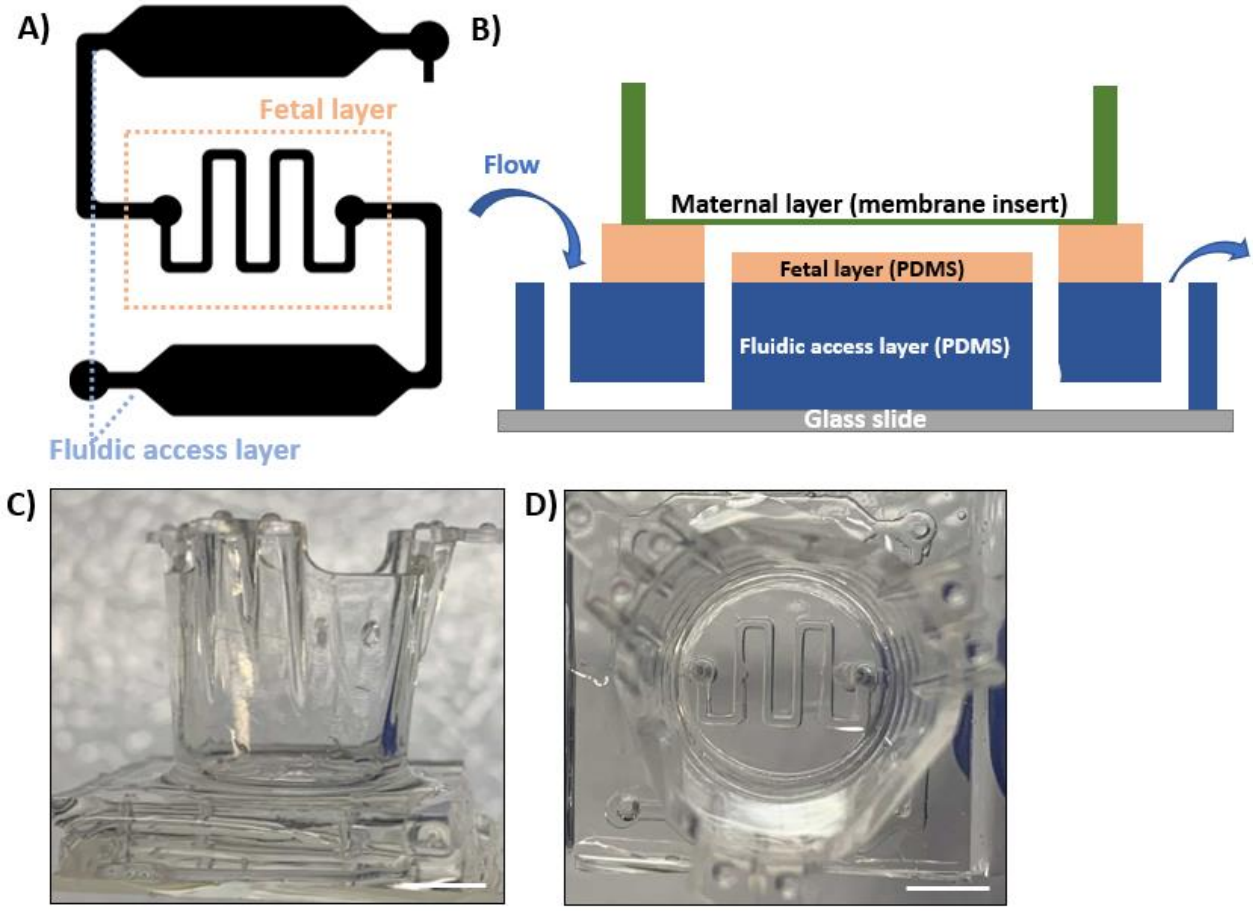

Figure 4.2: Schematic and photographic representations of the microfluidic device

A) Top-down Computer-Aided-Design (CAD) file of the fluidic access and fetal layers. B) Cross-sectional view of the fluidic and fetal access layers stacked vertically on top of one another, with the membrane insert and media retaining cup on the very top. The glass slide forms the base, with the fluidic access layer atop it, providing a way to interface with the channels without inverting the device. Atop the access layer is the fetal layer, and then subsequently the maternal layer composed of a cell culture membrane insert and its media retainment wall. C, D) Cross-sectional and top-down photographs of the microfluidic device. Scale bars = 5 mm.

The placenta-on-a-chip microfluidic device is a 'hybrid' open/closed microfluidic device, where a vertically stacked arrangement of traditional PDMS microchannels is bonded to a cell culture membrane insert (Figure 4.2B). This creates a system where the top compartment is 'open' to atmosphere thus providing facile access to the fabricator for complex handling, and the bottom compartment below the cell culture membrane insert is 'closed,' allowing for sealed perfusion. Microfluidic channel master molds and PDMS devices were fabricated as described previously[72].

A fetal 'capillary' channel was designed via computer aided design software (AutoCAD, AutoDesk), with a designed cross-sectional dimension of 0.5 x 0.5 mm (Figure 4.2A). The shape of the fetal channel was chosen to be a single serpentine length, to minimize adverse bubble events in branching parallel networks, with a total length of approximately 40 mm, giving a length-to-width ratio of approximately 80:1. A secondary layer, termed the 'fluidic access layer' was then created, designed to precisely match the inlet/outlet ports of the fetal channel in the Z-direction when aligned below it, with widened structures in the fluidic access layer functioning as additional media reservoir volume to extend time between media exchanges (Figure 4.2A). These two layers were bonded first to each other, and then to a glass slide base.

Afterwards, a cell culture membrane insert and its associated media retainment wall was then bonded atop the fetal layer, with the membrane effectively forming the 'ceiling' to the fetal compartment and the 'floor' to the maternal compartment simultaneously (Figure 4.2C, D). The cell culture membrane used in this study is a commercially available synthetic membrane composed of an optically clear microporous polyethylene terephthalate, with 0.4 micron track-etched pores at a density of 2E6 per square cm. This membrane is bioinert, topologically flat, and

can be functionalized for optimizing cell culture and hydrogel attachment. This completes the assembly of the placenta-on-a-chip and enables the culturing of live cells.

15.4.2. Cell Culture Optimization

There are three cell types present in this system: placental-derived stromal fibroblasts (PDSFs) and human trophoblast stem cells (hTSCs) for the maternal compartment, and human umbilical vein endothelial cells (HUVECs) for the fetal compartment. All three are human-sourced, and the PDSFs and hTSCS are primary-derived from donated placenta tissue explants, making them the ideal physiologically relevant choice for this model. However, before initiating co-culture, we first had to optimize cell culturing conditions within the device. To better recapitulate the 3D structure of the placental membrane, we encapsulated PDSFs within a gelatin methacryloyl (GelMA) hydrogel bioink, and optimized the stiffness at which the PDSFs seemed to best grow, proliferate, and exhibit their characteristic elongated fibroblastic morphology (Figure 4.3). Using DLP 3D printing, we varied the exposure time of incident light of fixed intensity against the photopolymerizable bioink, modifying the bulk stiffness of the gel and thus PDSFs behavior. By exploring a range of stiffnesses, from as low as ~1.5 kPa to as high as ~30 kPa, we were able to assess not only the PDSFs' viability as a function of stiffness, but also visually assess their morphology as a function of that same stiffness. Based on these assessments, the optimal GelMA stiffness for supporting PDSFs was found to be in the regime of ~18 kPa, which was utilized going forward. The compressive moduli of the hydrogels was measured via micro-mechanical testing (Microsquisher, Cell Scale), as described previously[201].

Once the stiffness for the GelMA-encapsulated PDSF layer in the maternal compartment was set, we similarly assessed hTSC viability and morphology as a function of GelMA stiffness. We explored the same ranges of stiffnesses, with particular focus on validating whether the

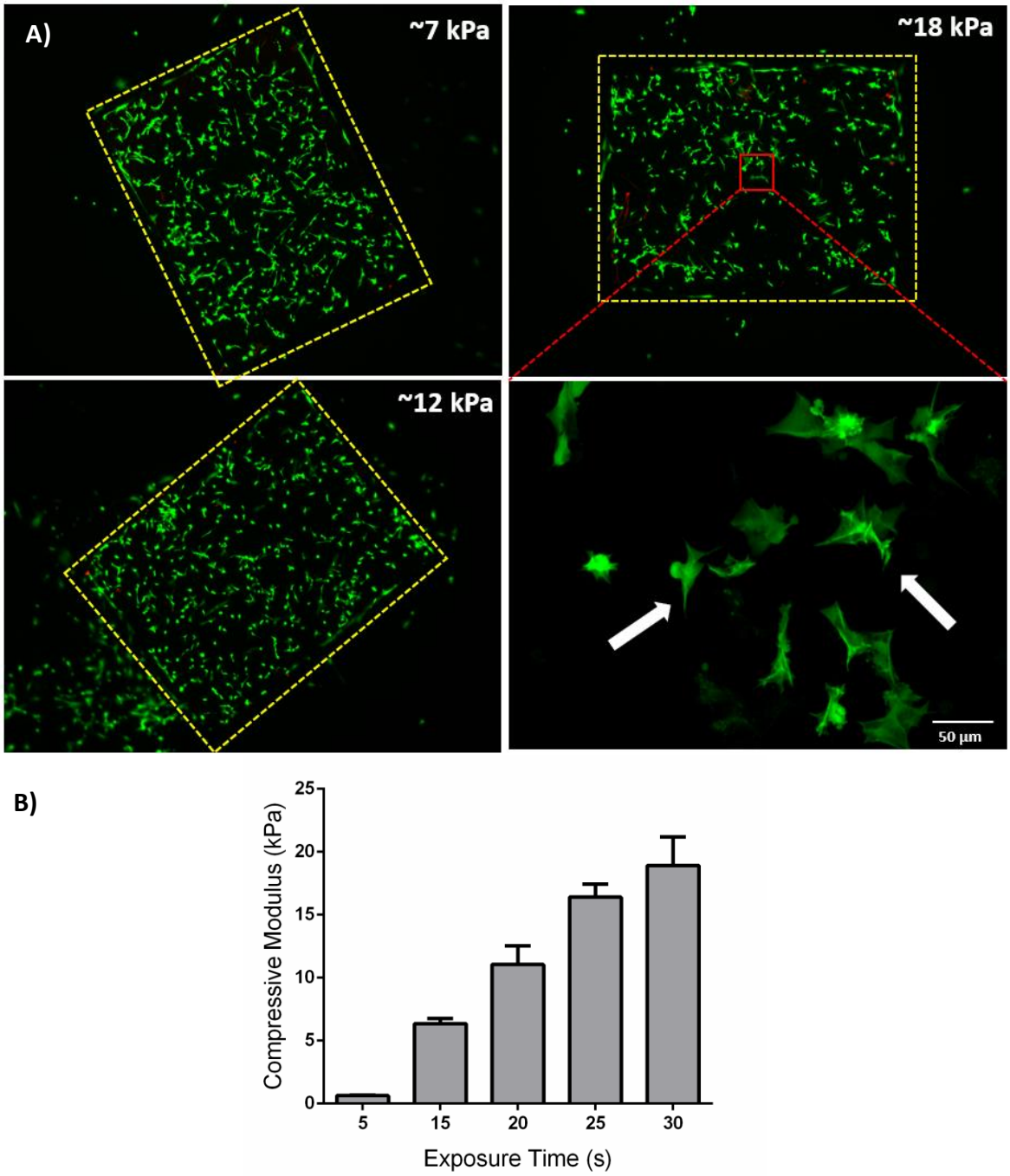

Figure 4.3: Placental-derived stromal fibroblast stiffness optimization in GelMA scaffolds

A) PDSFs were encapsulated at a cell density of 75,000 cells/mL in a 7.5% GelMA, 0.6% LAP bioink solution, and DLP 3D bioprinted as a rectangular slab of 125 μm thickness. Exposure time was varied to impart different stiffnesses to the slabs. Live/Dead imaging was taken of the cells over the course of seven days, and visually-assessed for optimal morphology. Images show Live/Dead at Day 7, while the lower right inset shows confocal microscopy of PDSFs in the ~18 kPa condition, with white arrows denoting the desired morphology. B) Compressive modulus of hydrogels as a function of DLP exposure time and fixed light intensity.

~18 kPa condition would promote optimal hTSC growth on its surface. Figure 4.4 shows hTSCs grown on DLP 3D printed GelMA scaffolds of the same dynamic stiffness range, where Live/Dead viability staining and fluorescence imaging were used to validate hTSC growth. GelMA of all stiffnesses were able to well-support hTSC viability, and we also validated that the chosen ~18 kPa stiffness for PDSF encapsulation was also functional for morphology.

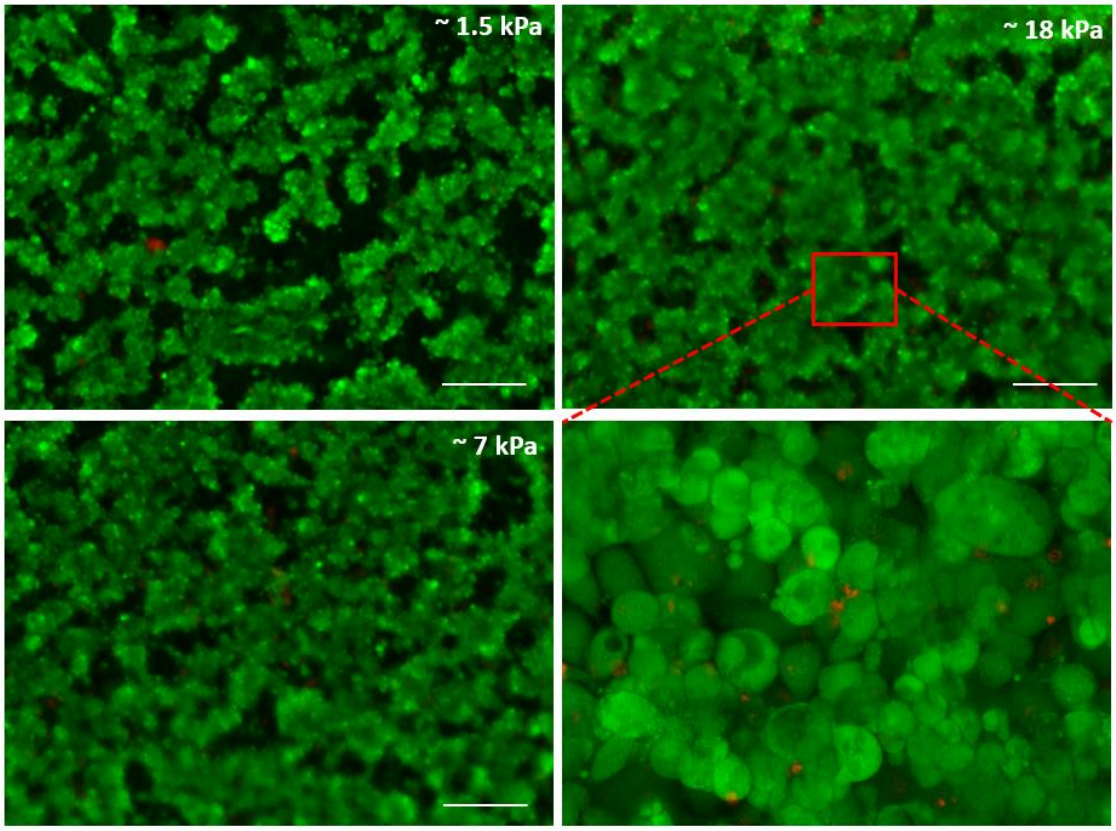

Figure 4.4: Human trophoblast stem cell stiffness optimization on GelMA scaffolds

hTSCs were seeded at a density of 300,000 cells/mL atop of DLP 3D printed GelMA scaffolds of varying stiffness. Live/Dead imaging was taken over seven days, and visually-assessed for optimal morphology. Images show Live/Dead at Day 7, while the lower right inset shows confocal microscopy of the hTSCs with high cell density and dense intercellular junctions.

The high cell density and associated intercellular junctions are critically important, as they form the basis of the placenta's barrier integrity. During the course of gestation, the placenta undergoes many structural changes, of which is the syncytialization (or aggregated cell fusion) of

the cytotrophoblasts on the maternal side of the chorionic villi in the placenta into a large, multi-nucleated barrier called the syncytiotrophoblast[207]. This change in structure is a critical feature of barrier portion of the placenta and is considered a necessary recapitulation in any *in vitro* placenta system[193]. The induction of syncytialization can be achieved through the addition of a compound called forskolin, which increases intracellular levels of cyclic adenosine monophosphate (cAMP) in BeWo b30 clone lines, and can be used to induce syncytialization of trophoblasts in model placenta systems[208]. We used forskolin-containing media to induce syncytialization in our system, as seen in Figure 4.5.

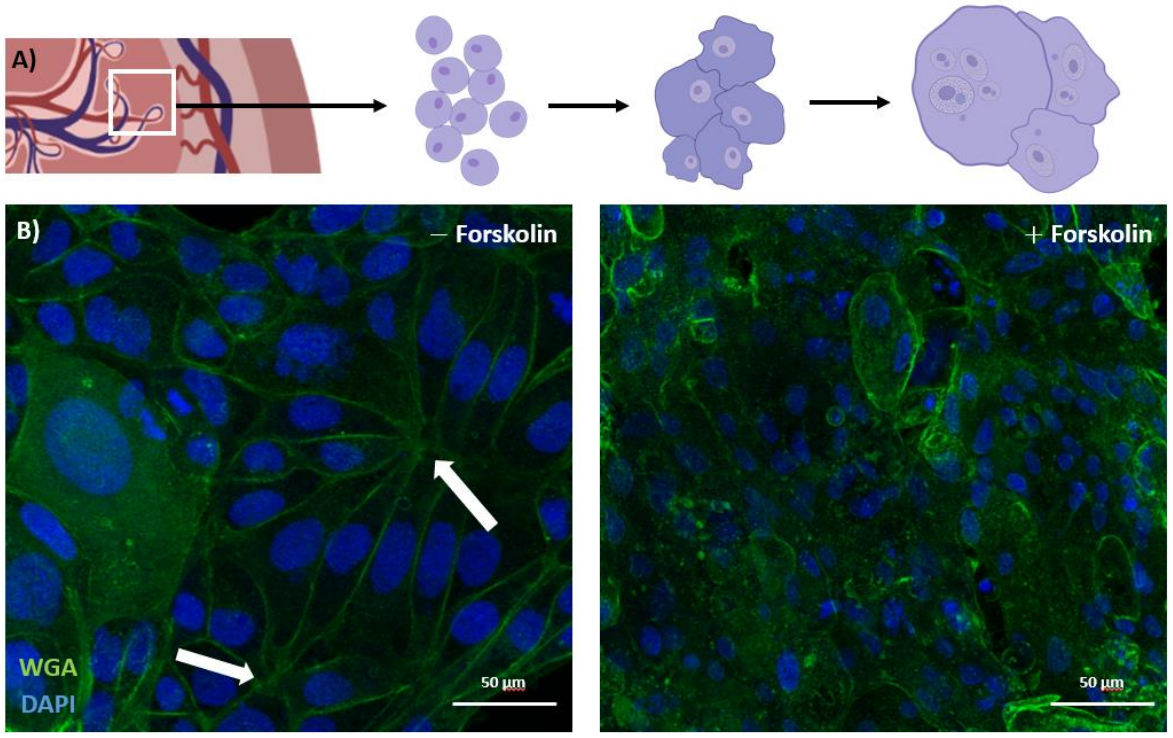

Figure 4.5: Syncytialization of cytotrophoblasts into syncytiotrophoblast.

A) Schematic depiction of the syncytialization process, where individual cytotrophoblasts aggregate, fuse, and give way to large, multinucleated structures with few intercellular junctions, thus forming the basis of the placental barrier. B) Confocal microscopy images of hTSCs stained with wheat germ agglutinin (WGA) and DAPI for cellular membrane and nuclear staining, respectively. Left image shows the presence of mono-nucleated cells with a high density of intracellular junctions (white arrows). Right image shows cells incubated with forskolin-containing media at 72 hours, showing a significant increase in individual cell area and multinucleated cells.

4.4.3. Tri-coculture Assembly and Perfusion

The assembly of the full tri-coculture device was carefully managed step-by-step (Figure 4.6). With all microfluidic devices completed, we incubate the maternal and fetal compartments with bovine plasma-derived fibronectin and collagen-I to promote cell and bioink adhesion to the membrane. Additionally, all three cell lines are brought up to reach maximum confluency along staggered expansion timelines. We first start with DLP 3D bioprinting of the GelMA-encapsulated PDSFs. 75,000 PDSFs are encapsulated within a small volume of 7.5% GelMA + 0.6% LAP bioink solution, and carefully spread onto the membrane insert 'floor' of the maternal compartment. PDMS spacers are used to constrain this volume, after which the UV light of the DLP 3D printer is used to polymerize the bioink into place. Careful removal of the PDMS spacers allows the GelMA-encapsulated PDSFs to remain adhered to the membrane surface.

Next, we seed HUVECs along the fetal compartment interior at a density of 10E6 cells/mL, carefully inverting the microfluidic device in an incubator environment for no more than 1 hour to promote HUVEC attachment to the underside of the membrane as well as prevent adverse evaporation of media in the maternal compartment. After this inversion, the device is placed upright, with fresh media replaced into the maternal compartment. This system is then left to static culture for three days, to give the PDSFs and HUVECs time to rest and proliferate. hTSCs are seeded on the third day, with additional fibronectin used to coat the maternal chamber the day before to promote cellular adhesion. At the same time, perfusion is begun on the HUVEC cells in the fetal compartment, using a peristaltic pump delivering media at a flow rate of 3.5 uL/min for three days. The next day, forskolin is added to the maternal compartment to promote syncytialization, giving the hTSCs in the maternal compartment time to become a

syncytiotrophoblast barrier. After the third day of perfusion, the tri-coculture system is ready for imaging, viability, and barrier assays.

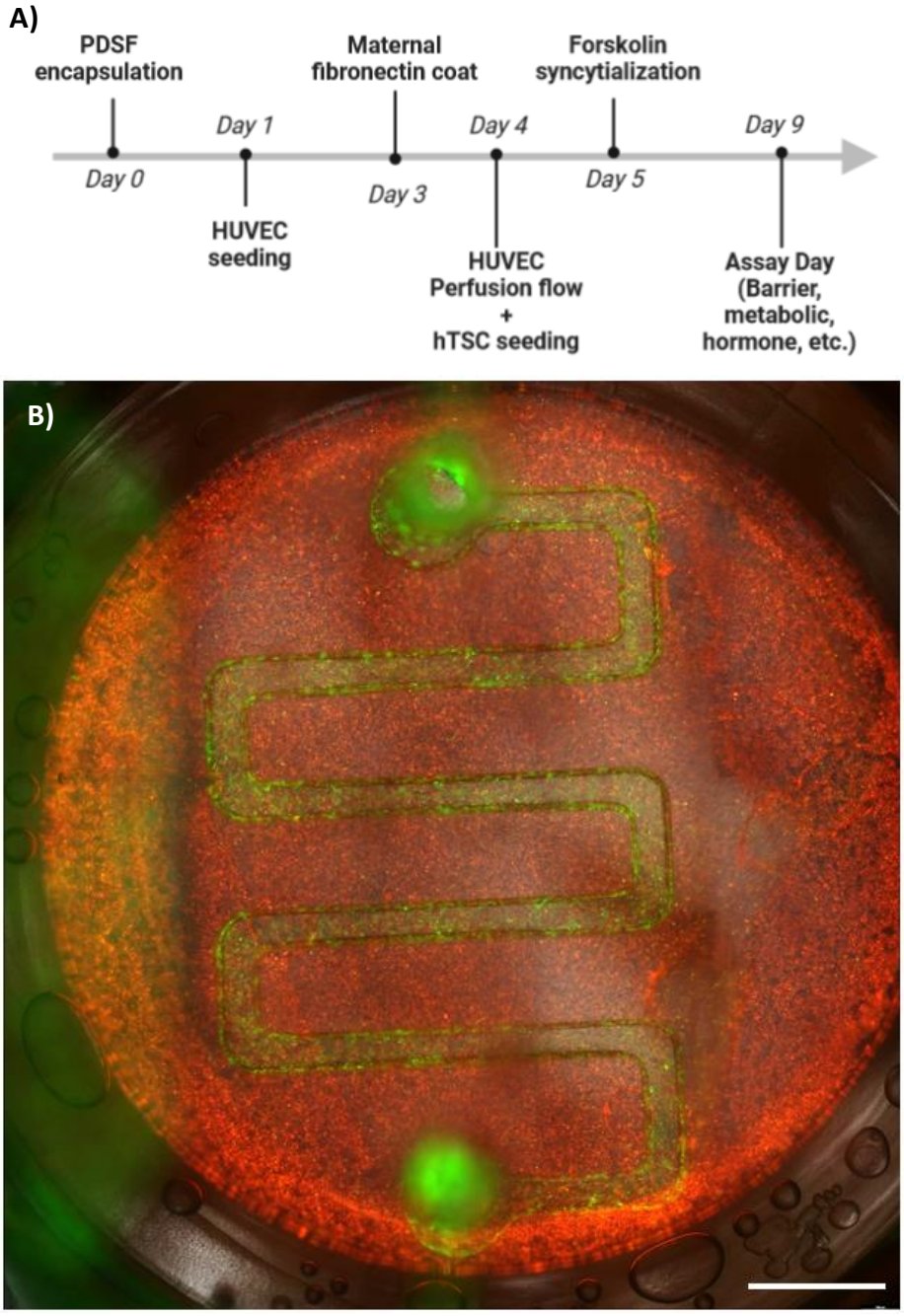

Figure 4.6: Experimental timeline and composite fluorescence image of full tri-coculture

A) Timeline schematic of the major steps in the experimental timeline for assembling the tri-coculture model. B) Composited fluorescence image at 5x tile scan stitch of completed tri-coculture model on Day 2 of perfusion culture. Coloration: HUVECs in green, PDSFs in yellow, and hTSCs in red. Scale bar is 2.5 mm.

We validated HUVEC viability through Live/Dead staining (Figure 4.7A), with images taken every day of static culture. Insets for each image show a slight increase in the presence of dead cells over the three days of static culture, but the vast majority of HUVECs were still alive at the end of the three days. Additionally, we tracked HUVEC morphology as a function of circularity and cell area when exposed to perfusion. Figure 4.7B shows HUVECs present in a previous prototype of channel geometry, where on Day 0 immediately post-seeding the HUVECs had a round, highly circular morphology indicating seeding stress. After one day, they began to relax, showing increased cell area as they begun to flatten out, but otherwise took on the standard 'cobblestone' morphology seen in static culture of HUVECs. After one day of perfusion culture, the HUVECs began to take on a more elongated, striated appearance as they responded to the shear forces present in the microchannel. Image analysis of the cells in the microchannels show that by Day 2, the circularity of the HUVECs markedly decreases, while the cell area correspondingly increases, matching the qualitative observation of the cells' morphology.

4.4.5. Viability and Barrier Integrity Assays

After the three days of perfusion culture and syncytialization of the maternal compartment, we conducted additional viability and barrier integrity assays. Due to the presence of three different cell types coculturing in the same system, we needed a way to asses cell viability in an aggregate manner, as it is challenging to separate one type of dead cell from another. Instead, we chose to utilize a relative colorimetric cell viability assay, the CyQUANT Cell Proliferation Kit XTT Assay (Invitrogen), which utilizes a yellow dye that can only be metabolized living mitochondria into a detectable orange product. By culturing the tric-oculture system with the XTT assay reagents over time, we could sample both the maternal and fetal compartments and thus measure the viability of the cells in aggregate (Figure 4.8A).

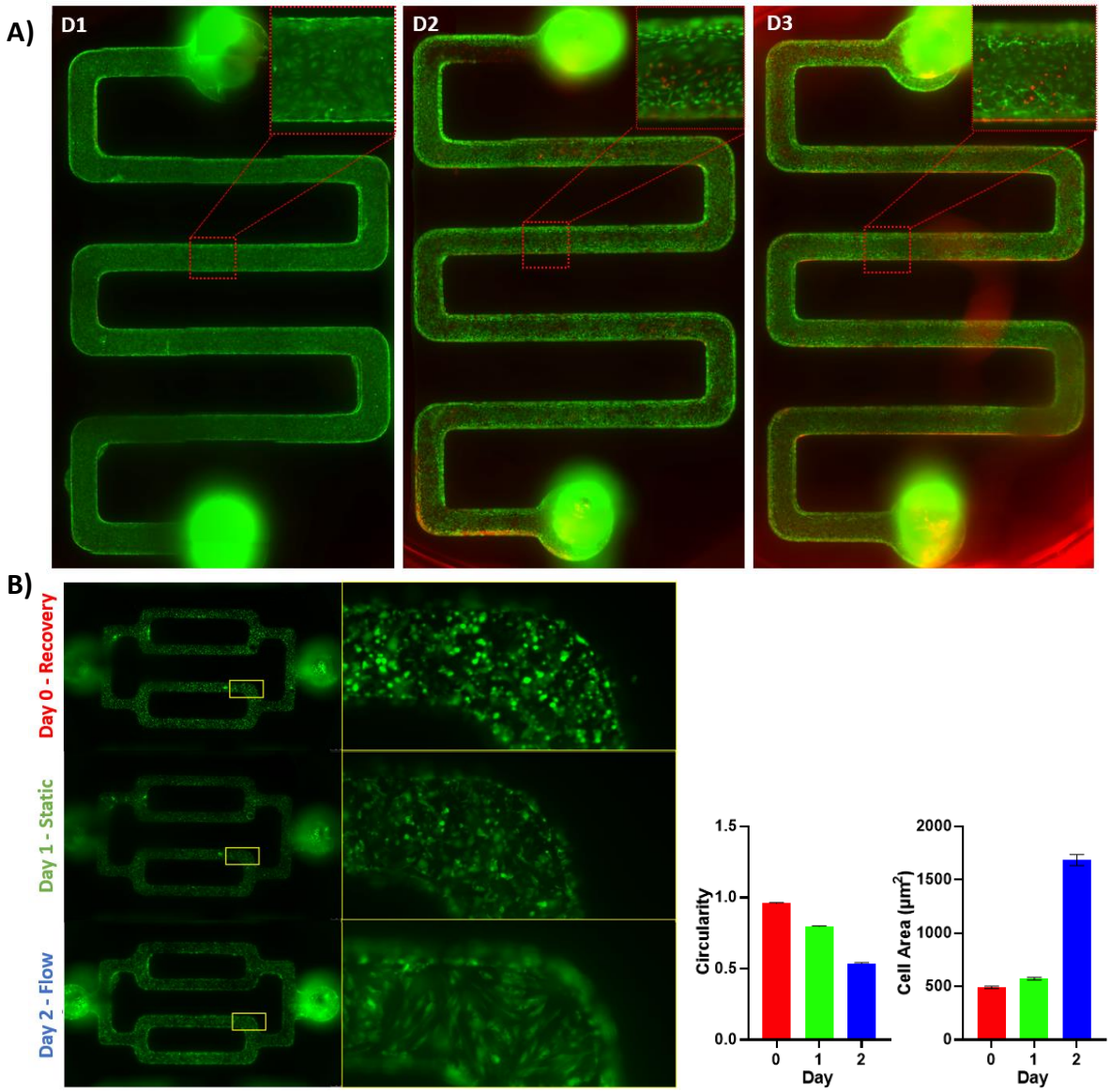

Figure 4.7: HUVEC static and perfusion culture.

A) HUVECs were maintained in static culture for three days, with Live/Dead staining assays done over that same period to assess viability. By Day 3, cellular viability still remains high. B) Analysis of HUVECs in microchannels, where a quantifiable difference in both cell circularity and cell area occurs after changing the culture conditions from static to flow. Over time, cell circularity decreases, while cell area increases.

Sodium fluorescein (Na-F) salt was used as a fluorescent tracer – its small molecular weight makes it an ideal candidate for testing barrier integrity, and can adequately represent a 'worst case scenario' in unwanted molecular transport through a membrane, and has even been

used in blood brain barrier studies as the 'smallest' penetrating molecule[204]. Na-F was input into the maternal compartment, and fetal compartment samples were collected (Figure 4.8B). In the full tri-coculture model, Na-F had lower fetal concentration compared to that of the 'blank' acellular model, and was sustained over time, indicating the barrier's fidelity against small molecule penetration.

While Na-F is an example of passive diffusion through an otherwise agnostic membrane, glucose transport is an active process, handled primarily by the GLUT1 receptor of the GLUT family in the placenta. Utilizing the native glucose concentrations present in the media for both the maternal and fetal compartments of our model, we measured glucose concentration in the fetal side as a function of time across a variety of model types and controls, including standard static acellular cell culture inserts (Figure 4.9A) and full tri-coculture perfusion (Figure 4.9B), with several variations in between, such as GelMA scaffolds with or without encapsulated PDSFs, and with or without seeded hTSCs. Results show that the blank acellular membranes functioned most like passive diffusion, with increasing fetal glucose content over time. In the cellularized conditions across both static and perfused models, the fetal glucose concentration decreased over time, which was an anomalous result, as we expected glucose concentration to at least increase slowly over time. The current hypothesis is that either the cellularized conditions completely block the passage of glucose, in which case HUVEC natural glucose consumption will inevitably deplete the total available glucose in the system, or the rate of glucose transport through the membrane is lower than that of the HUVEC's natural glucose consumption. Future studies will improve on this study design to deconvolve these effects.

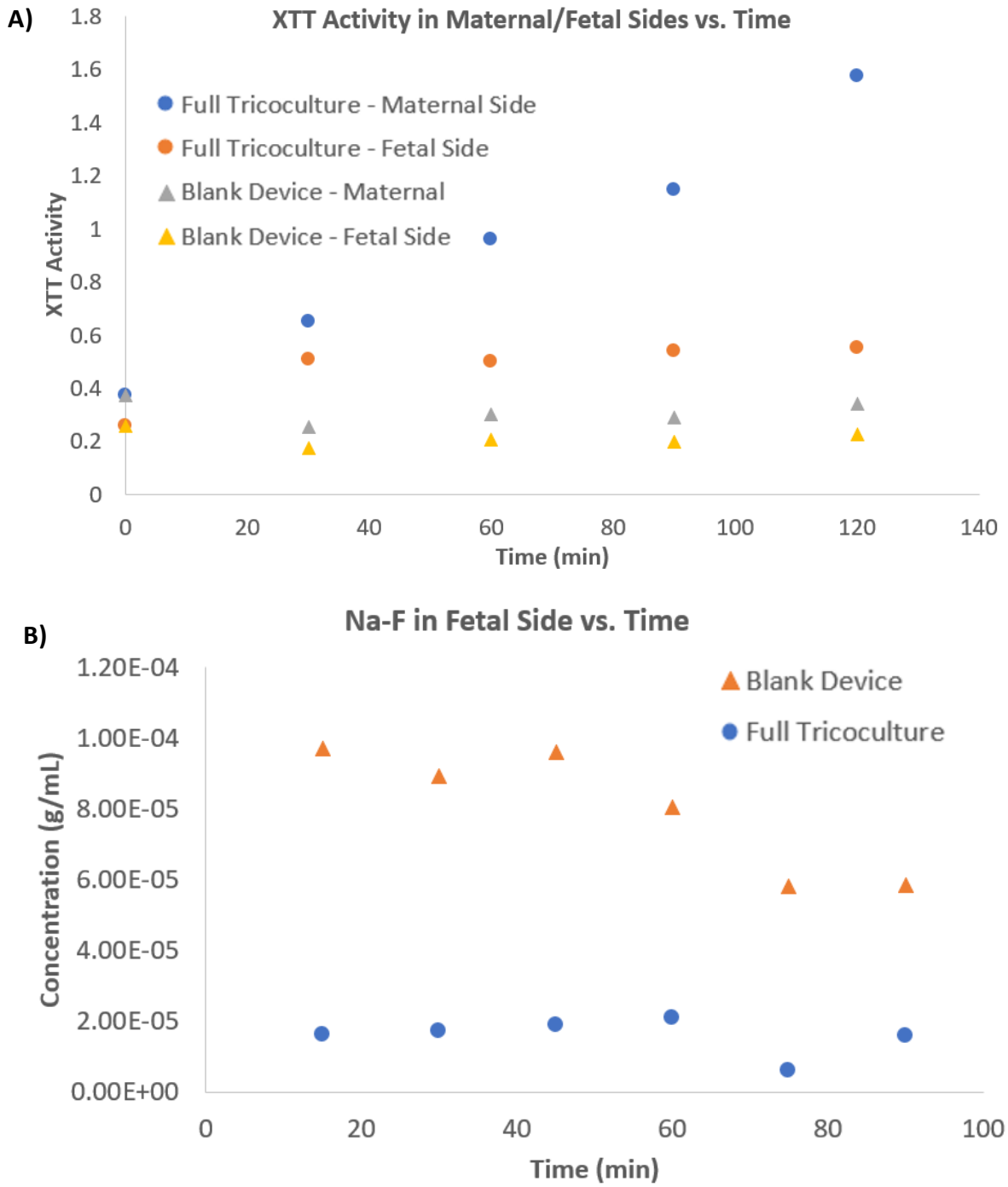

Figure 4.8: XTT Cell Viability and Na-F fluorescent molecule barrier integrity assay.

A) XTT cell viability confirms both a baseline and increase over time of XTT activity in the full tri-coculture model over 'blank' acellular devices. B) Sodium fluorescein (Na-F) penetration of the full tri-coculture model was lower than that of the 'blank' acellular devices and was sustained at low levels over time, indicating an intact barrier.

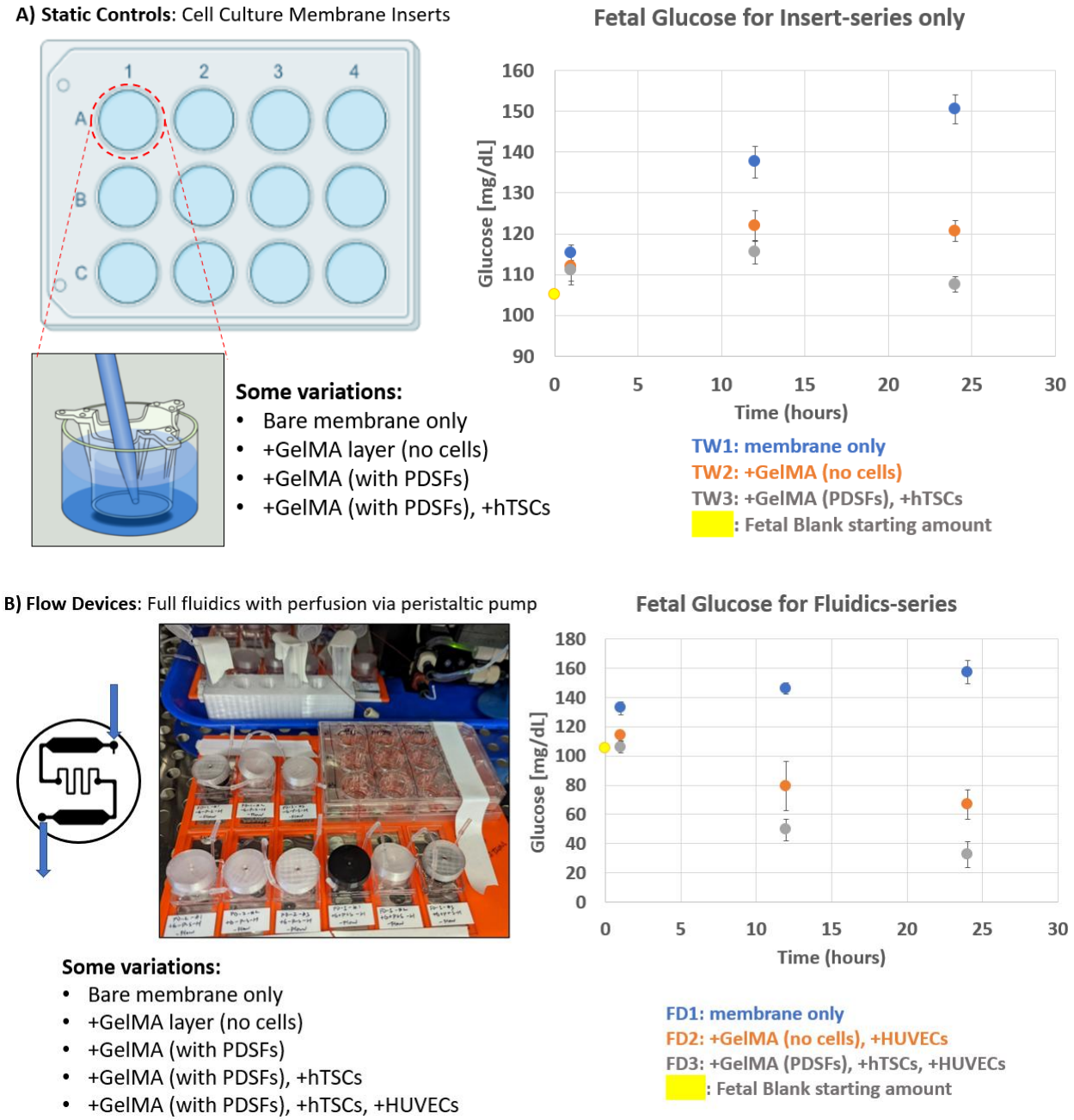

Figure 4.9: Static and perfusion assays for glucose transport.

A) Static testing done on standard cell culture inserts; right side shows fetal glucose over time for three different conditions of the cell culture insert (membrane only, with GelMA but no cells, and with GelMA with cells). Fetal glucose increases over time in all acellular conditions, but cellularized conditions show decrease in glucose. B) Perfusion testing of the same conditions, with similar results – fetal glucose increases over time in acellular conditions, but any cellularized conditions show decrease in fetal glucose concentration over time.

4.5. Conclusions and Future Outlook

In summary, we have developed a biomimetic, microfluidic, tri-coculture 3D transport model that aims to create an *in vitro*, physiologically relevant human placenta, utilizing two different primary tissue-derived placenta cells as part of the maternal compartment, and a human endothelial line for the fetal compartment. The open top of the microfluidic device enabled multi-component fabrication of the maternal layers: a 2D layer of hTSCs atop a stiffness-optimized 3D scaffold of encapsulated PDSFs, with a closed fetal compartment for perfusion flow. We demonstrated through cell viability testing that the device can fully sustain a tri-coculture system for multiple days, is perfusable, and satisfies a key component for *in vitro* placenta models: a syncytialized layer of trophoblasts which forms the tight barrier necessary for proper placental function. We validated the barrier formation with microscopy, as well as performed several molecular transport studies, including FITC-Dextran, sodium fluorescein, and glucose.

This work is still in progress at the time of this writing. Future studies will include additional barrier integrity studies, including: the hormone insulin, a natural molecule to test in conjunction with glucose, as well as the antibodies immunoglobulin G and M (IgG and IgM, respectively), to be tested via enzyme-linked immunosorbent assay (ELISA). IgG antibodies are capable of crossing the placenta during fetal circulation, as mediated by FcRn expressed in the syncytiotrophoblast cells, but IgM does not[209] – the presence of IgM in an actual human fetus would be indicative of infection, but in the *in vitro* model would be a good test of barrier integrity. This work, once completed, will have significant implications for the creation and advancement of highly physiologically relevant *in vitro* models for reproductive health.

4.6. Acknowledgements

Chapter 4, in full, includes material currently being prepared for submission for publication under the working title, “Human Placenta-on-a-Chip: a biomimetic microfluidic 3D transport model.” Hwang, Henry H.; Tekkatte, Chandana; Lindsay-Hewett, Scott; Yu, Claire; Ma, Xuanyi; Farah, Omar; Parast, Mana M.; Laurent, Louise C.; Chen, Shaochen. *In preparation.* The dissertation author is a co-primary investigator and co-author of this ongoing work.

CHAPTER 5: CONCLUSIONS

5.1. Summary

DLP-based 3D printing has garnered significant interest in recent years as a fast, versatile, and highly capable biofabrication platform. The work presented in this dissertation showcases several different applications of digital light processing (DLP)-based 3D printing in the context of microphysiological systems and tissue engineering. With light-based 3D printing systems, many of the limitations associated with extrusion-based 3D printing, such as limited feature resolution, shear forces affecting cell viability, and speed of printing, become mitigated. The availability of biomaterial choices, the high resolution, and the increase in speed of printing thus enable a great deal of flexibility in their use for biofabrication, whether it be direct bioprinting of cellularized scaffolds in microfluidic devices, as a platform for high throughput 3D tissue scaffold production, or as a tool for the creation of complex microfluidic microphysiological systems.

5.1.1. 3D-Printing of Functional Biomedical Microdevices via Light- and Extrusion-based Approaches

In Chapter 1, we explored the various modalities of 3D printing that can be used in the context of fabrication functional biomedical microdevices. Extrusion-based systems have several fundamental limitations that come about as a direct result of their mode of operation – hydrogels and other biological materials such as cells must be physically extruded through narrow apertures. This constrains material selection to those with proper rheological characteristics (to maintain sufficient shape post-extrusion), as well as limiting cell viability as the desired feature size decreases, as shear forces can negatively affect cell viability as they squeeze through narrow apertures. By contrast, light-based 3D bioprinting systems can escape the use of apertures

altogether by use of optical elements projecting and focusing light into an aqueous, photopolymerizable bioink. This enables greater selection of materials and the tuning of their properties compared to extrusion-based systems. Additionally, depending on the nature of the light-based system in question, such as digital light projection (DLP)-based systems, there can be marked increases in the speed and efficiency of the biofabrication of 3D tissue scaffolds, an important consideration when dealing with living materials with short lifetimes.

5.1.2. Direct 3D-Printing of Cell-laden Constructs in Microfluidic Architectures

In Chapter 2, we explored the use of DLP-3D printing as a platform for the construction of 3D microfluidic devices, showcasing the creation of a Variable Height Mixer (VHM) that has topologically distinct and varied rectangular columns that arise semi-randomly from the microfluidic device. This topological setup, compared to smooth channels, creates alternating narrow and widening zones that increase the lamellation and chaotic advection of the distinctive streamlines of laminar flow conditions, enabling enhanced mixing efficiency within small physical footprints. Notably, slower flow rates paired with increasingly complex topologies had better mixing efficiencies compared to faster flow rates paired with smoother topologies, a potentially significant path for preserving cell viability when doing on-chip mixing of live cells. Finally, we demonstrated the non-contact nature of DLP-based 3D printing to print both acellular and cellularized scaffolds of user-defined arbitrary shapes inside the already completed microfluidic device, which would be a challenge for extrusion-based printing systems that would have to navigate their extrusion apertures past a microfluidic device's closed ceiling.

5.1.3. High Throughput Direct 3D Bioprinting in Multiwell Plates

In Chapter 3, we explored the use DLP-3D printing in a high-throughput way, with the motivation being the high cost, time, and energy resources associated with validating compounds

in the pharmaceutical research pipeline. 2D cell culture monolayers are highly repeatable but lack physiological relevance. Animal models are highly physiologically-relevant but still have limitations due to differences in their biology compared to humans. While recent developments in tissue culturing technology have enabled 3D organoids, spheroids, and other tissue scaffolds to be constructed out of multiple cell types, there are limitations associated with throughput and microarchitectural fidelity in mimicking the native physiology they are trying to emulate. By modifying our DLP 3D bioprinter, we enabled high-throughput *in situ* 3D bioprinting of complex tissue scaffolds in standard well plate formats, which we believe is a significant step forward towards the use of humanized 3D tissue scaffolds as a replacement for animal model testing.

5.1.4. Human Placenta-on-a-Chip: a Biomimetic Microfluidic 3D Transport Model

In Chapter 4, we explored the fabrication and characterization of a novel 3D microphysiological system that emulates a human placenta in a microfluidic device. *In vitro* models for tissue systems represent a controllable, standardized, and repeatable method for doing research and validation where it would otherwise be inaccurate, challenging, or ethically dubious to assess in live animal or human subjects. This is especially true for the human placenta, where *ex vivo* perfusions and *in vivo* animals lack both controllability and relevance to the human condition. Existing microphysiological systems for recapitulating the placenta follow a common theme of closed bicameral systems with only one cell type each for the maternal and fetal sides, with the maternal side usually represented by an immortalized cell line derived from carcinogenic cells. We aimed to address these limitations with a hybrid 'open/closed' microfluidic device, where the maternal side is open to the atmosphere to enable DLP bioprinting of a 3D bioink layer encapsulating human-sourced primary placental-derived stromal fibroblasts with human-sourced primary trophoblast stem cells seeded atop, thus forming a dual-

component maternal side. The fetal side uses primary-derived human umbilical vein endothelial cells and was perfused using a peristaltic pump. We validated the tri-coculture system's viability and barrier integrity, although these studies are still ongoing at the time of this writing.

A limitation with this study is that since the maternal side is open to atmosphere, evaporation effects are significant, and perfusion is difficult. Although we modeled the maternal side as 'static' with respect to the flow rate the fetal side experiences for this study, there is ongoing work to incorporate a fluidically-sealable 'ceiling' to the maternal compartment to mitigate these issues.

5.2. Future Outlooks

The field of tissue engineering, as well as 3D printing's role in it, has advanced significantly over the past decade alone - it feels as if every year that novel and exciting small molecules, therapies, technologies, and techniques are invented. However, the human body is a complex biological machine, one made up of tens of trillions of precisely-arranged cells of numerous types[210]. Successfully recapitulating their composition, structure, and function is an ongoing task in tissue engineering, one that 3D printing may have significant potential for in the future. Some areas that will require continued active investigation are the: 1) Vascularization Problem, 2) Cell Sourcing and Density Problem, and 3) Multi-material and Resolution Problem.

5.2.1. The Vascularization Problem

Native tissue and organ systems are highly vascularized – every unit volume of tissue is close enough to a branch of the circulatory system such that oxygen, nutrient, and waste exchange can occur at their interfaces. If there were no such vascularization or circulatory systems present in an organism, biological processes would be reliant on diffusion for transport, which is critically limited to around 200 – 300 μm on average[211], which has negative

implications for the ability to biofabricate thicker tissues. While there are efforts to utilize biofabrication in directly creating hollow vasculature in otherwise cell-laden geometries, extrusion-based 3D printing efforts have poor resolution or require additional post-processing steps that can hamper overall cell viability, and light-based 3D printing efforts must deal with over-photopolymerizing hollow void spaces and poor resolution due to light scattering. Effort in this space is ongoing, and of intense interest.

5.2.2. The Cell Density Problem: Sourcing and Resolution

As mentioned previously, the human body is composed of tens of trillions of cells[210]. As such, any tissue engineering attempt to repair, maintain, or even replace, the structure and/or function of an existing volume of tissue require prodigious amounts of cells. Native human tissues typically have cell densities on the order of 1 – 3 billion cells/mL. Scaling the necessary cell culture technologies to incorporate the billions of cells necessary will be critical, not just because of the raw numbers of cells needed for minimum physiological function but also to mitigate the inevitable cell viability issues that will arise during the acts preparation, biofabrication, and eventual implantation. Additionally, attempting to DLP 3D bioprint such high densities of cells will inevitably incur light scattering, degrading biofabrication resolution when small feature sizes will be critical to accurately recapitulating physiological features.

5.2.3. The Multi-Material Problem

Native human tissues are not monoliths – even within a singular organ or tissue group, disparate tissue types are closely co-localized and often interweave together in close proximity. DLP-based 3D bioprinting utilizes primarily liquids as the base substrate for biofabrication. As liquids generally take on the shape of their container, precise control of liquids in the open-vat configurations typical to DLP-based 3D printing is challenging. Multi-material 3D printing

involves laborious, time-consuming, and/or resource intensive switching of different materials within a single voxel of space, with those requirements increasing severely with the number and complexity of needed materials. This becomes more complicated when living cells are considered, as their viability suffers dramatically when outside optimal cell culture conditions, and as such there are many engineering controls to consider when attempting multi-material 3D bioprinting.

5.3 Personal Final Thoughts

Whenever I am asked about the 'ultimate goal' of tissue engineering by friends, family, and others, the discussion usually tends to center around whether we are be able to 3D bioprint replacement body tissues/parts/organs/limbs for when we inevitably need them due to defects, time, and/or damage. I earnestly hope that such a thing will be possible within my lifetime! There is still a bit of a proverbial quantum leap to be made in tissue engineering technology, and we will have to wait patiently for the wheels of scientific progress to turn. Scientific innovation takes time, but I hold a great deal of optimism for the collective power of humankind.

In a way, it reminds me of my own personal journey with completing this doctorate degree. In my opinion, this whole PhD process has been a *marathon*, not a sprint. The pace of research can sometimes feel slow and arduous, punctuated by bursts of inspiration/success here and there, but otherwise I believe that this journey teaches not only knowledge and methodology, but also a great deal about perseverance, grit, and the willingness to keep going when confronted with failure.

REFERENCES

1. Liaw, C.-Y. & Guvendiren, M. Current and emerging applications of 3D printing in medicine. *Biofabrication* **9**, 024102 (2017).
2. Melchels, F. P. W., Feijen, J. & Grijpma, D. W. A review on stereolithography and its applications in biomedical engineering. *Biomaterials* **31**, 6121–6130 (2010).
3. Gross, B. C., Erkal, J. L., Lockwood, S. Y., Chen, C. & Spence, D. M. Evaluation of 3D printing and its potential impact on biotechnology and the chemical sciences. *Anal. Chem.* **86**, 3240–3253 (2014).
4. O'Donnell, J., Kim, M. & Yoon, H.-S. A Review on Electromechanical Devices Fabricated by Additive Manufacturing. *J. Manuf. Sci. Eng.* **139**, 010801 (2016).
5. Bhattacharjee, N., Urrios, A., Kang, S. & Folch, A. The upcoming 3D-printing revolution in microfluidics. *Lab Chip* **16**, 1720–1742 (2016).
6. Billiet, T., Vandenhaute, M., Schelfhout, J., Van Vlierberghe, S. & Dubruel, P. A review of trends and limitations in hydrogel-rapid prototyping for tissue engineering. *Biomaterials* vol. 33 6020–6041 Preprint at https://doi.org/10.1016/j.biomaterials.2012.04.050 (2012).
7. Novakova-Marcincinova, L. & Kuric, I. Basic and Advanced Materials for Fused Deposition Modeling Rapid Prototyping Technology. *Manuf Ind Eng* **11**, 1338–6549 (2012).
8. Chia, H. N. & Wu, B. M. Recent advances in 3D printing of biomaterials. *J. Biol. Eng.* **9**, 4 (2015).
9. Hull, C. W. Apparatus for production of three-dimensional objects by stereolithography. *US Pat. 4575330* 1–16 (1986) doi:10.1145/634067.634234.
10. Sun, H. B. & Kawata, S. Two-photon photopolymerization and 3D lithographic microfabrication. *Advances in Polymer Science* vol. 170 169–273 Preprint at https://doi.org/10.1007/b94405 (2004).
11. Kaur, M. & Srivastava, A. K. Photopolymerization: a Review. *J. Macromol. Sci. Part C Polym. Rev.* **42**, 481–512 (2002).
12. Shirazi, S. F. S., Gharehkhani, S., Mehrali, M., Yarmand, H., Metselaar, H. S. C., Adib Kadri, N. & Osman, N. A. A. A review on powder-based additive manufacturing for tissue engineering: selective laser sintering and inkjet 3D printing. *Sci. Technol. Adv. Mater.* **16**, 033502 (2015).
13. Stratakis, E., Ranella, A., Farsari, M. & Fotakis, C. Laser-based micro/nanoengineering for biological applications. *Progress in Quantum Electronics* vol. 33 127–163 Preprint at https://doi.org/10.1016/j.pquantelec.2009.06.001 (2009).
14. Lu, Y., Mapili, G., Suhali, G., Chen, S. & Roy, K. A digital micro-mirror device-based system for the microfabrication of complex, spatially patterned tissue engineering scaffolds. *J. Biomed. Mater. Res. - Part A* **77**, 396–405 (2006).
15. A. Bertsch, S. Zissi, J. Y. Jézéquel, S. Corbel, J. C. A. Microstereophotolithography using a liquid crystal display as dynamic mask-generator. *Microsyst. Technol.* **3**, 42–47 (1997).

16. Bertsch, A., Lorenz, H. & Renaud, P. 3D microfabrication by combining microstereolithography and thick resist UV lithography. *Sens. Actuators Phys.* **73**, 14–23 (1999).

17. Beluze, L., Bertsch, A. & Renaud, P. Microstereolithography: a new process to build complex 3D objects. *Des. Test Microfabr. Mems Moems Pts 1 2* **3680**, 808–817 (1999).

18. Sun, C., Fang, N., Wu, D. M. & Zhang, X. Projection micro-stereolithography using digital micro-mirror dynamic mask. *Sens. Actuators Phys.* **121**, 113–120 (2005).

19. Tumbleston, J. R., Shirvanyants, D., Ermoshkin, N., Janusziewicz, R., Johnson, A. R., Kelly, D., Chen, K., Pinschmidt, R., Rolland, J. P., Ermoshkin, A., Samulski, E. T. & DeSimone, J. M. Continuous liquid interface production of 3D objects. *Science* **347**, 1349–1352 (2015).

20. Purcell, E. M. Life at low Reynolds number. *Am.J.Phys.* **45**, 1–11 (1977).

21. Tottori, S., Zhang, L., Qiu, F., Krawczyk, K. K., Franco-Obregõn, A. & Nelson, B. J. Magnetic helical micromachines: Fabrication, controlled swimming, and cargo transport. *Adv. Mater.* **24**, 811–816 (2012).

22. Qiu, T., Lee, T.-C., Mark, A. G., Morozov, K. I., Münster, R., Mierka, O., Turek, S., Leshansky, A. M. & Fischer, P. Swimming by reciprocal motion at low Reynolds number. *Nat. Commun.* **5**, 5119 (2014).

23. Cvetkovic, C., Raman, R., Chan, V., Williams, B. J., Tolish, M., Bajaj, P., Sakar, M. S., Asada, H. H., Saif, M. T. A. & Bashir, R. Three-dimensionally printed biological machines powered by skeletal muscle. *Pnas* **111**, 10125–10130 (2014).

24. Zhu, W., Li, J., Leong, Y. J., Rozen, I., Qu, X., Dong, R., Wu, Z., Gao, W., Chung, P. H., Wang, J. & Chen, S. 3D-Printed Artificial Microfish. *Adv. Mater.* **27**, 4411–4417 (2015).

25. Alomari, M., Mohamed, F. H., Basit, A. W. & Gaisford, S. Personalised dosing: Printing a dose of one's own medicine. *Int. J. Pharm.* **494**, 568–577 (2015).

26. Scoutaris, N., Alexander, M. R., Gellert, P. R. & Roberts, C. J. Inkjet printing as a novel medicine formulation technique. *J. Controlled Release* **156**, 179–185 (2011).

27. Goyanes, A., Buanz, A. B. M., Hatton, G. B., Gaisford, S. & Basit, A. W. 3D printing of modified-release aminosalicylate (4-ASA and 5-ASA) tablets. *Eur. J. Pharm. Biopharm.* **89**, 157–162 (2015).

28. Skowyra, J., Pietrzak, K. & Alhnan, M. A. Fabrication of extended-release patient-tailored prednisolone tablets via fused deposition modelling (FDM) 3D printing. *Eur. J. Pharm. Sci.* **68**, 11–17 (2015).

29. Khaled, S. A., Burley, J. C., Alexander, M. R., Yang, J. & Roberts, C. J. 3D printing of five-in-one dose combination polypill with defined immediate and sustained release profiles. *J. Controlled Release* **217**, 308–314 (2015).

30. Goyanes, A., Wang, J., Buanz, A., Mart??nez-Pacheco, R., Telford, R., Gaisford, S. & Basit, A. W. 3D Printing of Medicines: Engineering Novel Oral Devices with Unique Design and Drug Release Characteristics. *Mol. Pharm.* **12**, 4077–4084 (2015).

31. Khaled, S. A., Burley, J. C., Alexander, M. R. & Roberts, C. J. Desktop 3D printing of controlled release pharmaceutical bilayer tablets. *Int. J. Pharm.* **461**, 105–111 (2014).

32. Prasad, L. K. & Smyth, H. 3D Printing technologies for drug delivery: a review. *Drug Dev. Ind. Pharm.* **42**, 1019–1031 (2016).

33. Goole, J. & Amighi, K. 3D printing in pharmaceutics: A new tool for designing customized drug delivery systems. *Int. J. Pharm.* **499**, 376–394 (2016).

34. Ursan, I. D., Chiu, L. & Pierce, A. Three-dimensional drug printing: A structured review. *J. Am. Pharm. Assoc.* **53**, 136–144 (2013).

35. Alhnan, M. A., Okwuosa, T. C., Sadia, M., Wan, K. W., Ahmed, W. & Arafat, B. Emergence of 3D Printed Dosage Forms: Opportunities and Challenges. *Pharmaceutical Research* vol. 33 1817–1832 Preprint at https://doi.org/10.1007/s11095-016-1933-1 (2016).

36. Apercia Pharmaceuticals Company. Spritam. https://www.spritam.com/ (2015).

37. Rouphael, N. G., Paine, M., Mosley, R., Henry, S., McAllister, D. V, Kalluri, H., Pewin, W., Frew, P. M., Yu, T., Thornburg, N. J., Kabbani, S., Lai, L., Vassilieva, E. V, Skountzou, I., Compans, R. W., Mulligan, M. J., Prausnitz, M. R., Beck, A., Edupuganti, S., Heeke, S., Kelley, C. & Nesheim, W. The safety, immunogenicity, and acceptability of inactivated influenza vaccine delivered by microneedle patch (TIV-MNP 2015): a randomised, partly blinded, placebo-controlled, phase 1 trial. *The Lancet* **390**, 649–658 (2017).

38. Kim, Y. C., Park, J. H. & Prausnitz, M. R. Microneedles for drug and vaccine delivery. *Advanced Drug Delivery Reviews* vol. 64 1547–1568 Preprint at https://doi.org/10.1016/j.addr.2012.04.005 (2012).

39. Hamilton, J. G. Fear of injections in young adults: Prevalence and associations. *Am. J. Trop. Med. Hyg.* **41**, 341–344 (1995).

40. Hamilton, J. G. Needle phobia: a neglected diagnosis. *J. Fam. Pract.* **41**, 169–75 (1995).

41. Indermun, S., Luttge, R., Choonara, Y. E., Kumar, P., Du Toit, L. C., Modi, G. & Pillay, V. Current advances in the fabrication of microneedles for transdermal delivery. *Journal of Controlled Release* vol. 185 130–138 Preprint at https://doi.org/10.1016/j.jconrel.2014.04.052 (2014).

42. Li, J., Zeng, M., Shan, H. & Tong, C. Microneedle Patches as Drug and Vaccine Delivery Platform. *Curr. Med. Chem.* **24**, 2413–2422 (2017).

43. Ovsianikov, A., Chichkov, B., Mente, P., Monteiro-Riviere, N. A., Doraiswamy, A. & Narayan, R. J. Two photon polymerization of polymer-ceramic hybrid materials for transdermal drug delivery. *Int. J. Appl. Ceram. Technol.* **4**, 22–29 (2007).

44. Kochhar, J. S., Zou, S., Chan, S. Y. & Kang, L. Protein encapsulation in polymeric microneedles by photolithography. *Int. J. Nanomedicine* **7**, 3143–3154 (2012).

45. Lim, S. H., Ng, J. Y. & Kang, L. Three-dimensional printing of a microneedle array on personalized curved surfaces for dual-pronged treatment of trigger finger. *Biofabrication* **9**, 015010 (2017).

46. Mohanty, S. P. & Koucianos, E. Biosensors: A tutorial review. *IEEE Potentials* vol. 25 35–40 Preprint at https://doi.org/10.1109/MP.2006.1649009 (2006).

47. Zhang, Y., Ge, S. & Yu, J. Chemical and biochemical analysis on lab-on-a-chip devices fabricated using three-dimensional printing. *TrAC - Trends in Analytical Chemistry* vol. 85 166–180 Preprint at https://doi.org/10.1016/j.trac.2016.09.008 (2016).

48. Bishop, G. W., Satterwhite-Warden, J. E., Kadimisetty, K. & Rusling, J. F. 3D-printed bioanalytical devices. *Nanotechnology* **27**, 284002 (2016).

49. Gowers, S. A. N., Curto, V. F., Seneci, C. A., Wang, C., Anastasova, S., Vadgama, P., Yang, G. Z. & Boutelle, M. G. 3D Printed Microfluidic Device with Integrated Biosensors for Online Analysis of Subcutaneous Human Microdialysate. *Anal. Chem.* **87**, 7763–7770 (2015).

50. Boehm, R. D., Jaipan, P., Yang, K.-H., Stewart, T. N. & Narayan, R. J. Microstereolithography-fabricated microneedles for fluid sampling of histamine-contaminated tuna. *Int. J. Bioprinting* **2**, 1–9 (2016).

51. Roda, A., Guardigli, M., Calabria, D., Calabretta, M. M., Cevenini, L. & Michelini, E. A 3D-printed device for a smartphone-based chemiluminescence biosensor for lactate in oral fluid and sweat. *The Analyst* **139**, 6494–6501 (2014).

52. Cevenini, L., Calabretta, M. M., Tarantino, G., Michelini, E. & Roda, A. Smartphone-interfaced 3D printed toxicity biosensor integrating bioluminescent 'sentinel cells'. *Sens. Actuators B Chem.* **225**, 249–257 (2016).

53. Miller, P. R., Gittard, S. D., Edwards, T. L., Lopez, D. A. M., Xiao, X., Wheeler, D. R., Monteiro-Riviere, N. A., Brozik, S. M., Polsky, R. & Narayan, R. J. Integrated carbon fiber electrodes within hollow polymer microneedles for transdermal electrochemical sensing. *Biomicrofluidics* **5**, 013415 (2011).

54. Kim, K., Zhu, W., Qu, X., Aaronson, C., McCall, W. R., Chen, S. & Sirbuly, D. J. 3D optical printing of piezoelectric nanoparticle-polymer composite materials. *ACS Nano* **8**, 9799–9806 (2014).

55. Gou, M., Qu, X., Zhu, W., Xiang, M., Yang, J., Zhang, K., Wei, Y. & Chen, S. Bio-inspired detoxification using 3D-printed hydrogel nanocomposites. *Nat. Commun.* **5**, 3774 (2014).

56. Mandon, C. A., Blum, L. J. & Marquette, C. A. Adding Biomolecular Recognition Capability to 3D Printed Objects. *Anal. Chem.* **88**, 10767–10772 (2016).

57. Stassi, S., Fantino, E., Calmo, R., Chiappone, A., Gillono, M., Scaiola, D., Pirri, C. F., Ricciardi, C., Chiado, A. & Roppolo, I. Polymeric 3D Printed Functional Microcantilevers for Biosensing Applications. *ACS Appl. Mater. Interfaces* **9**, 19193–19201 (2017).

58. Spivey, E. C., Xhemalce, B., Shear, J. B. & Finkelstein, I. J. 3D-printed microfluidic microdissector for high-throughput studies of cellular aging. *Anal. Chem.* **86**, 7406–7412 (2014).

59. Au, A. K., Lee, W. & Folch, A. Mail-order microfluidics: evaluation of stereolithography for the production of microfluidic devices. *Lab. Chip* **14**, 1294–301 (2014).

60. Ho, C. M. B., Ng, S. H., Li, K. H. H. & Yoon, Y.-J. 3D printed microfluidics for biological applications. *Lab Chip* **15**, 3627–3637 (2015).

61. Waheed, S., Cabot, J. M., Macdonald, N. P., Lewis, T., Guijt, R. M., Paull, B. & Breadmore, M. C. 3D printed microfluidic devices: enablers and barriers. *Lab Chip* **16**, 1993–2013 (2016).

62. Yazdi, A. A., Popma, A., Wong, W., Nguyen, T., Pan, Y. & Xu, J. 3D printing: an emerging tool for novel microfluidics and lab-on-a-chip applications. *Microfluid. Nanofluidics* **20**, 1–18 (2016).

63. Morgan, A. J. L., San Jose, L. H., Jamieson, W. D., Wymant, J. M., Song, B., Stephens, P., Barrow, D. A. & Castell, O. K. Simple and versatile 3D printed microfluidics using fused filament fabrication. *PLoS ONE* **11**, e0152023 (2016).

64. Bishop, G. W., Satterwhite, J. E., Bhakta, S., Kadimisetty, K., Gillette, K. M., Chen, E. & Rusling, J. F. 3D-Printed fluidic devices for nanoparticle preparation and flow-injection amperometry using integrated prussian blue nanoparticle-modified electrodes. *Anal. Chem.* **87**, 5437–5443 (2015).

65. Dolomite. Dolomite Microfluidics. *Http://Www.Dolomite-Microfluidics.Com/* Dolomite Microfluidics http://www.dolomite-microfluidics.com/.

66. Au, A. K., Huynh, W., Horowitz, L. F. & Folch, A. 3D-Printed Microfluidics. *Angew. Chem. - Int. Ed.* **55**, 3862–3881 (2016).

67. Erkal, J. L., Selimovic, A., Gross, B. C., Lockwood, S. Y., Walton, E. L., McNamara, S., Martin, R. S. & Spence, D. M. 3D printed microfluidic devices with integrated versatile and reusable electrodes. *Lab. Chip* **14**, 2023–32 (2014).

68. Begolo, S., Zhukov, D. V, Selck, D. a, Li, L. & Ismagilov, R. F. The pumping lid: investigating multi-material 3D printing for equipment-free, programmable generation of positive and negative pressures for microfluidic applications. *Lab. Chip* **14**, 4616–28 (2014).

69. Causier, A., Carret, G., Boutin, C., Berthelot, T. & Berthault, P. 3D-printed system optimizing dissolution of hyperpolarized gaseous species for micro-sized NMR. *Lab Chip* **15**, 2049–2054 (2015).

70. Lim, T. W., Son, Y., Jeong, Y. J., Yang, D.-Y., Kong, H.-J., Lee, K.-S. & Kim, D.-P. Three-dimensionally crossing manifold micro-mixer for fast mixing in a short channel length. *Lab. Chip* **11**, 100–3 (2011).

71. Urrios, A., Parra-Cabrera, C., Bhattacharjee, N., Gonzalez-Suarez, A. M., Rigat-Brugarolas, L. G., Nallapatti, U., Samitier, J., DeForest, C. A., Posas, F., Garcia-Cordero, J. L. & Folch, A. 3D-printing of transparent bio-microfluidic devices in PEG-DA. *Lab Chip* **16**, 2287–2294 (2016).

72. Liu, J., Hwang, H. H., Wang, P., Whang, G. & Chen, S. Direct 3D-printing of cell-laden constructs in microfluidic architectures. *Lab Chip* **16**, 1430–1438 (2016).

73. Rogers, C. I., Qaderi, K., Woolley, A. T. & Nordin, G. P. 3D printed microfluidic devices with integrated valves. *Biomicrofluidics* **9**, 16501 (2015).

74. Bhargava, K. C., Thompson, B., Malmstadt, N., Szuromi, D., Voss, D. F., Brauman, J. I. & Szuromi, P. Discrete elements for 3D microfluidics. *Proc. Natl. Acad. Sci.* **111**, 15013–8 (2014).

75. Sochol, R. D., Sweet, E., Glick, C. C., Venkatesh, S., Avetisyan, A., Ekman, K. F., Raulinaitis, A., Tsai, A., Wienkers, A., Korner, K., Hanson, K., Long, A., Hightower, B. J., Slatton, G., Burnett, D. C., Massey, T. L., Iwai, K., Lee, L. P., Pister, K. S. J. & Lin, L. 3D printed microfluidic circuitry via multijet-based additive manufacturing. *Lab. Chip* **16**, 668–678 (2016).

76. Tsuda, S., Jaffery, H., Doran, D., Hezwani, M., Robbins, P. J., Yoshida, M. & Cronin, L. Customizable 3D printed 'Plug and Play' millifluidic devices for programmable fluidics. *PLoS ONE* **10**, e0141640 (2015).

77. Lee, J. M., Zhang, M. & Yeong, W. Y. Characterization and evaluation of 3D printed microfluidic chip for cell processing. *Microfluid. Nanofluidics* **20**, 1–15 (2016).

78. Macdonald, N. P., Cabot, J. M., Smejkal, P., Guijt, R. M., Paull, B. & Breadmore, M. C. Comparing Microfluidic Performance of Three-Dimensional (3D) Printing Platforms. *Anal. Chem.* **89**, 3858–3866 (2017).

79. Vaezi, M., Seitz, H. & Yang, S. *A review on 3D micro-additive manufacturing technologies. International Journal of Advanced Manufacturing Technology* vol. 67 1721–1754 (Springer London, 2013).

80. Johnson, B. N., Lancaster, K. Z., Hogue, I. B., Meng, F., Kong, Y. L., Enquist, L. W. & McAlpine, M. C. 3D printed nervous system on a chip. *Lab Chip* **16**, 1393–1400 (2016).

81. Hutmacher, D. W., Sittinger, M. & Risbud, M. V. Scaffold-based tissue engineering: Rationale for computer-aided design and solid free-form fabrication systems. *Trends in Biotechnology* vol. 22 354–362 Preprint at https://doi.org/10.1016/j.tibtech.2004.05.005 (2004).

82. Muth, J. T., Vogt, D. M., Truby, R. L., Meng????, Y., Kolesky, D. B., Wood, R. J. & Lewis, J. A. Embedded 3D printing of strain sensors within highly stretchable elastomers. *Adv. Mater.* **26**, 6307–6312 (2014).

83. Zhu, W., Ma, X., Gou, M., Mei, D., Zhang, K. & Chen, S. 3D printing of functional biomaterials for tissue engineering. *Curr. Opin. Biotechnol.* **40**, 103–112 (2016).

84. Atala, S. V. M. & A. 3D Bioprinting of Tissues and Organs. *Nat. Biotechnol.* **32**, 773–785 (2014).

85. Goyanes, A., Buanz, A. B. M., Basit, A. W. & Gaisford, S. Fused-filament 3D printing (3DP) for fabrication of tablets. *Int. J. Pharm.* **476**, 88–92 (2014).

86. Zein, N. N., Hanouneh, I. A., Bishop, P. D., Samaan, M., Eghtesad, B., Quintini, C., Miller, C., Yerian, L. & Klatte, R. Three-dimensional print of a liver for preoperative planning in living donor liver transplantation. *Liver Transpl.* **19**, 1304–1310 (2013).

87. Bin, Z., Baekhoon, S., VuDat, N. & Doyoung, B. 3D printing of high-resolution PLA-based structures by hybrid electrohydrodynamic and fused deposition modeling techniques. *J. Micromechanics Microengineering* **26**, 25015 (2016).

88. Maruo, S., Nakamura, O. & Kawata, S. Three-dimensional microfabrication with two-photon-absorbed photopolymerization. *Opt. Lett.* **22**, 132 (1997).

89. Maruo, S. Development of Functional Devices Using Three-dimensional Micro / nano Stereolithography. *NIPPON GOMU KYOKAISHI* **3**, 382–388 (2014).

90. Kumi, G., Yanez, C. O., Belfield, K. D. & Fourkas, J. T. High-speed multiphoton absorption polymerization: fabrication of microfluidic channels with arbitrary cross-sections and high aspect ratios. *Lab. Chip* **10**, 1057 (2010).

91. Zhang, Y. L., Chen, Q. D., Xia, H. & Sun, H. B. *Designable 3D nanofabrication by femtosecond laser direct writing*. *Nano Today* vol. 5 435–448 (2010).

92. Fang, N., Sun, C. & Zhang, X. Diffusion-limited photopolymerization in scanning micro-stereolithography. *Appl. Phys. Mater. Sci. Process.* **79**, 1839–1842 (2004).

93. Selimis, A., Mironov, V. & Farsari, M. Direct laser writing: Principles and materials for scaffold 3D printing. *Microelectronic Engineering* vol. 132 83–89 Preprint at https://doi.org/10.1016/j.mee.2014.10.001 (2014).

94. Gittard, S. D., Nguyen, A., Obata, K., Koroleva, A., Narayan, R. J. & Chichkov, B. N. Fabrication of microscale medical devices by two-photon polymerization with multiple foci via a spatial light modulator. *Biomed. Opt. Express* **2**, 3167 (2011).

95. Stansbury, J. W. & Idacavage, M. J. 3D printing with polymers: Challenges among expanding options and opportunities. *Dent. Mater.* **32**, 54–64 (2016).

96. Shaffer, S., Yang, K., Vargas, J., Di Prima, M. A. & Voit, W. On reducing anisotropy in 3D printed polymers via ionizing radiation. *Polym. U. K.* **55**, 5969–5979 (2014).

97. McCullough, E. J. & Yadavalli, V. K. Surface modification of fused deposition modeling ABS to enable rapid prototyping of biomedical microdevices. *J. Mater. Process. Technol.* **213**, 947–954 (2013).

98. Stratasys. Objet350-500 Connex3. http://www.stratasys.com/3d-printers/objet-350-500-connex3 (2014).

99. Yap, Y. L., Wang, C., Sing, S. L., Dikshit, V., Yeong, W. Y. & Wei, J. Material jetting additive manufacturing: An experimental study using designed metrological benchmarks. *Precision Engineering* vol. 50 275–285 (2016).

100. Lee, M. P., Cooper, G. J. T., Hinkley, T., Gibson, G. M., Padgett, M. J. & Cronin, L. Development of a 3D printer using scanning projection stereolithography. *Sci. Rep.* **5**, 9875 (2015).

101. Zhang, A. P., Qu, X., Soman, P., Hribar, K. C., Lee, J. W., Chen, S. & He, S. Rapid fabrication of complex 3D extracellular microenvironments by dynamic optical projection stereolithography. *Adv. Mater.* **24**, 4266–4270 (2012).

102. Ali, Md. H., Mir-Nasiri, N. & Ko, W. L. Multi-nozzle extrusion system for 3D printer and its control mechanism. *Int. J. Adv. Manuf. Technol.* **86**, 999–1010 (2016).

103. Jiang, C. Development of a novel two-laser beam stereolithography system. *Rapid Prototyp. J.* **17**, 148–155 (2011).

104. Autodesk Ember. https://ember.autodesk.com/.

105. Tien, J. Microfluidic approaches for engineering vasculature. *Curr. Opin. Chem. Eng.* **3**, 36–41 (2014).

106. Zhu, W., Qu, X., Zhu, J., Ma, X., Patel, S., Liu, J., Wang, P., Lai, C. S. E., Gou, M., Xu, Y., Zhang, K. & Chen, S. Direct 3D bioprinting of prevascularized tissue constructs with complex microarchitecture. *Biomaterials* **124**, 106–115 (2017).

107. Ma, X., Qu, X., Zhu, W., Li, Y.-S., Yuan, S., Zhang, H., Liu, J., Wang, P., Lai, C. S. E., Zanella, F., Feng, G.-S., Sheikh, F., Chien, S. & Chen, S. Deterministically patterned biomimetic human iPSC-derived hepatic model via rapid 3D bioprinting. *Proc. Natl. Acad. Sci.* **113**, 2206–2211 (2016).

108. Kolesky, D. B., Truby, R. L., Gladman, A. S., Busbee, T. A., Homan, K. A. & Lewis, J. A. 3D bioprinting of vascularized, heterogeneous cell-laden tissue constructs. *Adv. Mater.* **26**, 3124–3130 (2014).

109. Kolesky, D. B., Homan, K. A., Skylar-Scott, M. A. & Lewis, J. A. Three-dimensional bioprinting of thick vascularized tissues. *Proc. Natl. Acad. Sci.* **113**, 3179–3184 (2016).

110. Yager, P., Edwards, T., Fu, E., Helton, K., Nelson, K., Tam, M. R. & Weigl, B. H. Microfluidic diagnostic technologies for global public health. *Nature* **442**, 412–8 (2006).

111. Toner, M. & Irimia, D. Blood-on-a-chip. *Annu. Rev. Biomed. Eng.* **7**, 77–103 (2005).

112. Yetisen, A. K., Akram, M. S. & Lowe, C. R. Paper-based microfluidic point-of-care diagnostic devices. *Lab. Chip* **13**, 2210–51 (2013).

113. Whitesides, G. M. The origins and the future of microfluidics. *Nature* **442**, 368–73 (2006).

114. Suh, Y. K. & Kang, S. A review on mixing in microfluidics. *Micromachines* (2010) doi:10.3390/mi1030082.

115. Lee, C.-Y., Chang, C.-L., Wang, Y.-N. & Fu, L.-M. Microfluidic Mixing: A Review. *Int. J. Mol. Sci.* (2011) doi:10.3390/ijms12053263.

116. Park, S.-J., Kim, J. K., Park, J., Chung, S., Chung, C. & Chang, J. K. Rapid three-dimensional passive rotation micromixer using the breakup process. *J. Micromechanics Microengineering* **14**, 6–14 (2004).

117. Liu, R. H., Stremler, M. A., Sharp, K. V., Olsen, M. G., Santiago, J. G., Adrian, R. J., Aref, H. & Beebe, D. J. Passive mixing in a three-dimensional serpentine microchannel. *J. Microelectromechanical Syst.* **9**, 190–197 (2000).

118. Viktorov, V. & Nimafar, M. A novel generation of 3D SAR-based passive micromixer: efficient mixing and low pressure drop at a low Reynolds number. *J. Micromechanics Microengineering* **23**, 055023 (2013).

119. Ho, C. M. B., Ng, S. H. G., Li, K. H. H. & Yoon, Y.-J. 3D Printed Microfluidics for Biological Applications. *Lab Chip* **15**, 3627–3637 (2015).

120. Spivey, E. C., Xhemalce, B., Shear, J. B. & Finkelstein, I. J. 3D-printed microfluidic microdissector for high-throughput studies of cellular aging. *Anal. Chem.* **86**, 7406–12 (2014).

121. Au, A. K., Lee, W. & Folch, A. Mail-order microfluidics: evaluation of stereolithography for the production of microfluidic devices. *Lab. Chip* **14**, 1294–301 (2014).

122. Spivey, E. C., Xhemalce, B., Shear, J. B. & Finkelstein, I. J. 3D-printed microfluidic microdissector for high-throughput studies of cellular aging. *Anal. Chem.* **86**, 7406–12 (2014).

123. Au, A. K., Lee, W. & Folch, A. Mail-order microfluidics: evaluation of stereolithography for the production of microfluidic devices. *Lab. Chip* **14**, 1294–301 (2014).

124. Paydar, O. H., Paredes, C. N., Hwang, Y., Paz, J., Shah, N. B. & Candler, R. N. Characterization of 3D-printed microfluidic chip interconnects with integrated O-rings. *Sens. Actuators Phys.* **205**, 199–203 (2014).

125. Rogers, C. I., Qaderi, K., Woolley, A. T. & Nordin, G. P. 3D printed microfluidic devices with integrated valves. *Biomicrofluidics* **9**, 16501 (2015).

126. Shallan, A. I., Smejkal, P., Corban, M., Guijt, R. M. & Breadmore, M. C. Cost-Effective Three-Dimensional Printing of Visibly Transparent Microchips within Minutes. *Anal. Chem.* **86**, 3124–30 (2014).

127. Lee, K. G., Park, K. J., Seok, S., Shin, S., Kim, D. H., Park, J. Y., Heo, Y. S., Lee, S. J. & Lee, T. J. 3D printed modules for integrated microfluidic devices. *RSC Adv.* (2014) doi:10.1039/C4RA05072J.

128. Saggiomo, V. & Velders, A. H. Simple 3D Printed Scaffold-Removal Method for the Fabrication of Intricate Microfluidic Devices. *Adv. Sci.* **2**, n/a-n/a (2015).

129. Chen, C., Wang, Y., Lockwood, S. Y. & Spence, D. M. 3D-printed fluidic devices enable quantitative evaluation of blood components in modified storage solutions for use in transfusion medicine. *The Analyst* **139**, 3219–26 (2014).

130. Anderson, K. B., Lockwood, S. Y., Martin, R. S. & Spence, D. M. A 3D printed fluidic device that enables integrated features. *Anal. Chem.* **85**, 5622–6 (2013).

131. Kolesky, D. B., Truby, R. L., Gladman, A. S., Busbee, T. A., Homan, K. A. & Lewis, J. A. 3D bioprinting of vascularized, heterogeneous cell-laden tissue constructs. *Adv Mater* **26**, 3124–3130 (2014).

132. Kolesky, D. B., Truby, R. L., Gladman, A. S., Busbee, T. A., Homan, K. A. & Lewis, J. A. 3D bioprinting of vascularized, heterogeneous cell-laden tissue constructs. *Adv Mater* **26**, 3124–3130 (2014).

133. Bhatia, S. N. & Ingber, D. E. Microfluidic organs-on-chips. *Nat Biotech* **32**, 760–772 (2014).

134. Liu, Y., Chen, C., Summers, S., Medawala, W. & Spence, D. M. C-peptide and zinc delivery to erythrocytes requires the presence of albumin: implications in diabetes explored with a 3D-printed fluidic device. *Integr. Biol. Quant. Biosci. Nano Macro* **7**, 534–43 (2015).

135. Lee, K. G., Park, K. J., Seok, S., Shin, S., Kim, D. H., Park, J. Y., Heo, Y. S., Lee, S. J. & Lee, T. J. 3D printed modules for integrated microfluidic devices. *RSC Adv.* **4**, 32876 (2014).

136. Grogan, S. P., Chung, P. H., Soman, P., Chen, P., Lotz, M. K., Chen, S. & D'Lima, D. D. Digital micromirror device projection printing system for meniscus tissue engineering. *Acta Biomater.* **9**, 7218–26 (2013).

137. Lee, J. W., Kim, K.-J., Kang, K. S., Chen, S., Rhie, J.-W. & Cho, D.-W. Development of a bone reconstruction technique using a solid free-form fabrication (SFF)-based drug releasing scaffold and adipose-derived stem cells. *J. Biomed. Mater. Res. A* **101A**, 1865–1875 (2013).

138. Soman, P., Kelber, J. a, Lee, J. W., Wright, T. N., Vecchio, K. S., Klemke, R. L. & Chen, S. Cancer cell migration within 3D layer-by-layer microfabricated photocrosslinked PEG scaffolds with tunable stiffness. *Biomaterials* **33**, 7064–70 (2012).

139. Suri, S., Han, L.-H., Zhang, W., Singh, A., Chen, S. & Schmidt, C. E. Solid freeform fabrication of designer scaffolds of hyaluronic acid for nerve tissue engineering. *Biomed. Microdevices* **13**, 983–93 (2011).

140. Zhang, A. P., Qu, X., Soman, P., Hribar, K. C., Lee, J. W., Chen, S. & He, S. Rapid fabrication of complex 3D extracellular microenvironments by dynamic optical projection stereolithography. *Adv. Mater.* **24**, 4266–4270 (2012).

141. Soman, P., Chung, P. H., Zhang, A. P. & Chen, S. Digital microfabrication of user-defined 3D microstructures in cell-laden hydrogels. *Biotechnology and bioengineering* vol. 110 3038–3047 http://schen.ucsd.edu/lab/papers/90_bit24957.pdf (2013).

142. Qu, X., Zhu, W., Huang, S., Li, Y.-S., Chien, S., Zhang, K. & Chen, S. Relative impact of uniaxial alignment vs. form-induced stress on differentiation of human adipose derived stem cells. *Biomaterials* **34**, 9812–8 (2013).

143. Huang, T. Q., Qu, X., Liu, J. & Chen, S. 3D printing of biomimetic microstructures for cancer cell migration. *Biomed. Microdevices* **16**, 127–132 (2014).

144. Kim, K., Zhu, W., Qu, X., Aaronson, C., McCall, W. R., Chen, S. & Sirbuly, D. J. 3D Optical Printing of Piezoelectric Nanoparticle–Polymer Composite Materials. *ACS Nano* **8**, 9799–9806 (2014).

145. Gou, M., Qu, X., Zhu, W., Xiang, M., Yang, J., Zhang, K., Wei, Y. & Chen, S. Bio-inspired detoxification using 3D-printed hydrogel nanocomposites. *Nat. Commun.* **5**, 3774 (2014).

146. Hribar, K. C., Finlay, D., Ma, X., Qu, X., Ondeck, M. G., Chung, P. H., Zanella, F., Engler, A. J., Sheikh, F., Vuori, K. & Chen, S. C. Nonlinear 3D projection printing of concave hydrogel microstructures for long-term multicellular spheroid and embryoid body culture. *Lab Chip* **15**, 2412–2418 (2015).

147. Zhu, W., Li, J., Leong, Y. J., Rozen, I., Qu, X., Dong, R., Wu, Z., Gao, W., Chung, P. H., Wang, J. & Chen, S. 3D-Printed Artificial Microfish. *Adv. Mater.* **27**, 4411–4417 (2015).

148. Nichol, J. W., Koshy, S. T., Bae, H., Hwang, C. M., Yamanlar, S. & Khademhosseini, A. Cell-laden microengineered gelatin methacrylate hydrogels. *Biomaterials* **31**, 5536–5544 (2010).

149. Fairbanks, B. D., Schwartz, M. P., Bowman, C. N. & Anseth, K. S. Photoinitiated polymerization of PEG-diacrylate with lithium phenyl-2, 4, 6-trimethylbenzoylphosphinate: polymerization rate and cytocompatibility. *Biomaterials* **30**, 6702–6707 (2009).

150. Zhang, A. P., Qu, X., Soman, P., Hribar, K. C., Lee, J. W., Chen, S. & He, S. Rapid fabrication of complex 3D extracellular microenvironments by dynamic optical projection stereolithography. *Adv. Mater. Deerfield Beach Fla* **24**, 4266–70 (2012).

151. Miller, J. S., Stevens, K. R., Yang, M. T., Baker, B. M., Nguyen, D. H., Cohen, D. M., Toro, E., Chen, A. A., Galie, P. A., Yu, X., Chaturvedi, R., Bhatia, S. N. & Chen, C. S. Rapid

casting of patterned vascular networks for perfusable engineered three-dimensional tissues. *Nat Mater* **11**, 768–774 (2012).

152. Hughes, J. P., Rees, S. S., Kalindjian, S. B. & Philpott, K. L. Principles of early drug discovery. *British Journal of Pharmacology* vol. 162 1239–1249 Preprint at https://doi.org/10.1111/j.1476-5381.2010.01127.x (2011).

153. Avorn, J. The $2.6 Billion Pill — Methodologic and Policy Considerations. *N. Engl. J. Med.* **372**, 1877–1879 (2015).

154. Giacomotto, J. & S??galat, L. High-throughput screening and small animal models, where are we? *British Journal of Pharmacology* vol. 160 204–216 Preprint at https://doi.org/10.1111/j.1476-5381.2010.00725.x (2010).

155. Musther, H., Olivares-Morales, A., Hatley, O. J. D., Liu, B. & Rostami Hodjegan, A. Animal versus human oral drug bioavailability: Do they correlate? *Eur. J. Pharm. Sci.* **57**, 280–291 (2014).

156. Langhans, S. A. Three-Dimensional in Vitro Cell Culture Models in Drug Discovery and Drug Repositioning. *Front. Pharmacol.* **9**, (2018).

157. Bhadriraju, K. & Chen, C. S. Engineering cellular microenvironments to improve cell-based drug testing. *Drug Discov. Today* **7**, 612–620 (2002).

158. Verjans, E.-T., Doijen, J., Luyten, W., Landuyt, B. & Schoofs, L. Three-dimensional cell culture models for anticancer drug screening: Worth the effort? *J. Cell. Physiol.* **233**, 2993–3003 (2018).

159. Yildirimer, L., Zhang, Q., Kuang, S., Cheung, C.-W. J., Chu, K. A., He, Y., Yang, M. & Zhao, X. Engineering three-dimensional microenvironments towards *in vitro* disease models of the central nervous system. *Biofabrication* (2019) doi:10.1088/1758-5090/ab17aa.

160. Edmondson, R., Broglie, J. J., Adcock, A. F. & Yang, L. Three-Dimensional Cell Culture Systems and Their Applications in Drug Discovery and Cell-Based Biosensors. *Assay Drug Dev. Technol.* **12**, 207–218 (2014).

161. Kaplowitz, N. Idiosyncratic drug hepatotoxicity. *Nat. Rev. Drug Discov.* **4**, 489–499 (2005).

162. Buschauer, S., Koch, A., Wiggermann, P., Müller, M. & Hellerbrand, C. Hepatocellular carcinoma cells surviving doxorubicin treatment exhibit increased migratory potential and resistance to doxorubicin re-treatment in vitro. *Oncol. Lett.* **15**, 4635–4640 (2018).

163. Takebe, T., Zhang, R.-R., Koike, H., Kimura, M., Yoshizawa, E., Enomura, M., Koike, N., Sekine, K. & Taniguchi, H. Generation of a vascularized and functional human liver from an iPSC-derived organ bud transplant. *Nat. Protoc.* **9**, 396–409 (2014).

164. Si-Tayeb, K., Lemaigre, F. P. & Duncan, S. A. Organogenesis and Development of the Liver. *Dev. Cell* **18**, 175–189 (2010).

165. Yu, C., Ma, X., Zhu, W., Wang, P., Miller, K. L., Stupin, J., Koroleva-Maharajh, A., Hairabedian, A. & Chen, S. Scanningless and continuous 3D bioprinting of human tissues with decellularized extracellular matrix. *Biomaterials* **194**, 1–13 (2019).

166. Liu, J., He, J., Liu, J., Ma, X., Chen, Q., Lawrence, N., Zhu, W., Xu, Y. & Chen, S. Rapid 3D bioprinting of in vitro cardiac tissue models using human embryonic stem cell-derived cardiomyocytes. *Bioprinting* **13**, e00040 (2019).

167. Soman, P., Chung, P. H., Zhang, A. P. & Chen, S. Digital microfabrication of user-defined 3D microstructures in cell-laden hydrogels. *Biotechnol. Bioeng.* **110**, 3038–3047 (2013).

168. Hwang, H. H., Zhu, W., Victorine, G., Lawrence, N. & Chen, S. 3D-Printing of Functional Biomedical Microdevices via Light- and Extrusion-Based Approaches. *Small Methods* **2**, 1700277 (2017).

169. Kang, H. W., Lee, S. J., Ko, I. K., Kengla, C., Yoo, J. J. & Atala, A. A 3D bioprinting system to produce human-scale tissue constructs with structural integrity. *Nat. Biotechnol.* **34**, 312–319 (2016).

170. Zhu, W., Tringale, K. R., Woller, S. A., You, S., Johnson, S., Shen, H., Schimelman, J., Whitney, M., Steinauer, J., Xu, W., Yaksh, T. L., Nguyen, Q. T. & Chen, S. Rapid continuous 3D printing of customizable peripheral nerve guidance conduits. *Mater. Today* (2018) doi:10.1016/j.mattod.2018.04.001.

171. Zhang, A. P., Qu, X., Soman, P., Hribar, K. C., Lee, J. W., Chen, S. & He, S. Rapid Fabrication of Complex 3D Extracellular Microenvironments by Dynamic Optical Projection Stereolithography. *Adv. Mater.* **24**, 4266–4270 (2012).

172. Ma, X., Dewan, S., Liu, J., Tang, M., Miller, K. L., Yu, C., Lawrence, N., McCulloch, A. D. & Chen, S. 3D printed micro-scale force gauge arrays to improve human cardiac tissue maturation and enable high throughput drug testing. *Acta Biomater.* **95**, 319–327 (2019).

173. Kim, J. H., Seol, Y. J., Ko, I. K., Kang, H. W., Lee, Y. K., Yoo, J. J., Atala, A. & Lee, S. J. 3D Bioprinted Human Skeletal Muscle Constructs for Muscle Function Restoration. *Sci. Rep.* **8**, 12307 (2018).

174. Ma, X., Yu, C., Wang, P., Xu, W., Wan, X., Lai, C. S. E., Liu, J., Koroleva-Maharajh, A. & Chen, S. Rapid 3D bioprinting of decellularized extracellular matrix with regionally varied mechanical properties and biomimetic microarchitecture. *Biomaterials* **185**, 310–321 (2018).

175. Koffler, J., Zhu, W., Qu, X., Platoshyn, O., Dulin, J. N., Brock, J., Graham, L., Lu, P., Sakamoto, J., Marsala, M., Chen, S. & Tuszynski, M. H. Biomimetic 3D-printed scaffolds for spinal cord injury repair. *Nat. Med.* 1 (2019) doi:10.1038/s41591-018-0296-z.

176. Grayscale digital light processing 3D printing for highly functionally graded materials | Science Advances. https://advances.sciencemag.org/content/5/5/eaav5790.

177. Tumbleston, J. R., Shirvanyants, D., Ermoshkin, N., Janusziewicz, R., Johnson, A. R., Kelly, D., Chen, K., Pinschmidt, R., Rolland, J. P., Ermoshkin, A., Samulski, E. T. & DeSimone, J. M. Continuous liquid interface production of 3D objects. *Science* **347**, 1349–1352 (2015).

178. Beer, M. P. de, Laan, H. L. van der, Cole, M. A., Whelan, R. J., Burns, M. A. & Scott, T. F. Rapid, continuous additive manufacturing by volumetric polymerization inhibition patterning. *Sci. Adv.* **5**, eaau8723 (2019).

179. Kelly, B. E., Bhattacharya, I., Heidari, H., Shusteff, M., Spadaccini, C. M. & Taylor, H. K. Volumetric additive manufacturing via tomographic reconstruction. *Science* **363**, 1075–1079 (2019).

180. Shusteff, M., Browar, A. E. M., Kelly, B. E., Henriksson, J., Weisgraber, T. H., Panas, R. M., Fang, N. X. & Spadaccini, C. M. One-step volumetric additive manufacturing of complex polymer structures. *Sci. Adv.* **3**, eaao5496 (2017).

181. Rodríguez-Dévora, J. I., Zhang, B., Reyna, D., Shi, Z. & Xu, T. High throughput miniature drug-screening platform using bioprinting technology. *Biofabrication* **4**, 035001 (2012).

182. Xu, F., Celli, J., Rizvi, I., Moon, S., Hasan, T. & Demirci, U. A three-dimensional in vitro ovarian cancer coculture model using a high-throughput cell patterning platform. *Biotechnol. J.* **6**, 204–212 (2011).

183. Guillemot, F., Souquet, A., Catros, S., Guillotin, B., Lopez, J., Faucon, M., Pippenger, B., Bareille, R., Rémy, M., Bellance, S., Chabassier, P., Fricain, J. C. & Amédée, J. High-throughput laser printing of cells and biomaterials for tissue engineering. *Acta Biomater.* **6**, 2494–2500 (2010).

184. Ma, X., Yu, C., Wang, P., Xu, W., Wan, X., Lai, C. S. E., Liu, J., Koroleva-Maharajh, A. & Chen, S. Rapid 3D bioprinting of decellularized extracellular matrix with regionally varied mechanical properties and biomimetic microarchitecture. *Biomaterials* **185**, 310–321 (2018).

185. Ye, N., Qin, J., Liu, X., Shi, W. & Lin, B. Characterizing doxorubicin-induced apoptosis in HepG2 cells using an integrated microfluidic device. *Electrophoresis* **28**, 1146–1153 (2007).

186. Lupertz, R., Watjen, W., Kahl, R. & Chovolou, Y. Dose- and time-dependent effects of doxorubicin on cytotoxicity, cell cycle and apoptotic cell death in human colon cancer cells. *Toxicology* **271**, 115–121 (2010).

187. Mitchell, A. A., Gilboa, S. M., Werler, M. M., Kelley, K. E., Louik, C., Hernández-Díaz, S., & National Birth Defects Prevention Study. Medication use during pregnancy, with particular focus on prescription drugs: 1976-2008. *Am. J. Obstet. Gynecol.* **205**, 51.e1–8 (2011).

188. Zubizarreta, M. E. & Xiao, S. Bioengineering models of female reproduction. *Bio-Des. Manuf.* **3**, 237–251 (2020).

189. Miller, R. K., Genbacev, O., Turner, M. A., Aplin, J. D., Caniggia, I. & Huppertz, B. Human placental explants in culture: Approaches and assessments. *Placenta* **26**, 439–448 (2005).

190. Carter, A. M. Animal Models of Human Placentation – A Review. *Placenta* **28**, S41–S47 (2007).

191. Chen, H.-C. Boyden chamber assay. *Methods Mol. Biol. Clifton NJ* **294**, 15–22 (2005).

192. Blundell, C., Tess, E. R., Schanzer, A. S. R., Coutifaris, C., Su, E. J., Parry, S. & Huh, D. A microphysiological model of the human placental barrier. *Lab. Chip* **16**, 3065–3073 (2016).

193. Blundell, C., Yi, Y.-S., Ma, L., Tess, E. R., Farrell, M. J., Georgescu, A., Aleksunes, L. M. & Huh, D. Placental Drug Transport-on-a-Chip: A Microengineered In Vitro Model of Transporter-Mediated Drug Efflux in the Human Placental Barrier. *Adv. Healthc. Mater.* **7**, 1700786 (2018).

194. Pemathilaka, R. L., Reynolds, D. E. & Hashemi, N. N. Drug transport across the human placenta: review of placenta-on-a-chip and previous approaches. *Interface Focus* **9**, 20190031 (2019).

195. Pemathilaka, R. L., Caplin, J. D., Aykar, S. S., Montazami, R. & Hashemi, N. N. Placenta-on-a-Chip: In Vitro Study of Caffeine Transport across Placental Barrier Using Liquid Chromatography Mass Spectrometry. *Glob. Chall.* **3**, 1800112 (2019).

196. Gonçalves, B. M., Graceli, J. B., da Rocha, P. B., Tilli, H. P., Vieira, E. M., de Sibio, M. T., Peghinelli, V. V., Deprá, I. C., Mathias, L. S., Olímpio, R. M. C., Belik, V. C. & Nogueira, C. R. Placental model as an important tool to study maternal-fetal interface. *Reprod. Toxicol.* **112**, 7–13 (2022).

197. Yin, F., Zhu, Y., Zhang, M., Yu, H., Chen, W. & Qin, J. A 3D human placenta-on-a-chip model to probe nanoparticle exposure at the placental barrier. *Toxicol. In Vitro* **54**, 105–113 (2019).

198. Zhu, Y., Yin, F., Wang, H., Wang, L., Yuan, J. & Qin, J. Placental Barrier-on-a-Chip: Modeling Placental Inflammatory Responses to Bacterial Infection. *ACS Biomater. Sci. Eng.* **4**, 3356–3363 (2018).

199. Miura, S., Sato, K., Kato-Negishi, M., Teshima, T. & Takeuchi, S. Fluid shear triggers microvilli formation via mechanosensitive activation of TRPV6. *Nat. Commun.* **6**, 8871 (2015).

200. Apps, R., Sharkey, A., Gardner, L., Male, V., Trotter, M., Miller, N., North, R., Founds, S. & Moffett, A. Genome-wide expression profile of first trimester villous and extravillous human trophoblast cells. *Placenta* **32**, 33–43 (2011).

201. Hwang, H. H., You, S., Ma, X., Kwe, L., Victorine, G., Lawrence, N., Wan, X., Shen, H., Zhu, W. & Chen, S. High throughput direct 3D bioprinting in multiwell plates. *Biofabrication* **13**, 025007 (2021).

202. Igura, K., Zhang, X., Takahashi, K., Mitsuru, A., Yamaguchi, S. & Takashi, T. A. Isolation and characterization of mesenchymal progenitor cells from chorionic villi of human placenta. *Cytotherapy* **6**, 543–553 (2004).

203. Okae, H., Toh, H., Sato, T., Hiura, H., Takahashi, S., Shirane, K., Kabayama, Y., Suyama, M., Sasaki, H. & Arima, T. Derivation of Human Trophoblast Stem Cells. *Cell Stem Cell* **22**, 50-63.e6 (2018).

204. Kozler, P. & Pokorný, J. Altered blood-brain barrier permeability and its effect on the distribution of Evans blue and sodium fluorescein in the rat brain applied by intracarotid injection. *Physiol. Res.* **52**, 607–614 (2003).

205. Brandes, J. M., Tavoloni, N., Potter, B. J., Sarkozi, L., Shepard, M. D. & Berk, P. D. A new recycling technique for human placental cotyledon perfusion: Application to studies of

the fetomaternal transfer of glucose, inulin, and antipyrine. *Am. J. Obstet. Gynecol.* **146**, 800–806 (1983).

206. Hahn, T., Barth, S., Weiss, U., Mosgoeller, W. & Desoye, G. Sustained hyperglycemia in vitro down-regulates the GLUT1 glucose transport system of cultured human term placental trophoblast: a mechanism to protect fetal development?1. *FASEB J.* **12**, 1221–1231 (1998).

207. Teasdale, F. Gestational changes in the functional structure of the human placenta in relation to fetal growth: a morphometric study. *Am. J. Obstet. Gynecol.* **137**, 560–568 (1980).

208. Wice, B., Menton, D., Geuze, H. & Schwartz, A. L. Modulators of cyclic AMP metabolism induce syncytiotrophoblast formation in vitro. *Exp. Cell Res.* **186**, 306–316 (1990).

209. Palmeira, P., Quinello, C., Silveira-Lessa, A. L., Zago, C. A. & Carneiro-Sampaio, M. IgG Placental Transfer in Healthy and Pathological Pregnancies. *Clin. Dev. Immunol.* **2012**, 985646 (2012).

210. Bianconi, E., Piovesan, A., Facchin, F., Beraudi, A., Casadei, R., Frabetti, F., Vitale, L., Pelleri, M. C., Tassani, S., Piva, F., Perez-Amodio, S., Strippoli, P. & Canaider, S. An estimation of the number of cells in the human body. *Ann. Hum. Biol.* **40**, 463–471 (2013).

211. Zhu, W., Qu, X., Zhu, J., Ma, X., Patel, S., Liu, J., Wang, P., Lai, C. S. E., Gou, M., Xu, Y., Zhang, K. & Chen, S. Direct 3D bioprinting of prevascularized tissue constructs with complex microarchitecture. *Biomaterials* **124**, 106–115 (2017).